Intra and Inter-Continental Aerosol Transport and Local and Regional Impacts

by

Leona Ann Marie Charles

A dissertation submitted to the Graduate Faculty in Electrical Engineering in partial fulfillment of the requirements for the degree of Doctor of Philosophy, The City University of New York

2008

UMI Number: 3296968

ProQuest Information and Learning Company
300 North Zeeb Road
P.O. Box 1346
Ann Arbor, MI 48106-1346

This manuscript has been read and accepted for the
Graduate Faculty in Engineering in satisfaction of the
dissertation requirement for the degree of Doctor of Philosophy.

Dr. Fred Moshary

Date — Chair of Examining Committee

Mumtaz K. Kassir

Date — Executive Officer

Prof. Barry Gross, Dept. of Electrocal Engineering, CCNY

Prof. Samir Ahmed, Dept. of Electrocal Engineering, CCNY

Prof. Reza Khanbilvardi, Dept. of Civil Engineering, CCNY

Dr. Ali Omar, Science Directorate, NASA

Dr. John Edward Anthony Selby, Consultant Engineer, NGC
Supervisory Committee

THE CITY UNIVERSITY OF NEW YORK

Abstract

Intra and Inter-Continental Aerosol Transport and Local and Regional Impacts

by

Leona Charles

Advisers: Prof. Fred Moshary and Co-mentor: Prof. Barry Gross

Under the Clean Air Act, the Environmental Protection Agency (EPA) is required to establish a nationally uniform air quality index for the reporting of air quality. In 1976, the EPA established this index, then called the Pollutant Standards Index, for use by state and local communities across the country. The Index provides information on pollutant concentrations for ground-level ozone, particulate matter, carbon monoxide, sulfur dioxide, and nitrogen dioxide. On July 18, 1997, the EPA revised the ozone and particulate matter standards, in light of a comprehensive review of new scientific evidence including refined fine particulate matter standards. In particular, significant exposure studies have further reinforced the need to lower $PM_{2.5}$ concentrations, and currently, a notable portion of the urban North East is in compliance with the EPA standards as seen in Figure A1.

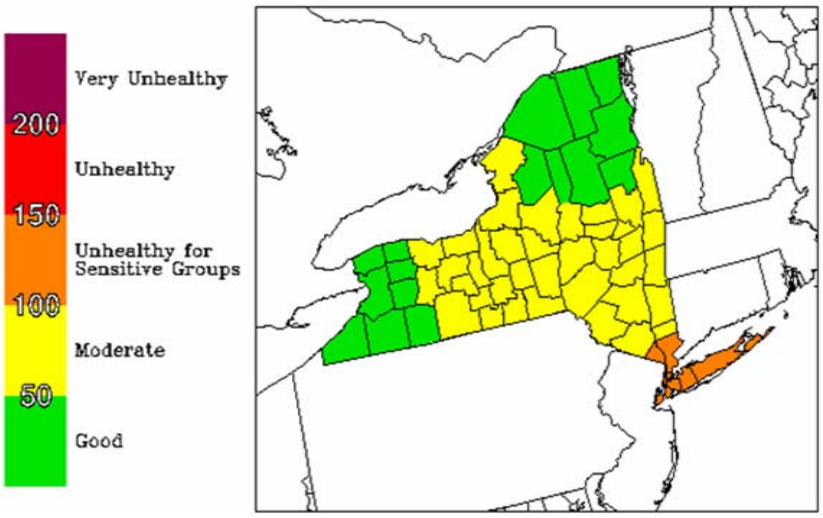

Figure A1: EPA PM2.5 Air Quality Map

Any program which is designed to improve air quality must devise tools in which emissions, meteorology, air chemistry and transport are understood. Clearly, the complexity of this task requires measurements at both regional and mesoscale ranges, as well as on a continental scale to investigate long range transport. Unfortunately, determination of fine particulate matter (PM) concentrations is particularly difficult since an accurate measurement of PM2.5 relies on costly equipment which cannot provide the complete transport story and the mixing and dispersion of particulate matter is much more complex than that for trace gases.

Besides the need for accurate measurements as a way of documenting air quality standards, the EPA is required in the near future to implement a 24 hour Air Quality Forecast. Current forecast tools are usually based on emission inventories and meteorological forecasts, but significant work is being done in trying to assimilate both ground measurements as well as satellite

measurements into these schemes. Clearly, the '*Holy Grail*' would be the capability of assimilating full 3D (+ time) measurements. However, since satellite measurements are primarily passive, only total air column properties such as aerosol optical depth can be retrieved. In particular, it is not possible to determine the vertical layering of aerosols in the troposphere from passive remote sensing measurements. Therefore, the connection with air pollution is very poor. Furthermore, the vertical structure of the aerosol is very important in assessing transport events and how they mix with the Planetary Boundary Layer (PBL).

The need to fill this data gap and supply vertical information on plume detection has led to the launch of the Cloud Aerosol Lidar and Infrared Pathfinder Satellite (CALIPSO) space borne lidar system, which can in principle provide vertical profiles of aerosol backscatter that can be used in the assimilation schemes. One particular problem which needs to be addressed, is the fact that the relationship between the optical scattering coefficients (or AOD) and the PM2.5 mass is not simple.

Finally, regarding non-attainment of National Ambient Air Quality Standards (NAAQS), it has also been shown that a significant portion of the PM2.5 aerosol mass can be due to non-local sources. This fact is critical in assessing the appropriate strategy in emission controls, as part of the state implementation plan (SIP) to come into compliance. However, these studies are usually based on statistical analysis tools such as Positive Factor Analysis (PFA), and are not applicable to any single measurement. In addition, little is known about the impact of episodic long range transport as a possible mechanism for

affecting local pollution. Such a mechanism cannot be investigated by statistical means or by any existing air transport models which do not consider high altitude plumes (aerosol layers), and must be studied solely with an appropriate suite of measurements including the simultaneous use of sky radiometers, lidars and satellites. Furthermore, since fine particulate matter is so crucial to identify, multi-wavelength determination of aerosol properties such as angstrom coefficient are necessary. It is our purpose to investigate the possibility that such long range transport events can indeed affect local air-quality. This may first seem improbable due to the high plume altitudes, but we will show by case studies that significant mixing into the PBL can occur and affect local air quality.

In particular, in chapters 5 and 6 we investigate dust and smoke transport events respectively, showing the usefulness of multi-wavelength lidar measurements to study the interaction of aerosols in the PBL with long range advected aerosol plumes. Our measurements are used to determine the plume angstrom exponent, which allows us to differentiate smoke events from dust events, as well as partitioning the total aerosol optical depth obtained from a CIMEL sky radiometer between the PBL and the high altitude plumes. Furthermore, the correlation between the lidar derived PBL aerosol optical depth and surface PM2.5 is high, only if the optical depth from the upper level plumes is taken into account. We also observe the dynamic mixing of high altitude plumes with the PBL and how they can significantly affect air quality as seen by the surface samplers. These local measurements are then compared to GOES AOD measurement data for the case of strong fire plumes. We also show that GOES

AOD data is very consistent with the sun-photometer data and clearly shows the onset of plumes over the NYC area. However, we do note the existence of a significant low bias in the GOES AOD product which can be attributed to a poor estimate of a “clean atmospheric column” which is not valid for summer months.

ACKNOWLEGEMENTS

A journey worth the time and effort!

I do not know what I may appear to the world, but to myself I seem to have been only like a boy playing on the seashore, and diverting myself in now and then finding a smoother pebble or a prettier shell than ordinary, whilst the great ocean of truth lay all undiscovered before me. -Isaac Newton

There are a number of people I would like to thank for a variety of reasons, and it is a pleasure to thank the many people who made this degree possible.

I would like to thank all those who have made my time at CCNY an enjoyable one. Of course, my thesis would be a dream without the guidance of my advisors Drs. Fred Moshary and Barry Gross. In particular, I would like to thank them for their patience and helpfulness in making my degree a success, and I could not have imagined having any better advisors and mentors throughout this journey. Their wide knowledge and logical ways of thinking have been of great value to me. Their understanding, encouragement and personal guidance have provided a good basis for my success.

Many thanks to my friends and family as well, for their support and good-natured skepticism which is at times the best kind of encouragement. My parents, for their constant loving support. My husband who stuck with me through thick and thin, for his understanding, endless patience and encouragement when it is most required.

CONTENTS

LISTS OF TABLES

LISTS OF FIGURES

LIST OF ACRONYMS

A

AERONET	AErosol RObotic NETwork
AIRS	Atmospheric Infrared Sounder
AOD	Aerosol Optical Depth
APD	Avalanche Photo Diode

B

BC	Black Carbon

C

CALIPSO	Cloud-Aerosol Lidar and Infrared Pathfinder Satellite Observation
CCNY	City College of New York
CO	Carbon Monoxide
Col5	Collection 5

E

EPA	Environmental Protection Agency

F

FOV	Field of View
FRM	Federal Reference Monitors

I

IDEA	Infusing Satellite Data into Environmental Applications
IPCC	International Panel of Climate Change

L

LIDAR	LIght Detection And Ranging

M

MISR	Mulitangle Imaging SpectroRadiometer
MODIS	Moderate Resolution Imaging Spectrometer
MOPITT	Measurement of Pollution In The Atmosphere

N

NAAQS	National Ambient Air Quality Standards
NASA	National Aeronautic and Space Aviation
NCEP	National Center for Environmental Prediction
ND: YAG	Neodymium-doped Yttrium Aluminum Garnet
NOAA	National Oceanic and Atmospheric Administration
NOx	Nitrogen Oxides

O

OC	Organic Carbon
OMI	Ozone Mapping Instrument

P

PFA	Positive Factor Analysis
PM	Particulate Matter
PM2.5	Particulate Matter less than 2.5 microns in diameter
PMT	Photo Multiplier Tube

S

SIP	State Implementation Plan
SOx	Sulfur Oxides

T

TEOM	Tapered Element Oscillating Microbalance
TES	Tropospheric Emission Spectrometer

V

VOCs	Volatile Organic Compounds

1. INTRODUCTION

As far back as the 1970's, air quality measurements demonstrated that pollutant emission can be transported over large distances. This realization of long range transport of pollutants has led to numerous air quality networks, models, and large scale field studies in an effort to understand the physical and chemical properties governing local and regional transport [Schichtel et al. 1995].

Aerosol, also known as particulate matter (PM), is one of the major air pollutants determining ambient air quality. Airborne particulate matter is a complex mixture of many different chemical species originating from a variety of sources, and their composition varies by geographical location, and also has a seasonal variability. Air borne particle sizes vary widely from a few nanometers to a few hundred micrometers in diameter. The size of aerosols is often critical to their transport and impact.

Aerosols can be transported over large distances from their source regions and can affect air quality on local, regional and even inter-continental scales, which may come as a surprise. Clearly, there is a need to monitor aerosols globally because of the aerosol effects on the earth's radiation budget, and largely because of their potential impact on air quality and human health.

1.1 SATELLITE REMOTE SENSING

Satellites are being widely utilized to map the geographical distribution and to characterize aerosols globally since they have the capability of providing snap-shots of large-scale aerosol distribution during time of flight. Satellites like

MODIS and TOMS provide global coverage once daily; however, data is available only during times of overpass, which is impractical for tracking and monitoring large scale aerosol events. Geostationary Satellites (GOES) on the other hand, can provide coverage of the entire globe at 30 minute intervals providing a summary of the spatial extent of aerosol coverage, and the added capability of being able to track the time history of aerosol transport.

Unfortunately, the GOES sensor is a single channel sensor, which is therefore not useful for differentiating aerosols (e.g. smoke from dust). However, with the advent of multi-spectral polar orbiting sensors, as well as the possible fusion of different sensors, some classification and differentiation is possible.

At present, MODIS is the *workhorse* of the remote sensing community due to its wide swath and excellent spectral coverage. Current operational algorithms such as ‘collection 5’ (col5) are able to retrieve both aerosol optical depth and angstrom coefficients. Details of the algorithm can be referenced in appendix A. In past algorithms, handling surfaces other than dark vegetation were very problematic, but improvements in the current algorithms have improved the situation somewhat, although retrieval over urban areas is still very challenging. However, MODIS is not able to measure absorbing properties well, therefore, other techniques are needed.

For example, measurements from OMI aboard the AURA satellite are very sensitive to the coupling of aerosols and Rayleigh scattering, and are ideally suited for the assessment of absorption. Due to the large Rayleigh scattering optical depth and low albedo of the surface in the blue/UV, ground contamination is minimal, so UV aerosol retrievals can work over urban areas, but ambiguities

due to lack of vertical information can strongly modify the results [Yu et al., 2005; Brinksma et al., 2003]. However, it is expected that with CALIPSO being able to clearly determine the vertical location of aerosols, a much better absorbing diagnostic is possible and will be used to fix the imaginary refractive index of the aerosols, while simultaneously providing us with a means to determine aerosol "type".

Another example is the NASA Glory Aerosol Polarimetry Sensor, expected to be launched in 2008, and fly in formation with the "A-Train" satellite constellation. Measurements from this sensor can be combined with MODIS, OMI and CALIPSO to provide better constraints on the aerosol models, particularly size and refractive index used in the MODIS retrievals, and thereby improve the fine/coarse mode fraction estimated by MODIS [Diner et al. 2004]. In addition, we are in a unique position to validate improvements in fine /coarse mode due to the addition of a 1630 nm channel on the CCNY AERONET CIMEL instrument.

It has been suggested that Carbon Monoxide (CO) estimates from MOPITT, TES and AIRS can provide better identification of smoke (carbonaceous aerosols) in MODIS, MISR and OMI aerosol retrievals. Details of the OMI retrieval algorithm can be obtained in appendix A. Biomass burning aerosols are associated with high CO levels and have very high real refractive indices; they are quite absorbing and tend to be very small. Using CO signatures to select the appropriate biomass burning aerosol model is straight forward and will substantially improve the accuracy of the aerosol retrievals from these various sensors. Also, in terms of air quality, having a combined estimate of

particle load and CO concentration is valuable when evaluating the potential effects of forest fires on air quality.

1.2 GROUND-BASED REMOTE SENSING

Although satellite measurements are crucial for understanding the aerosol transport and air quality prediction schemes, they only provide information on the total atmospheric column with the exception of CALIPSO. Because of their lack of information on the layering of the atmospheric column, this limits the use of satellite measurements for air quality applications. Since plumes can at times be transported aloft and remain entrained in layers, or even advect downwards and mix with the surface air and can go undetected by satellites, this makes connections of satellite measurements to ground measurements difficult.

On the other hand, conventional multi-wavelength lidars can be very useful tools for monitoring aerosol properties at a single convenient location. They have the capability of providing detailed information on the vertical layering of the atmosphere above. They also have the added capability of identifying the existence and extent of aerosol plumes that have undergone long-range transport, and additionally provide methods to determine the optical properties of aerosol plumes and help in their identification and characterization. Finally, these vertical measurements are critical in probing the performance of air quality models such as the Community Multiscale Air Quality (CMAQ) model system and the Weather Research and Forecast Chemistry (WARF-CHEM) model systems.

Unfortunately, lidar measurements suffer from a need to identify an extinction-to-backscatter ratio and can therefore result in incorrectly retrieved

vertical profiles. However, this problem is somewhat reduced with the help of sky radiometers. In particular, combining lidar with total column optical depth, allows us to constrain the lidar retrievals and provide a useful lidar (S) ratio. In addition, when such measurements are not available, a suitable aerosol climatology based on AERONET Sky Radiometry measurements has been developed and used.

1.3 CONNECTING SURFACE PM TO REMOTE SENSED COLUMN DATA

In an effort to improve Air Quality Forecasting, the EPA together with NASA and NOAA, implemented an ambient air-quality monitoring program to determine the composition of airborne $PM_{2.5}$ in urban air, in an effort to assimilate satellite measurements of aerosol column optical depth into air quality transport models. While satellite AOT products provide critical references for air quality monitoring, they are unable to provide aerosol vertical distribution. Therefore, to connect these satellite measurements with surface measurements such as PM2.5 requires an assumption that the PBL is well mixed and no aloft layers are present. However, these two assumptions are often not met; as a result transport models that ingest data based on these assumptions are not always accurate.

Much effort has been made to relate surface PM2.5 and column AOD. However, it must be emphasized that these measurements can be very inaccurate when plumes are present in the atmospheric column and a means to separate (or filter) the plume events or compensate for them is crucial. To this end, lidars are capable of isolating the PBL AOD contribution from the total integrated column AOD, and therefore a partition of the total column loading can

be done since lidars can provide accurate measurements of the column extinction. While this may be done from a ground based lidar, it is hoped that with the advent of CALIPSO, such apportionment can be done on the data where MODIS AOD can take the place of the sun-photometer, although clearly, this approach will not be nearly as accurate.

However, even with these problems, the potential for monitoring PM air quality using satellite data from space-based sensors from regional to global scales has been recently demonstrated using aerosol optical thickness (AOT) data [Wang et al., 2003; Chu et al., 2003; Engel-Cox, et al., 2004]. Although the satellite-based retrieval of air quality is promising in regions where the PBL is well mixed, it poses several challenges. There are many factors that can affect the relationship between AOT and PM2.5. For example, the satellite-derived quantities provide columnar information for ambient conditions whereas the PM2.5 measurements are representative of near-surface dry mass concentrations. Other issues including variations in aerosol type, PBL Height and hygroscopic properties must be adequately understood before using satellite data for air quality assessment.

REFERENCES

Brinksma, E. J., K. F. Bousma, and P. F. Levelt, "Validation Requirements Document", 2003.

Chu, D. A., Y. J. Kaufman, G. Zibordi, J. D. Chern, J. Mao, C. Li and B. N. Holben, "Global Monitoring of air pollution over Land from the Earth Observing System – Terra Moderate Resolution Imaging Spectrometer (MODIS)", Journal of Geophysical Research, VOL. 108, D21, 2003.

Diner, D. I., Russe A. Chipman, Neil Beaudryb, Brian Caims, Leslie D. Food, Steven A. Macenka, Thomas J. Cunningham, Suresh Seshadli, and Christoph Keller, "An integrated multiangle, multispectral, and polarimetric imaging concept foor aerosol remeote sensing from space", 2004.

Diner, D.J., T.P. Ackerman, T.L. Anderson, J. Bosenberg, A.J. Braverman, R.J. Charlson, W.D. Collins, R. Davies, B.N. Holben, C.A. Hostetler, R.A. Kahn, J.V. Martonchik, R.T. Menzies, M.A. Miller, J.A. Ogren, J.E. Penner, P.J. Rasch, S.E. Schwartz, J.H. Seinfeld, G.L. Stephens, O. Torres, L.D. Travis, B.A. Wielicki, and B. Yu, "PARAGON: An integrated approach for characterizing aerosol climate impacts and environmental interactions", Bull. Amer. Meteorol. Soc., **85**, 14911-1501, 2004.

Engel-Cox, J. A., H. H. Christopher, B. W. Coutant and R. M. Hoff, "Qualitative and Quantitative evaluation of MODIS satellite sensor data for regional and urban scale air quality", Atmospheric Environment, VOL. 38, pp. 2495-2509, 2004.

Heintzenberg, Jost and David S. Covert, "On the distribution of physical and chemical particle properties in the atmospheric aerosol", Journal of Atmospheric Chemistry, VOL. 10, 4, 1990.

Schneider, J. and R. Eixmann, "Three years of routine Raman lidar measurements of tropospheric aerosols: Backscattering, extinction, and residual layer height" Atmos. Chem. Phys., 2, 313–323, 2002.

Wang J. and S. A. Christopher, "Inter-comparison between Satellite-derived Aerosol Optical Thickness and PM2.5 mass: Implications of Air Quality Studies", Geophysical Research Letters, VOL. 30, 2003.

Yu, H., Y. J. Kaufman, M. Chin, G. Feingold, L. A. Remer, T. L. Anderson, Y. Balkanski5, N. Bellouin, O. Boucher, S. Christopher, P. DeCola, R. Kahn, D. Koch, N. Loeb, M. S. Reddy, M. Schulz, T. Takemura, and M. Zhou, "A review of measurement-based assessment of aerosol direct radiative effect and forcing", Atmos. Chem. Phys. Discuss., 5, 7647-7768, 2005.

2. MOTIVATION FOR AEROSOL MONITORING

2.1 INTRODUCTION

Air quality in New York City and elsewhere is highly dependent on the meteorological conditions that govern the transport and mixing of trace gases and aerosol particles. These processes occur on a variety of scales, namely; regional, intra-continental and inter-continental scales, and vertically, the Atmospheric boundary layer and the free troposphere. Previous studies have demonstrated, on all of these scales, the impact of transport processes on the east coast air quality [NEAQS_ITCT 2003]. A clear understanding of transport on these scales will allow us to assess the impact from local, regional, and distant sources on air quality of air masses as they traverse NYC and are transported to downwind locations.

2.2 AIR POLLUTION SOURCES

Some aerosols are primary pollutants emitted directly into the atmosphere, while others are secondary pollutants formed by the transformation of pre-existing gases or from the growth of smaller particulates into larger ones by coagulation.

Sources of particulate matter (PM) can be either primary or secondary in nature. Primary particles can be further divided into anthropogenic or natural depending on their origin. Secondary formed particles in the atmosphere are from both natural and anthropogenic origin and originate from chemical transformations of gaseous precursors such as SO_X, NO_X and VOCs. Natural

particulates introduced directly into the atmosphere can originate from natural fires, wind blown dust, sand, volcanic eruptions, the ejection of sea salt, and by the entrainment of pollen by wind. Some indirect aerosols form by the coagulation of gases, and are most rapid at high relative humidity [Aguado at al. 2004].

The lifetime of particulate matter in the atmosphere ranges from a few days to a few weeks and these relative long residence times are due to small differences between the average total mass of $PM_{2.5}$ between urban and non-urban continental aerosols (Heintzenberg, 1989).

Air pollution comes from many different sources: point (i.e. stationary) sources such as factories, mobile sources, and naturally occurring sources such as wind-blown dust, and volcanic eruptions, all contribute to air pollution. Air Quality can be affected in many ways by the pollution emitted from these sources. The EPA has these pollutants classified as the six principal pollutants, namely; sulfur dioxide, carbon monoxide, ozone, lead, particulate matter and nitrogen oxide. The United States EPA, and other federal agencies are researching and developing air pollution prevention technologies, providing scientific data to prevent human population exposures to hazardous air pollutants, and using statistics to predict current and future air pollution levels.

Atmospheric aerosols (tropospheric and stratospheric) are of great importance because of their role in long-range transport of pollutants, their impacts on human health, visibility, continental and maritime ecosystems, the stratospheric ozone layer, and the Earth's climate, thus requiring dedicated

monitoring of their concentrations and properties at the regional and global scales.

2.3 AEROSOL EFFECTS ON CLIMATE

Aerosols have a direct radiative forcing because they scatter and absorb solar and infrared radiation in the atmosphere. Aerosols also alter the formation and precipitation efficiency of liquid-water, ice and mixed-phase clouds, thereby causing an indirect radiative forcing associated with these changes in cloud properties.

Aerosols tend to cause cooling of the Earth's surface immediately below them. Because most aerosols reflect sunlight back into space, they have a "direct" cooling effect by reducing the amount of solar radiation that reaches the Earth's surface. The magnitude of this cooling effect depends on the size and composition of the aerosol particles, as well as the reflective properties of the underlying surface.

The effect of anthropogenic emissions from activities, such as fossil fuel, biomass, and bio-fuel burning, transportation, and land-clearing, have a profound impact on the climate system. The impact of these activities is manifested in observed changes in temperature, precipitation, sea-level rise, melting of glaciers, air quality, health, and agriculture yields, to name a few. The obvious question to ask is the role that these different processes play in affecting climate and what action could one impose to curtail or constrain adverse human impacts on climate [Menon, 2004].

Greenhouse gases, ozone, and black carbon (BC) aerosols are usually associated with global warming, whereas aerosols, such as sulfates and organic carbon (OC), and their interaction with clouds result in global cooling. Whereas global warming effects from greenhouse gases and ozone can be quantified fairly well, the magnitude of the effects of aerosols on climate still has a large uncertainty associated with it. Figure 1 shows the global mean radiative forcing from 1750 to 2005, which is an imposed, natural, or anthropogenic perturbation of the Earth's energy balance with space [IPCC 2007].

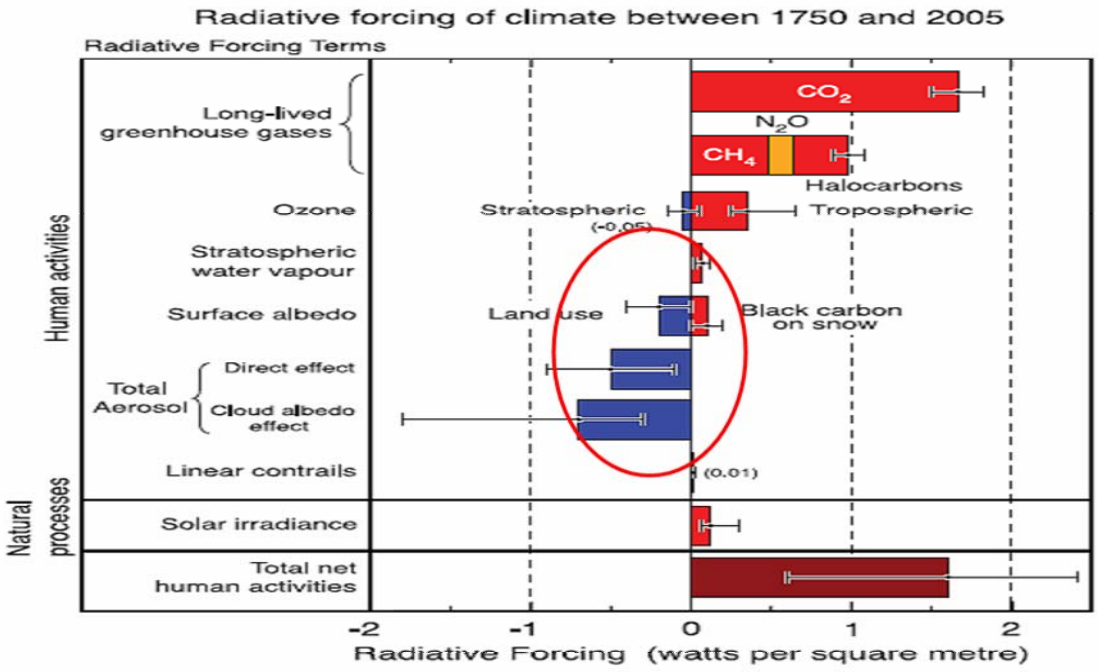

Fig. 2.1 Principal components of the Global radiative forcing of climate change, levels of understanding and uncertainties [IPCC 2007]

Increasing anthropogenic greenhouse gases cause the largest positive forcing [Hansen et al., 2001]. Among green house gases, carbon dioxide has caused the largest positive forcing during this period (warming). It is important to

note that the largest uncertainties in climate forcing (negative forcing, i.e., cooling) are due to tropospheric aerosols (dust), which can interact with clouds and influence precipitation, by acting as cloud condensation nuclei or ice nuclei, that is the indirect forcing effect on climate change. Thus, they have an influence on the radiative balance of the Earth-Atmosphere system, which could also have an influence on the hydrological cycle. The direct radiative forcing summed over all aerosol types is negative. Aerosols also cause a negative radiative forcing indirectly through the changes they cause in cloud properties [IPCC 2007].

The IPCC also reports that the forcing due to greenhouse gases has increased, which are largely due to human activities. This contributes to an overall heating of the atmosphere, mainly because gases absorb outgoing infrared radiation in the atmosphere. Among those greenhouse gases, increases in CO_2 have caused the largest forcing during this period.

2.3.1 Aerosol Direct Effect

The so-called "direct effect" of radiative forcing on climate relates to the changes in net radiative fluxes in the atmosphere caused by the modulation of atmospheric scattering and absorption properties due to changes in the concentration and optical properties of the aerosol.

2.3.2 Aerosol Indirect Effect

Indirect forcing by aerosols is broadly defined as the overall process by which aerosols perturb the Earth-atmosphere radiation balance by modulation of cloud

albedo and cloud amount. Aerosols serve as cloud condensation nuclei and ice formation nuclei, thereby modifying the microphysics, the radiative properties, and the lifetime of clouds. The aerosol indirect effect is usually split into two effects: the first indirect effect, whereby an increase in aerosols causes an increase in droplet concentration and a decrease in droplet size for fixed liquid water content [Twomey, 1977], and the second indirect effect, whereby the reduction in cloud droplet size affects the precipitation efficiency, tending to increase the liquid water content, the cloud lifetime [Albrecht, 1989], and the cloud thickness [Pincus and Baker, 1994].

2.4 Aerosol Effects on Health

Particulate matter is defined by three general categories commonly used by the U.S. Environmental Protection Agency (U.S. EPA): coarse (2.5 to 10 μm), fine (2.5 μm or smaller), and ultra fine (0.1 μm or smaller). Research [Bret et al., 2006; Poschl et al., 2006] suggests that particle size is an important factor that influences how particles deposit in the respiratory tract and affect human health.

Coarse particles are deposited almost exclusively in the nose and throat; whereas, fine and ultra fine particles generally are able to penetrate to deep areas of the lung. Fine and ultra fine particles are present in greater numbers and have greater surface area than larger particles of the same mass, and they are generally considered to be more toxic.

Because these particles ($PM_{2.5}$) are so small, they are able to penetrate to the deepest parts of the lungs. Scientific studies, for example Schwatz et al. in 1994, have suggested links between fine particulate matter and numerous health

problems including asthma, bronchitis, acute and chronic respiratory symptoms such as shortness of breath and painful breathing, and premature deaths.

Over the years, an increasing number of studies have reported a link between $PM_{2.5}$ and adverse respiratory and cardiovascular effects in people. [Dockery et al., 1994] The health effects of particulates matter are heavily dependent on particle size and composition, and the concentrations and lifetime. In an effort to improve Air Quality Forecasting, the EPA has implemented an ambient air quality-monitoring program to determine the composition of airborne $PM_{2.5}$ in urban air.

2.5 Air Quality Monitoring

NOAA has been directed by congressional mandate to implement an operational air quality forecast system, which will provide 24-48hr forecasts of ozone and fine particulate matter ($PM_{2.5}$) to benefit public health. In order to perform this obligation, NOAA and the EPA formed a partnership to transfer scientific advances in air quality monitoring and forecasting into the National Center for Environmental Prediction (NCEP). In support of this effort, the IDEA (Infusing satellite Data into Environmental Applications) product was developed through a joint collaboration between NASA, EPA and NOAA, which couples a satellite estimate of aerosol optical depth (AOD) using the MODIS sensor into a NOAA Lagrangian transport model [Szykman et al., 2004]. The air quality forecast is then assessed through the use of the EPA $PM_{2.5}$ surface-monitoring network.

There is increased interest in the properties of small airborne particles (aerosols) because of the role that they play in many environmental processes. Urban air quality monitoring and forecasting have become an important and challenging concern. $PM_{2.5}$ is particularly of concern because they are a risk to human health and the environment.

Particulate matter is an important parameter that has been used worldwide to evaluate air quality. In recent years, research studies have shown the potential to monitor air quality from space-based observations, as a possible method for regions were the ground-based $PM_{2.5}$ measurements are sparse. Conventional lidars and ground radiometers also show potential to predict air quality, especially in urban regions where pollution monitoring seems quite complicated.

Remote sensing provides valuable data on aerosol distribution and transport, which has traditionally been used in climate studies. Relating aerosol measurements to surface fine particulate concentration ($PM_{2.5}$) is attractive, as remotely sensed data allows for large spatial coverage not possible with point monitors. Several studies over the past years have demonstrated the relationship between satellite-derived AOT and ground-based measurements of $PM_{2.5}$ mass [Chu et al., 2003; Engel-Cox et al., 2004]. Wang et al. (2003) showed that MODIS AOT data is well correlated with $PM_{2.5}$ mass over the South eastern United States, and concluded that satellite AOT can be a useful tool for monitoring air quality over large scales. However, information on the vertical distribution of aerosols (ground based lidars) and meteorological information to

take into account PBL Height and aerosol variability is needed to further refine the analysis.

Further, the ability to track the transport of aerosols allows for better understanding of pollution sources and emission inventories. However, it is important to note that remotely sensed observations are related to the optical properties of fine particulates, not their mass. Additionally, these measurements are in most cases, column measurements, and not surface measurements. Therefore, it is crucial to have complementary information on the altitude variability of aerosol distributions from both ground and space-borne lidars. These observations need to be carried out over time to be able to derive the correlations necessary to use aerosol optical depth as a proxy for $PM_{2.5}$.

The EPA is currently setting air quality standards relating to the concentration levels of six main air pollutants: ozone, particulate matter, carbon monoxide, nitrogen dioxide, sulfur dioxide and lead. The EPA is also responsible for forecasting concentration levels of two of these pollutants: ozone and particulate matter (PM).

Table 2.1 presents details on the air-quality categories as defined by National Ambient Air Quality Standards (NAAQS) for different categories and the corresponding $PM_{2.5}$ mass values. According to these standards, the 24-h mean value of $PM_{2.5}$ mass should be less than 65 μgm^{-3} and 15 μgm^{-3} for the annual mean.

Index Values	Category	Cautionary Statements	$PM_{2.5}$ (ug/m^3)	PM_{10} (ug/m^3)
0-50	Good	None	0-15.4	0-54
51-100	Moderate	Unusually sensitive people should consider reducing prolonged or heavy exertion	15.5-40.4	55-154
101-150	Unhealthy for Sensitive Groups	Sensitive groups should reduce prolonged or heavy exertion	40.5-65.4	155-254
151-200	Unhealthy	Sensitive groups should avoid prolonged or heavy exertion; everyone else should reduce prolonged or heavy exertion	65.5-150.4	255-354
201-300	Very Unhealthy	Sensitive groups should avoid all physical activity outdoors; everyone else should avoid prolonged or heavy exertion	150.5-250.4	355-424

Table 2.1: US Environmental Protection Agency (EPA) Air Quality Index (AQI) for particle pollution, and categories for $PM_{2.5}$ mass concentrations, air-quality category, corresponding 24-hourly mean $PM_{2.5}$ mass (μgm^{-3}) and their potential effects on human health.

2.5.1 Particulate Matter

Particle pollution or particulate matter (PM) is the general term used to describe a mixture of solid particles and liquid droplets in the air. Particles are classified as coarse (e.g., dirt or dust) or fine (i.e., the by-products of fuel combustion). PM can be emitted directly into the atmosphere (e.g., wind blown dust) or formed in the atmosphere through chemical reactions (i.e., sulfates and nitrates formed from emissions of power plants and vehicle exhaust.)

Particulate matter (PM), including fine particulate matter ($PM_{2.5}$), is one of the six principal pollutants for which the U.S. Environmental Protection Agency (EPA) has set National Ambient Air Quality Standards (NAAQS) under the Clean Air Act (CAA).

The EPA has a ground network of monitoring stations around the country that are currently being used to monitor concentration levels of $PM_{2.5}$ and could be used as input to forecasts of $PM_{2.5}$. The networks monitor the concentration (and at some sites, speciation) of particulate and gaseous air pollutants at the ground level. PM2.5 monitoring (mass and speciation) is most important to this project. In addition to the filter-based 24-h average from Federal Reference Monitors (FRM), Tapered Element Oscillating Microbalance (TEOM) and other instruments provide continuous PM2.5 concentration data in real-time.

However, the EPA recognizes that the utility of this network may be improved with the addition of satellite imagery, which can provide information about the air in regions not covered by these monitoring stations. The addition of satellite data could also assist in identifying areas that are generating particle pollution and areas that are receiving pollution due to transport between regions. Aerosol products from existing satellite systems were identified as potential data sets that could add value to the forecast.

$PM_{2.5}$ Data Collection

The Tapered Element Oscillating Microbalance (TEOM) is an automated continuous particle monitor. The TEOM draws air through a hollow tapered tube, with the wide end of the tube fixed, while the narrow end oscillates in response to an applied electric field. The filter cartridge is at the narrow end of the tube. The sampled airflow passes from the sampling inlet, through the filter, to a flow controller. As particles are collected on the filter, the mass changes resulting in a change of the oscillating frequency. Using the rate of mass accumulation on the

filter and the flow rate through the sample (main) flow controller, the TEOM's microprocessor calculates the mass concentration. The flow rate through the sample filter is set at a nominal 3.0 litres per minute (L/min). A bypass (auxiliary) flow is used to provide an additional 13.67 L/min for a total flow rate of 16.67 L/min; the design flow of the size selective inlet [Parikh, 1999].

REFERENCES

Albrecht, B. A., "Aerosols, cloud microphysics and fractional cloudiness. Science", 245, 1227–1230, 1989.

Bret Brunekreef, "Health Effects of Ambient Particulate Matter", 7th International Aerosol Conference, Minnesota, 2006.

Chu, D. A., Y. J. Kaufman, G. Zibordi, J. D. Chern, J. Mao, C. Li and B. N. Holben, "Global Monitoring of air pollution over Land from the Earth Observing System – Terra Moderate Resolution Imaging Spectrometer (MODIS)", Journal of Geophysical Research, VOL. 108, D21, 2003.

Dockery, D. W. and C. A. Pope III, "Acute Respiratory Effects of Particulate Air Pollution", NYU, Annual Review of Public Health, 15, 1994.

Forster, P., V. Ramaswamy, P. Artaxo, T. Berntsen, R. Betts, D.W. Fahey, J. Haywood, J. Lean, D.C. Lowe, G. Myhre, J. Nganga, R. Prinn, G. Raga, M. Schulz and R. Van Dorland, 2007: "Changes in Atmospheric Constituents and in Radiative Forcing. In: Climate Change 2007: The Physical Science Basis. Contribution of Working Group I to the Fourth Assessment Report of the Intergovernmental Panel on Climate Change" [Solomon, S., D. Qin, M. Manning, Z. Chen, M. Marquis, K.B. Averyt, M.Tignor and H.L. Miller (eds.)]. Cambridge University Press, Cambridge, United Kingdom and New York, NY, USA.

Hansen, James E. and Makiko Sato, "Trends of measured climate forcing agents", Proceedings of the National Academy of Sciences (PNAS), 98, 26, 2001.

Heintzenberg J., "Arctic haze: Air pollution in polar region", AMBIO 18(1): 50-55, 1998.

NOAA's ARC, "NEAQS-ITCT 2004 Science & Implementation Plan", 2003.

Pincus, R. and M. B. Baker, "Effect of precipitation on the albedo susceptibility of marine boundary layer clouds", Nature, 372, 250–252, 1994.

Poschl, U., T. Fehrenbach, T. Franze, U. McKeon, A. Messerer, E. Mikhailov, R. Niessner, C. Schauer, and A. Zerrath, "Carbonaceous Aerosol Components: Properties, Interactions, Climate and Health Effects", Geo. Res. Letters, 8, 2006.

Schwartz, Joel and Douglas W. Dockery, "Particulate Air Pollution and Daily Mortality in Steubenville, Ohio", Amer. Jour. Epidemiology, VOL. 135, 1994.

Szykman, J., et al "Utilizing MODIS satellite observations in near-real-time to improve AIRNow next day forecast of fine particulate matter, PM2.5" Proceedings of the Sixth Conference on Atmospheric Chemistry, American Meteorological Society, January 10-15, 6pp. (2004).

Twomey, S., "The influence of pollution on the short wave albedo of clouds", J. Atmos. Sci., 34, 1149–1152, 1977.

3. LIDAR INSTRUMENTATION AND ANALYSIS

3.1 Introduction

Optical remote sensing techniques are used today for monitoring atmospheric characteristics, due to the fact that an obstacle could be “seen” by an electromagnetic wave having a wavelength of the same magnitude as the geometric dimension of the obstacle. So, using a light beam (wavelength nm to μm) one can detect atmospheric components, which are “invisible” to other sounding waves. Very important among optical remote sensing techniques are the **LIDARs** (**LI**ght **D**etection **A**nd **R**anging), based on the use of pulse or continuous lasers as high sensitivity and a long range of penetration characterize them.

Lidars are laser-based systems for atmosphere sounding, which allows the detection of suspended particulate in the sounding direction, with very good precision and in a very short time (seconds). The main components for any Lidar system are the transmitter (pulsed, high power laser), the receiver (telescope + spectrum analyzer + low level, high speed photodetectors) placed on a common platform, and the high speed acquisition system with analog-to-digital converter. Laser transmitted radiation is scattered by the aerosols, so that a fraction of radiation backscattered by each volume of air can be captured, detected and analyzed. The return signal contains information about the concentration and some physical characteristics of particles in the laser beam direction. Lidars can be mobile and can thus be used at different sites, including satellites. Lidar measurements permit a highly accurate determination of the type and size of

atmospheric constituents, even at long distances, lidars and are able to detect very low concentrations, as well as providing for a study of their spatial-temporal dynamics. This measurement technique can infer several characteristics of the intervening atmosphere and the lidar echo has numerous applications.

When the beam encounters aerosol particles or air molecules in the atmosphere, laser radiation is scattered in all directions including some in the direction from which the radiation came. Hence, the term backscatter is used to define the radiation returned to a receiver. With very short pulses of radiation sent out, timing how long it takes for pulses to be returned allows the backscattered radiation to be determined at a number of range intervals from the lidar system. If the lidar system has been calibrated, backscatter is defined in units of per meter per steradian ($m^{-1}sr$-1). Since backscatter can vary over a wide range of values (up to five orders of magnitude depending on the type of scatterer and its concentration), the logarithm of the backscatter is often used to allow plots of the backscatter data to be made.

Unfortunately, as the laser makes its way through the atmosphere, it passes through many different layers of air and therefore unlike radar, the signal is attenuated both prior to and after interaction with a given target layer. This attenuation (or more generally extinction) makes it difficult to interpret the backscatter directly since the extinction along the path must be estimated. This extinction is dependant on the properties of the target itself.

3.2 Extinction

Light from a laser can travel through air that consists of molecules, mostly nitrogen and oxygen, where some of the intervening light will be attenuated according to absorption and scattering by molecules and particles. The attenuation of the incoming intensity P(z) can be expressed as

$$\frac{dP(z)}{dz} = -\alpha P(z) \tag{3-1}$$

where α is the extinction coefficient of light per unit length. The extinction coefficient is a function of both the wavelength of light and range from the ground up. It comprises of a molecular contribution α_{mol} and an aerosol contribution α_{aer}, and can be written as follows,

$$\alpha = \alpha_{mol} + \alpha_{aer} \tag{3-2}$$

The extinction due to molecules can be calculated once the temperature and pressure vertical profiles are known, unless your laser line coincides with an absorption line of O_2 or other atmospheric species, like H_2O, O_3, CO etc.

3.3 Backscatter

Scattering occurs at several angles compared to the original direction of the laser beam and is dependent on the size and form of the aerosols. This can be visualized by a phase function. The photons are scattered (backscattered) at an angle of 180 degrees, i.e., to where the light originated. The amount of scattering varies typically with different angles and different particles; therefore

there is no relation between extinction coefficients and backscatter coefficients that is consistent in the atmosphere.

The backscatter coefficient β, is a formal way to describe the amount of incident light that scatters back along the direction of the incoming light. The backscatter coefficient, like the extinction also comprises of a molecular and an aerosol contribution, and has units of per unit length, per solid angle.

$$\beta = \beta_{mol} + \beta_{aer} \tag{3-3}$$

Nonetheless, there exists a relationship between the molecular backscatter and extinction coefficients, also referred to as the molecular lidar ratio, and can be expressed as:

$$\frac{\alpha_{mol}(\lambda, z)}{\beta_{mol}(\lambda, z)} = \frac{\mathbf{8}\pi}{\mathbf{3}} \tag{3-4}$$

3.4 BASIC LIDAR EQUATION

The lidar equation is for the power received by the detector of the instrument. Here the lidar equation is derived for the case of elastic atmospheric backscatter only. It is assumed that the wavelength of the emitted and detected radiation is the same.

When a short laser pulse of wavelength λ is emitted into the atmosphere, the detected power P of the backscattered light at distance R from the instrument in its simple form may be written as

$$P(R) = KG(R)\beta(R)T(R) \quad (3\text{-}5)$$

where,

P : power received from a distance R
K : constant dependent on the system performance
G(R): describes the range-dependent measurement geometry
$\beta(R)$: backscatter coefficient at distance R due to atmospheric scattering
T(R): transmission term describing how much light gets lost on the way from the lidar to R and back

The lidar performance (K) and the geometric factor (G(R)) are resolved by the lidar setup and set and varied at the discretion of user. The system factor (Eq. 3-6), the geometric factor (Eq. 3-7), the backscatter coefficient (Eq. 1.4), and the transmission term (Eq. 3-9) are detailed below.

The system factor can be written as

$$K = 1/2P_0c\tau A\eta \quad (3\text{-}6)$$

where P_0 is the average power of the individual laser pulse, τ is the temporal pulse length, A is the area of the primary receiver optics used for collection of the backscatter returns, and η is the system efficiency. The pulse energy and the length of the volume illuminated by the laser pulse are $E_0 = P_0r$ and $c\tau$ respectively. The user can optimize the overall system efficiency to obtain the best possible lidar signal.

The geometric factor includes the laser beam receiver field of view (FOV) overlap function O(R) and can be written as

$$G(R) = R^{-2}O(R) \quad (3\text{-}7)$$

The R^{-2} dependence is responsible for the large dynamic range of the lidar signal.

The total volume backscattering coefficient $\beta(R,\lambda)$ describes how much light is scattered into the backward direction and also determines the strength of the lidar signal and has unites of $km^{-1}sr^{-1}$. The backscatter coefficient consists of a molecular (Rayleigh) and an aerosol (Mie) contribution. The laser light in the atmosphere is scattered by molecules (through Rayleigh scattering where backscatter decreases with distance from ground, but vice versa for space-based lidars) and by aerosol scattering. Backscatter, $\beta(R,\lambda)$ can therefore be written as

$$\beta_T(R,\lambda) = \beta_{mol}(R,\lambda) + \beta_{aer}(R,\lambda) \tag{3-8}$$

The final component of the lidar equation, the transmittance at wavelength λ from instrument position to range R, and back to the instrument is given by the Beer-Lambert law and has values between 0 and 1

$$T(R,\lambda) = \exp\left[-2\int_0^R \alpha(R,\lambda)dr\right] \tag{3-9}$$

The extinction coefficient α [m^{-1}] also has a molecular and aerosol influence and is expressed as the sum of these two components, in the following way:

$$\alpha_T(R,\lambda) = \alpha_{mol}(R,\lambda) + \alpha_{aer}(R,\lambda) \tag{3-10}$$

where α_{mol} and α_{aer} correspond to the molecular and aerosol attenuation coefficients, respectively. Extinction occurs due to scattering and light absorption

by molecules and particles. Since scattering occurs in all directions and contributes to light extinction, the scattering cross section $\sigma_{sca,}$ and the absorption cross section σ_{abs} together make up the extinction cross section.

$$\sigma_{ext}(\lambda) = \sigma_{sca}(\lambda) + \sigma_{abs}(\lambda) \tag{3-11}$$

Substituting (3-1) to (3-7) into (3-5) the lidar equation is obtained:

$$P(R,\lambda) = P_0 \frac{c\tau}{2} A\eta \frac{O(R)}{R^2} \beta(R,\lambda) \exp\left[-2\int_0^R \alpha(r,\lambda) dr \right] \tag{3-12}$$

The lidar ratio S_a is derived from the ratio of the extinction to the backscatter and is assumed to be through the aerosol layer.

$$S_a = \frac{\alpha_a(r)}{\beta_a(r)} \tag{3-13}$$

For the visible channel (532 nm) the calibration constant is determined using the Fernald method, where the maximum range (R_{max}) is chosen to be the highest point in the lidar range. The Fernald solution fixes the boundary conditions at R_{max} and finds a solution by an iterative backward integration. We can therefore invert the lidar signal to retrieve the backscatter and extinction due to aerosols.

3.5 LIDAR DATA ANALYSIS

3.5.1 SOLUTIONS OF THE LIDAR EQUATION

The atmospheric extinction coefficient α_T is the fundamental parameter extracted from the elastic lidar signal [Kovelev et al., 2004]. However, the lidar equation contains more unknown values than equations which make it difficult to solve. To be able to reduce the complexity of the solution a few paramenters have to be estimated. Below we present two methods for the inversion of the lidar signal to obtain profiles of the extinction coefficient.

3.5.1.1 FERNALD'S METHOD

The Fernald's method [Fernald, 1984] for inverting the lidar backscatter signal to obtain the altitude profiles of aerosol extinction is based on the assumption that the aerosol extinction coefficient at a reference altitude and the aerosol extinction-to-backscatter ratio are known *a priori*. The solution for the two component lidar equation takes into consideration air molecules and aerosols under the assumption of a constant extinction-to-backscatter ratio (S_r). To be able to use Fernald's solution we must specify a far end (boundary) condition of a particular value for the extinction coefficient at a designated range (R_{max}). Since the extinction values at the far end are usually unknown, it is assumed that an aerosol-free layer exists at certain altitudes, which is a method to calibrate the lidar signal. In this case we assume that scattering occurs due to molecules only, which is considered a reasonable assumption around the tropopause. Although the algorithm is assumed to be nonadaptive, the reliability of the inverted profile is hampered by the two user inputs to the algorithm: the assumed

boundary condition at the far end of the inversion range and the assumed exponential term in the extinction-to-backscatter relationship.

The steps to the solution are outlined below:

1. The Lidar equation for two distinct classes of scatterers is

$$P(R) = C\left[\beta_{aer}(R) + \beta_{mol}(R)\right] T_{aer}^{2}(R) T_{mol}^{2}(R) \tag{3-14}$$

2. The molecular atmosphere scattering properties are determined from upper air meteorological soundings (temperature and pressure vertical profiles).

$$\beta_{mol}(R) = \frac{P_{mol}(R)/T_{mol}(R)}{\int_{R_0}^{R} P_{mol}(R)/T_{mol}(r)} \tau_{mol} \tag{3-15}$$

   Where, τ_{mol} is the molecular optical depth, P_{mol} and T_{mol} are pressure and temperature vertical profiles from upper air meteorological soundings.

3. The extinction-to-backscatter ratio for aerosols remains constant, since the atmosphere is assumed homogenous, which implies that the composition of the aerosol scatterers are unchanging, however, the variation in the backscatter from aerosols do change in their number density. The ratio for molecular scatterers is also a constant

$$S_{mol} = \frac{\alpha_{mol}(R)}{\beta_{mol}(R)} = \frac{8\pi}{3} \tag{3-16}$$

   In figure 3-1 we show a typical profile of molecular extinction and backscatter.

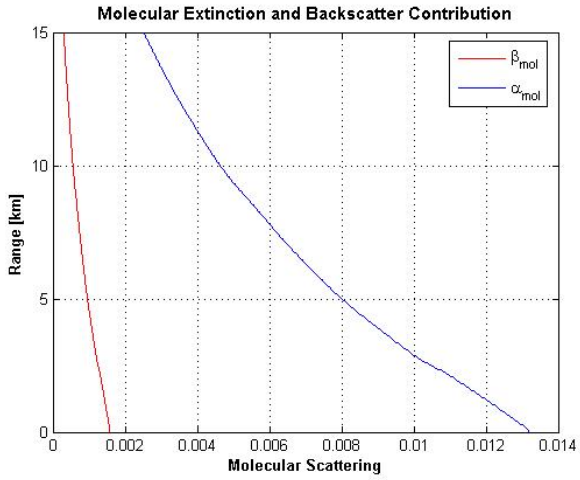

Figure 3-1: Molecular extinction and backscatter generated for upper air meteorological soundings (temperature and pressure) for a summer US Standard Atmosphere.

4. These variables are input into the Fernald and the lidar inversion is then performed, which depends on the following additional information:
    a. The aerosol backscatter coefficient, which can be estimated from the molecular profile.
    b. The lidar ratio for aerosol scatterers S_{aer} can be estimated given the AOD τ_{aer} from an AERONET sun-photometer.

Using these assumed conditions as an input to the inversion, the solution to the Fernald method is as follows [Fernald, 1984]:

$$\beta_{aer}(R)+\beta_{mol}(R) \quad = \quad \downarrow \quad \frac{\overline{P}(R)\exp\left[-2(S_{mol}-S_{aer})\int_{R_0}^{R_{max}}\beta_{mol}(R')dr'\right]}{\frac{\overline{P}(R_{max})}{\beta_{tot}(R_{max})}+2S_{aer}\int_{R_0}^{R_{max}}\overline{P}(R)\exp\left[-2(S_{mol}-S_{aer})\int_{R_0}^{R_{max}}\beta_{mol}(R'')dr''\right]dr'} \tag{3-17}$$

5. So, given the aerosol scattering ratio S_{aer} and the aerosol backscattering at the far end $\beta_{aer}(R_{max})$ are known, the lidar signal can be backward integrated to obtain $\beta_{aer}(R)$ and $\alpha_{aer}(R)$, the aerosol backscatter and extinction respectively as a function of range. Figure 3-2 shows the retrieved aerosol extinction profile, were S_{aer} was assumed to be 50.

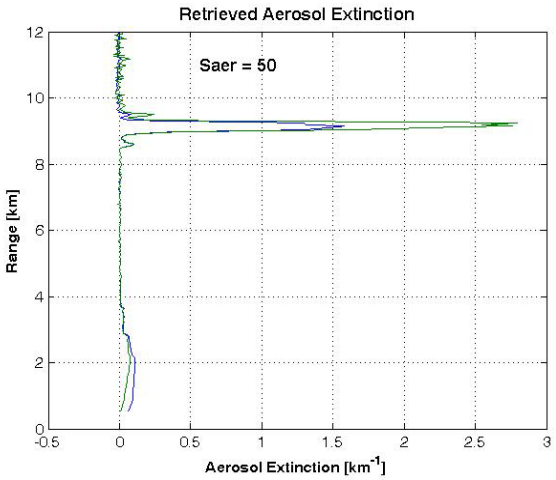

Figure 3-2: Retrieved aerosol extinction and backscatter, with extinction-to-backscatter ratio of 50.

3.5.1.2 ITERATIVE METHOD

The iterative method uses an inversion technique for the lidar signals by iteratively solving the lidar equation using Fernald's method. This method, like Fernald's method also requires prior knowledge of the aerosol type to fix the values that determine the lidar constants. The iterative convergence method determines the altitude profiles of aerosol extinction, which incorporates Fernald's inversion scheme

1. We assume distribution profiles from upper air meteorological soundings just as the Fernald method, from which the molecular backscatter is

obtained and the extinction-to-backscatter ratio calculated using the extinction/backscatter relationship. The calibrated lidar signal is representative of the total untenanted backscatter for each range bin:

$$\beta_{tot}(R) = \beta_{aer}(R) + \beta_{mol}(R) \tag{4-18}$$

2. The retrieved aerosol backscatter is simply the difference between the total unattenuated and molecular backscatter profile.
3. Once the aerosol type is fixed, the aerosol extinction profile is obtained from AERONET sun-photometer modeled relationship.

$$\alpha_{aer} = S_{aer}\beta_{aer} \tag{4-19}$$

4. For each range bin the total unattenuated backscatter is corrected for the molecular and aerosol extinction encountered below that range and which provides the corrected total unattenuated backscatter.

$$\beta'_{tot}(R) = \beta'_{aer}(R) + \beta'_{mol}(R) \tag{4-20}$$

5. Steps 1-4 are iterated to convergence of the integrated aerosol backscatter. In figure 3-3 we show a comparison of Fernald's to the iterative method upon convergence (10^{th} iteration), showing that at convergence the results of the two methods are no different.

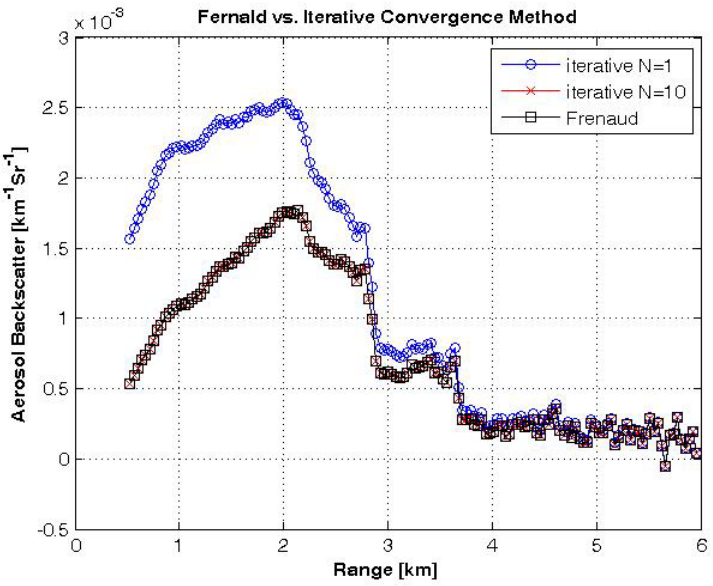

Figure 3-3: Comparison of Fernald's method (black squares) to the Iterative method (a) blue circles showing no convergence at first iteration, however (b) by the 10th iteration there was convergence.

3.5.2 LIDAR RATIO (S_{AER}) ESTIMATES

The procedure for obtaining the lidar ratio S_{aer} uses data from AERONET sun-photometers and is outlined below:

1. Using only the spherical mode , we can obtain the volume distribution and the complex refractive index from the sun-photometer database

$$\left[\frac{dV}{d\log(r)}\right],\ (m_r(\lambda), m_i(\lambda)) \tag{3-21}$$

2. We then calculate the aerosol optical depth for each distribution in the AERONET archive using the Mie theory:

$$\alpha L(\lambda) = \int_{r_{min}}^{r_{max}} \left(\frac{3}{4r}\right) Q_e\left(q = \frac{2\pi r}{\lambda}, m_r(\lambda), m_i(\lambda)\right)\left[\frac{dV}{d\log(r)}\right] d(\log(r)) \tag{3-22}$$

$$\beta L(\lambda) = \int_{r_{min}}^{r_{max}} \left(\frac{3}{4r}\right) Q_\beta\left(q = \frac{2\pi r}{\lambda}, m_r(\lambda), m_i(\lambda)\right) \left[\frac{dV}{d\log(r)}\right] d(\log(r)) \qquad (3\text{-}23)$$

3. The lidar ratio can then be calculated using the backscatter/extinction relationship as before.

The results of the S ratio for the 532 and 1064 channels are displayed in the figure 3-4 for a set of AERONET retrievals. We note that for AERONET retrievals, for aerosol optical thickness at the 440 nm channel (AOT(440) > 0.4) the S ratios are fairly stable at $70 \le S_{532} \le 90$. However, below optical thickness of 0.4 (AOT(440) < 0.4), a much more broadened range of S ratios are observed $40 \le S_{532} \le 80$.

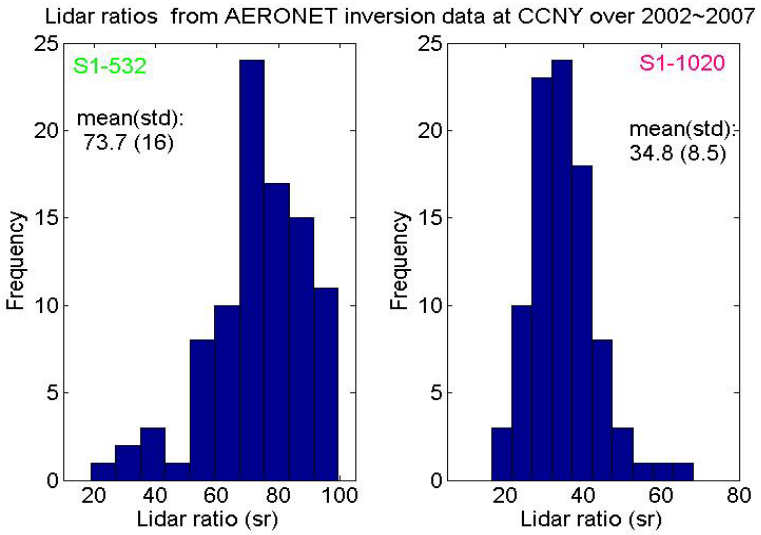

Figure 3-4: Top row represents the statistics of the S ratio at 532nm obtained from AERONET. Bottom row represents that for the 1064nm.

3.5.3 OPTICAL PARAMETERS DETECTED FROM LIDAR RETURNED SIGNAL

The detected signal from the lidar system is a result of both molecular and aerosol scattering. Therefore, the parameters to be derived are the backscattering coefficient and the extinction coefficient. These are optical parameters which depend on wavelength (λ). Other optical parameters can be derived too if the system is multi-wavelength, like the CCNY set-up. Some of the other optical parameters are:

i. The Angstrom Exponent A, which describes the wavelength dependence of the extinction coefficient:

$$\alpha_a = B\lambda^{-A} \tag{4-14}$$

ii. The aerosol optical depth (AOD), which is the extinction coefficient integrated over an atmospheric path :

$$\mathrm{AOD} = \int_{z_0}^{z} \alpha_a(Z)\partial z \tag{4-15}$$

These parameters and many more can be derived from lidar data with reasonable accuracy if the system has good alignment and stability, and the algorithm for data processing is optimized.

The typical unprocessed lidar signal has a large peak, where the laser the laser beam enters completely in the telescope field of view (FOV) at about 150m (figure 3-5). After the maximum peak the signal decreases exponentially provided there exists a clear atmosphere above.

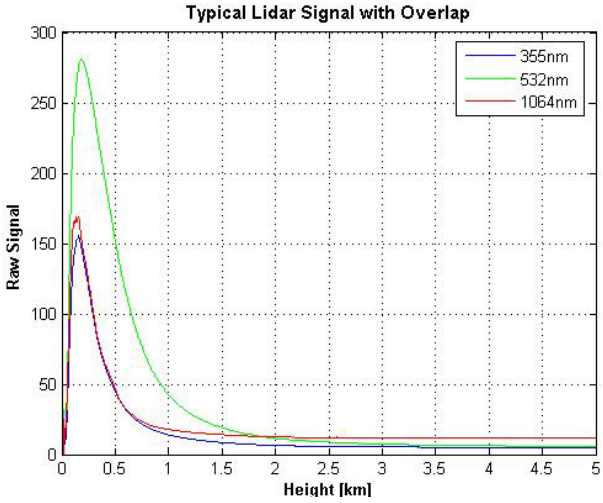

Figure 3-5: Typical lidar signal, and the overlap produced between the laser beam and the telescope mirror at 355, 532 and 1064 nm channels on April 10, 2006.

In figure 3.6 we shows a typical three dimensional images of the range corrected power measured by the CCNY multi-wavelength lidar for the 1064, 532 and 355 nm channels for a polluted day.

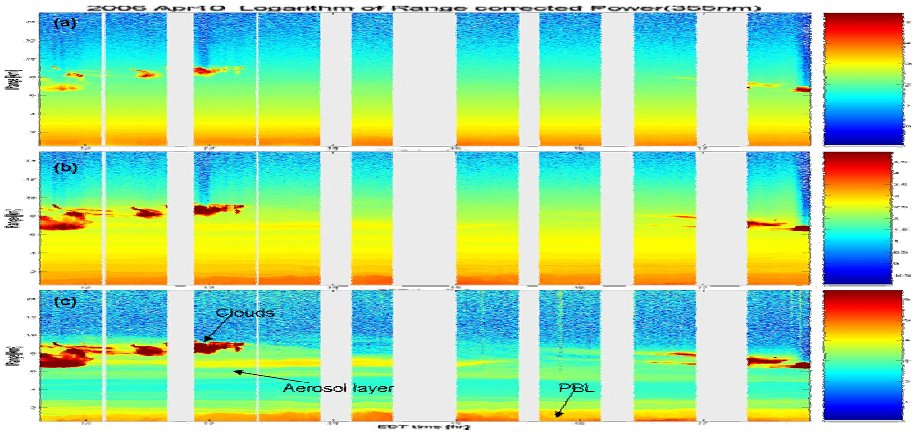

Figure 3.6: Multi-wavelength lidar range corrected power on April 10, 2006 at (a) 355 nm, (b) 532nm and (c) 1064 nm showing existence of plumes entrained aloft, a uniformly mixed PBL, and cirrus clouds above 11 km in the atmosphere above CCNY.

The strong wavelength dependence of Rayleigh scattering enhances the short wavelengths, making it difficult to identify features other than clouds. Small particles scatter a much higher percentage of short wavelength light than long wavelength light. In the Rayleigh scattering process, the atmosphere can be

treated as a collection of gas molecules that are randomly distributed relative to each other. Because the mathematical relationship involves the fourth power of the wavelength even a small wavelength difference can mean a large difference in scattering efficiencies.

This is emphasized in figure 3.6a where there is no visible evidence of the presence of aerosol layers. However, the longer wavelengths (1064 nm channel) removes the molecular background enabling easy identification of high altitude layers. For the 1064 nm channel in figure 3.6c, we can see a more polluted atmosphere with clearly visible high altitude layers compared to the shorter wavelength channels.

Applying the Fernald method we are able to retrieve the aerosol backscatter and extinction. In figure 3.7 we show a plot of a typical backscatter profile for the 532 nm channel at two time instances (3 minutes apart), where we observe the largest backscatter due to high altitude clouds (above 8 km), small aerosol backscatter (between 6 and 8 km), and a noticeable boundary layer backscatter compared to the background.

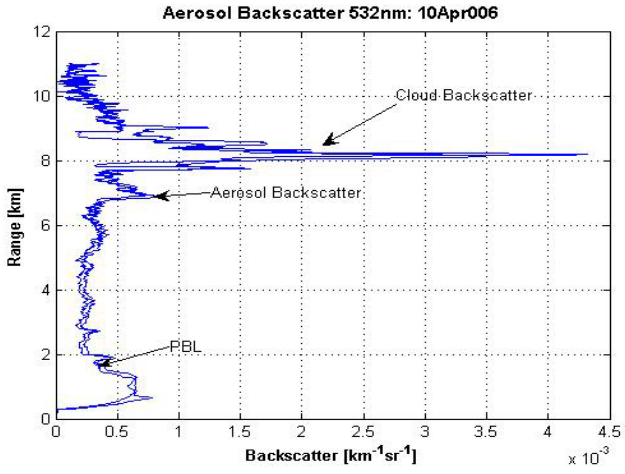

Figure 3.7: Lidar aerosol backscatter vertical profile at 1064 nm wavelength on April 10, 2006 at 12:34 and 12:37 PM EST.

The aerosol backscatter profile in figure 3.7 extends to approximately 11 km and corresponds to a 1 minute integration time (3000 laser shots) with a vertical resolution of 3.76 m. To retrieve the aerosol extinction (not shown) a lidar ratio of 50 was used.

3.6 CCNY Elastic Backscatter Lidar

At the City College of the City University of New York (CCNY), located at 40.8° N, 73.9° W, a backscatter Nd:YAG lidar system has been built and lidar profiles up to an altitude of 40 km have been obtained since 2002. The direct detection lidar, or Rayleigh lidar, is important for profiling the aerosol and molecular backscatter intensity. Rayleigh lidar techniques are the simplest to apply because only a simple laser transmitter and receiver are required; however the signals generally provide more qualitative and less quantitative information of the atmospheric properties. This technique can be used to detect and measure the distances to clouds and the number density distribution of aerosols.

3.6.1 LIDAR SETUP

Figure 3-8 shows the schematic of the lidar setup at CCNY, composed of a laser source, a receiving telescope, a signal-processing unit, and a data processor. Table 3.1 gives the specifications of the various subsystems. The lidar system uses a pulsed Nd:YAG laser with second- and third-harmonic-generation options.

The lidar consist of a transmitter, a receiver (telescope), and an Nd:YAG laser with a fundamental wavelength of 1064 nm, with a 1.2 joule output at the

fundamental wavelength, produces pulses of approximately 8 ns at 50 Hz. Frequency doubling with the nonlinear crystals converts the fundamental to 532 nm when the 1064 nm Nd:YAG fundamental interacts with the crystal to produce a secondary wave with half the fundamental wavelength. The resultant 532 nm wave is mixed with the residual 1064 nm fundamental to produce a 355 nm wave. Short pulses of light with length of a few to several nanoseconds are generated by the laser, which emits a pulse of light into the atmospheres by reflecting mirrors. The laser bean interacts with the intervening atmosphere, where some of the light is scattered back to the detector. The backscattered echoes are not seen by the telescope until the transmitted pulse crosses into and start overlapping with the telescope field of view, which occurs above approximately 500 m altitude.

The scattered light collected by the telescope is then transferred to the detectors. Beam splitters are used to separate the returned signals into 1064, 532, 355, 387, 407 nm components.

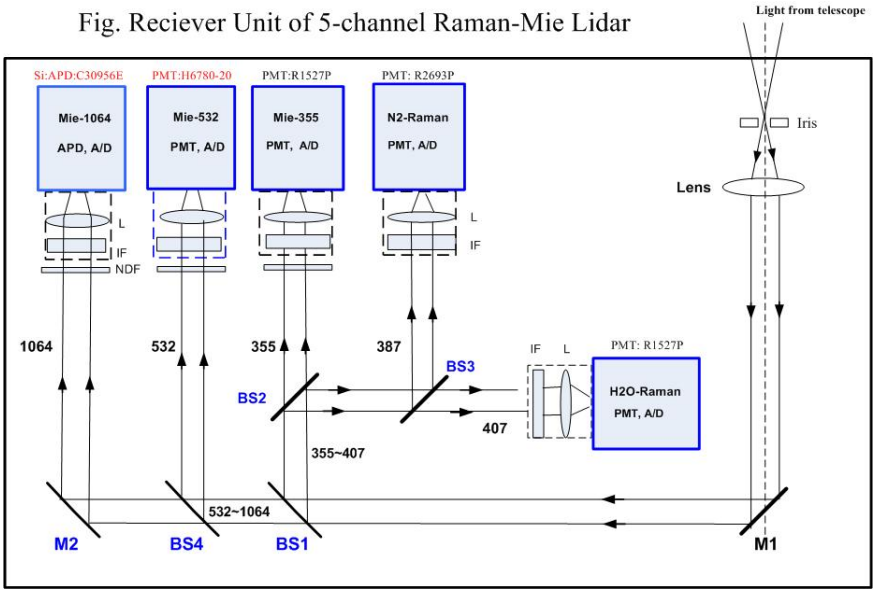

Figure 3-8: Schematic of the Lidar Detection System

3.6.2 LIDAR SYSTEM COMPONENTS

There are three sub-systems in the CCNY lidar setup, namely the transmitter, the receiver, and the data acquisition system. Figure 3-9 shows the block diagram of the system giving details of the setup and basic components of each sub-system, and Table 3.1 on page 42 details some of the laser and receiver parameters.

3.6.2.1 TRANSMITTER

The purpose of the transmitter is to generate light pulses and direct them into the atmosphere. It is an advantage for the lidar detection system to view as small an area of the sky as possible in order to keep the background (light detected by the lidar from other sources) low, particularly during daytime operation [Bisson et al. 1999 and Chen et al. 1997].

There are many reasons that make lasers the best light source for the transmitter. Firstly, both the transmitted light and the lidar returned signal from atmospheric scatters are attenuated. Secondly, there is a broad spectrum of background light sources such as sunlight which can enter into the receiver. A narrow light source combined with a narrow interference filter is necessary to eliminate most of the background contamination other than the backscatter signals. The pulsed laser possesses both of these desirable properties, and therefore makes it the best candidate for the lidar transmitter.

The CCNY multi-wavelength lidar uses a Spectra Physics Quanta-Ray PRO-Series pulsed Neodymium-doped Yttrium Aluminum Garnet (Nd:YAG) laser. Some of the properties are listed in table 3-1. The transmitter sub-system

includes the laser source, tuning mirrors, beam splitters, a half-wave plate and a polarizer.

3.6.2.2 RECEIVER

The CCNY receiver system for the lidar collects and processes the backscatter return and directs them onto photo detectors, and devices that convert the light into an electrical signal. The detector converts the light into an electrical signal, and the transient recorder processes and records the electrical signal. Photomultiplier tubes (PMTs) are used as detectors for the UV and visible light. The PMT converts the incident photons into electrical current, large enough to be detected by the sensitive electronics.

3.6.2.3 DETECTION SYSTEM

The detection setup of a lidar system takes the light from the receiver system and produces a permanent record of the measured intensity as a function of altitude. The detection system consist of Photo-multiplier tubes (PMTs), Avalanch Photo Diodes (APD), lenses, interference filters, mirrors, and beam splitters.

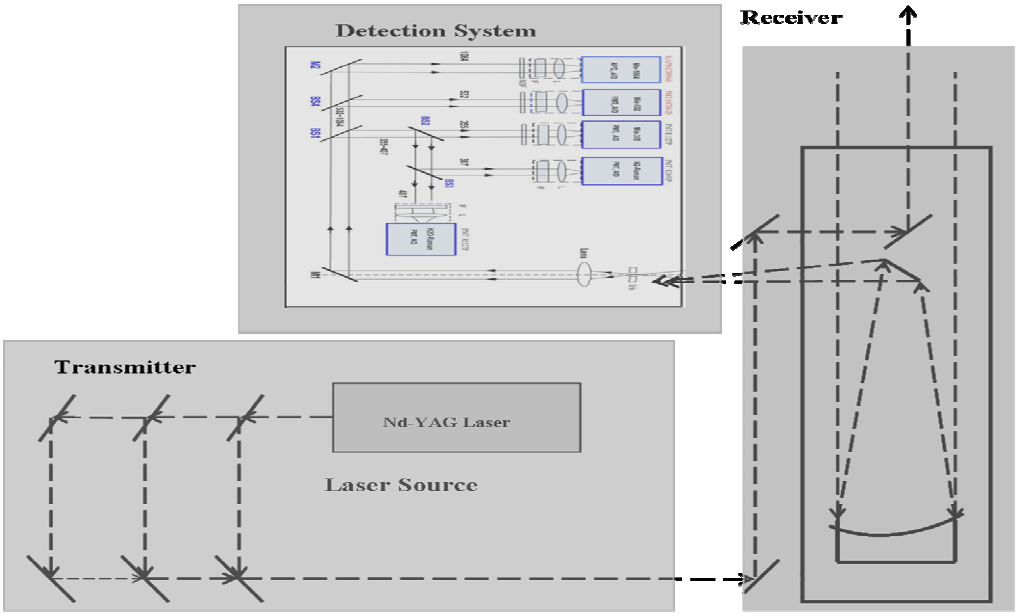

Figure 3.9: Block diagram of the CCNY multi-wavelength lidar configuration.

TRANSMITTER	
Pulsed Nd:YAG Laser ***Quantum-Ray PRO-Series***	
Fundamental Wavelength	1064 nm
Energy per Pulse	950 mJ :1064 nm 475 mJ :532 nm 300 mJ :355nm
Repetition Rate	30 Hz
Power	28.5 W :1064 nm 14.3 W: 532 nm 9.0 W: 355 nm
Pulse Width	8-12 ns :1064 nm 1-2 ns: 532 nm 2- 3 ns: 355 nm
Beam Divergence	< 0.5 mrad

RECEIVER	
NewtonianTelescope	
Aperture	50.8 mm
Focal Length	1778 mm
Hamamatsu Detectors	
355 nm 532 nm 1064 nm	PMT: R758-10 PMT: R758-10 APD
Data Acquisition	
Transient Licel	

Table 3.1: Specifications of the CCNY lidar system.

3.7 SUMMARY

The CCNY multi-wavelength lidar system is designed to measure elastic (355, 532, 1064 nm) and inelastic (387, 407 nm) backscatter signals from the atmosphere above, with signal returns up to 14 km. The system has been operated at least 3 days a week during fair weather conditions since 2002. The system will be modified in the near future to extend and improve its capabilities, including measurement of tropospheric ozone at 266 nm.

REFERENCES

Bisson, S. E, J. E. M. Goldsmith, and M. G. Mitchell, "Daytime Raman lidar profiling of atmospheric water vapor", Appl.Opt. **38**, 1,841–1,849 (1999).

Chen H. et al., Opt. Lett. **21**, 1,093–1,095 (1997).

Fernauld, F. G., "Analysis of Atmospheric Lidar Observations", Applied Optics, VOL. 23, pp. 652, 1984.

Gobbi, G. P., F. Barnaba, R. Van Dingenen, J. P. Putaud, M. Mircea, and M. C. Facchini, "Lidar and in situ observations of continental and Saharan aerosol: closure analysis of particles optical and physical properties", Atmos. Chem. Phys., 3, 2161-2172, 2003.

Kovalev, Vladimir A., and William E. Eichinger, "Elastic Lidar: Theory, Practice, and Analysis Methods", 2004

Weitkamp, C., "LIDAR: Range-Resolved Optical Remote Sensing of the Atmosphere," Springer Series in Optical Science, VOL. 1, 2005.

4. LIDAR METEOROLOGY

METEOROLOGICAL FEATURES REVEALED BY THE CCNY LIDAR

4.1 INTRODUCTION

Atmospheric processes play a major role in determining the fundamental properties of climate as the deposition of incoming solar radiation, temperature of the earth's surface, and much more [Wallace et al., 2006]. It is also known that optical and physical properties of atmospheric aerosols, such as optical depth, particle size, number density, single scattering albedo, etc., play an important role in the Earth's climate and radiation budget [IPCC, 2001].

The study of atmospheric aerosols is important for a variety of reasons. Aerosols influence the climate directly by altering the radiative energy transfer through their optical properties and secondly, the inhomogeneous space–time variability of aerosol provides unique information on atmospheric behavior needed for environmental research and operational programs. A lot of interest in atmospheric aerosols has been stimulated by the presence and impact of anthropogenic emissions associated with many urban environments, and it is therefore of public concern [IPCC, 1995]. The impact of aerosols on the global, regional, and local weather and climate, and satellite remote sensing has been the subject of numerous investigations in recent years [Charlson *et al*., 1992; Harshvardhan, 1993].

While aerosols may affect local weather, it is also clear that the interrelationship can go both ways and local meteorology can significantly modify

aerosol formation. For example, sea breeze circulations have the ability to significantly modify the atmospheric boundary layer by replacing the existing air mass with low level incursions of cool moist air. Elevated wind speed and changes in wind direction that can either increase or diminish the concentrations of chemical constituents [Clarke et al., 2004]. Gedzelman et al. (2006) has explored some of the characteristics of sea breeze fronts on the Planetary Boundary Layer for two cases over CCNY (data obtained by the CCNY lidar) by making connections with changes the mixed layer height, and from MODIS Aqua observation real time images of formation of a line of cumulus clouds where the surface winds converge with the leading edge of the front.

Through its high spatial and temporal resolution, the lidar technique is a helpful tool for monitoring the evolution of the basic meteorological and atmospheric parameters. The lidar technique has become a very powerful tool to visualize, in real time, the atmospheric transport processes, especially over coastal urban areas (land-sea breeze circulation), using the aerosol particles as tracers. Secondly, to visualize in real time, the vertical distribution of aerosol particles, either produced locally over the measuring site or transported by atmospheric circulation (land-sea breeze circulation, trans-boundary air pollution, desert dust events etc.), and thirdly, the structure of the lower atmosphere (structure of the PBL, identification of several aerosol dust layers), and its correlation with ground air pollution levels.

The detection and analysis of the backscattered lidar signals permits the retrieval of the relative concentration of the suspended aerosol particles, and of the absolute concentration of several air pollutants, with very high temporal and

spatial resolution along the propagating laser beam. The lidar technique is an efficient tool for continuous monitoring of clouds and aerosols in conjunction with local, regional and global climate studies. Lidars are needed to provide long-term accurate data on cloud heights, optical depth and their spatial distribution.

Lidar is also a valuable tool for weather analysis when used with standard meteorological measurements, as well as radar and satellite imagery. In this section, we present some of the meteorology connected to some of the atmospheric features and conditions observed by the CCNY multi-wavelength lidar. We will also present a climatological study using a number of lidar observations.

4.2 AEROSOL CLIMATOLOGY

The aerosols present in the atmospheric boundary-layer, particularly in the lowest air layers (up to 200 m), contribute greatly to the overall loading at a given site, and thus the boundary-layer aerosol information is of paramount importance.

4.2.1 AEROSOL CHARACTERIZATION

Aerosol Optical Depth (AOD) is a useful parameter for characterizing the atmosphere in terms of column-integrated aerosol density. The vertical distribution and general physical properties of aerosols are also very important factors in understanding aerosol transport climatology. A general consensus on the need for systematic and coherent monitoring of aerosol vertical loading variations has led to the development of a number of networks throughout the

globe. The most important of these networks is the NASA worldwide federated network of sun-photometers (AERONET, for AERosol RObotic NETwork).

4.3 LIDAR CLIMATOLOGY

Lidar is an excellent tool for providing data on the vertical distribution of aerosol scattering properties. We investigate weather features in NYC, in particular over CCNY using the CCNY lidar vertical profiles of tropospheric aerosol content.

From March 18, 2005 to October 16, 2006 the CCNY lidar operated on 143 clear or partly cloudy days. Out of those days of operation, the planetary boundary layer (PBL) was always identifiable; clouds were present in the scene less than 63% of the time. Of those 143 days, 114 days of distinct haze layers were identifiable above the PBL, 84 days of waves on haze layers and 14 days of sea breeze fronts. The statistics are detailed in table 4.1.

Features Recorded	#Days	%
Atmospheric Boundary Layer (ABL)	143	100
Cirrus or Cirrostratus	76	53
Altocumulus or Altostratus	22	15
Cumulus or Stratocumulus	88	62
Distinct Haze Layers above ABL	114	80
Waves on Haze Layers	84	59
Sea Breeze Fronts	14	10

Table 4.1: CCNY lidar climatology statistics identifying climatology featured from the 3-D data plot including the Atmospheric Boundary layer (ABL), Cloud classification, Haze layers, Gravity waves on haze layers, and sea breeze frontal passages.

The PBL was the most prominent and dominant feature visible in the vertical lidar profile. In most observations the top of the PBL is marked by an abrupt change in the range corrected power and can be verified with a marked temperature inversion (a meteorological situation where temperature increases with height) in upper air soundings. Inversions separate the PBL from the free troposphere and in some cases the transition is not well defined. In figure 4.1a we display a CCNY 3-D lidar vertical profile of the range corrected power on a logarithmic scale on January 11, 2007, showing the complexity of the atmosphere above. Coupled with this we show (figure 4.1b) the upper air sounding at 13:00 EST above CCNY (courtesy: Wyoming University Weather).

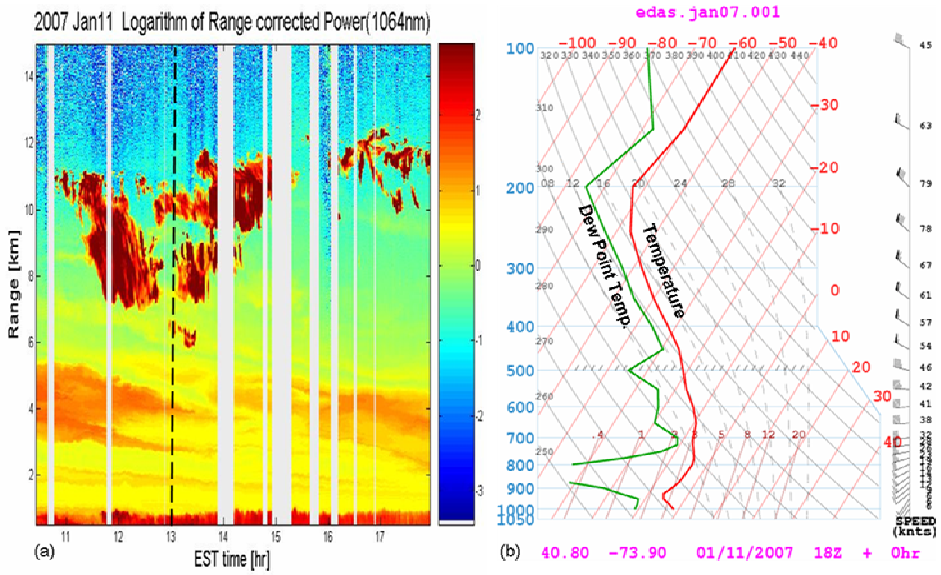

Figure 4.1: (a) CCNY lidar 3-D vertical profile of the range corrected power on a logarithmic scale on January 11, 2007 showing a complex atmosphere above and (b) An example of an early afternoon, 18Z sounding from CCNY showing a temperature inversion between 1000 and 950 hpa, very dry and humid region between 900 and 750 hpa, and a thick precipitation layer above 450 hpa. (Courtesy: Wyoming University Weather).

The temperature on a Skew-T Log-P diagram aids forecasters in finding out how air parcels will move. In this plot temperature increases with height, most commonly called a temperature inversion in meteorology can give forecasters an

almost instantaneous look at where clouds and moisture layers can be found. Therefore the lidar 3-D vertical profile coupled with the upper air sounding are very useful in identifying and classifying meteorological features.

In figure 4.1b we can see a large deviation between the dew point temperature and the ambient temperature, which is indicative of dry air with confined aerosol layers. Quantitatively, when there is a large distance between the ambient temperature and the dew point temperature, the air in that region is dry and relative humidity values are low. Conversely; when there is a small distance between the ambient temperature and the due point profile, the air in the region is moist and relative humidity values are high – especially near or up to 100 percent – clouds can easily form. This is seen in the sounding in figure 4.1b above 450 hpa which is in agreement with the cloud layers seen above 6 km in the lidar image (figure 4.1a). In figure 4.1 the atmospheric sounding validates the features seen in the lidar image.

4.3.1 BOUNDARY LAYER HEIGHT

The atmospheric boundary layer height is a fundamental parameter characterising the structure of the lower troposphere. The determination of this parameter is important in applications that range from meteorological modeling and forecasting to dispersion problems of atmospheric pollutants. Since substances emitted into the atmospheric boundary layer are dispersed horizontally and vertically through the action of turbulence, they are well-mixed over this layer that is widely known as the "mixing layer".

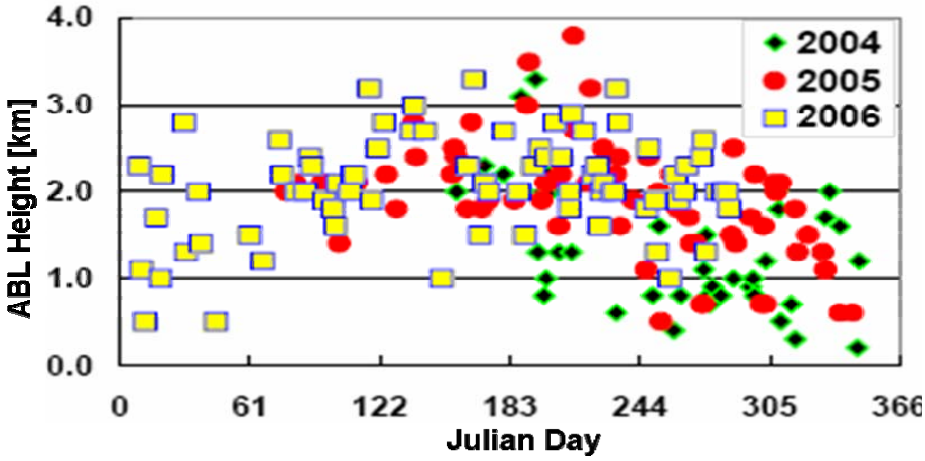

Figure 4.2: Maximum Atmospheric Boundary Layer Height for each CCNY lidar observation day for 2004 (green diamonds), 2005 (red circles), and 2006 (yellow squares) [Gedzelman et al. 2006].

In figure 4.2, the atmospheric boundary layer height was obtained by taking the maximum value of the height of the ABL per day for 187 days between 2004 and 2006 from lidar measurements [Gedzelman et al. 2006]. In most cases the atmospheric boundary layer is marked by a sharp change (reduction) in the signal (backscatter) returns from the lidar and at times by a cumulus (Cu) or stratocumulus (Sc) cloud capped boundary layer. The lidar PBL height in figure 4.2 is in close agreement with heights based on thermodynamic soundings obtained from ARL/NOAA HYSPLIT models. We also see the annual cycle attached with the PBL height which peaks during the summer, at the times when surface radiation heating is at its highest for the year. This trend can be observed in all three years (2004-2006) studied.

It is commonly understood that the atmospheric boundary layer evolves from a thin layer in the early morning to a distinct rapid growth (thicker) by afternoon. However, due to the urban heat island effects, we have also noted a strong persistence of the PBL layer into the night, reducing especially in summer

the diurnal cycle. However, on some spring and summer days, we find the height of the boundary layer can increases rapidly, which is indicative of a sea breeze frontal passage which is most often marked by a transition to a cloud capped PBL.

4.4 CASE STUDIES OF FRONTAL PASSAGES OVER NYC

Sea breeze circulations have the ability to significantly modify the atmospheric boundary layer by replacing the existing air mass with low level incursions of cool, moist air, elevated wind speed, and changes in wind direction that can either increase or diminish the concentrations of chemical constituents depending on the relative difference between the in-situ and upstream properties [Clark et al., 2002].

4.4.1 JUNE 13, 2006 SEA BREEZE FRONT

In figure 4.3 we can observe the growth in the PBL from about 1 km to a little higher than 2 km between 1400 and 1500 UTC as a sea breeze frontal passage made its way over NYC, which is also marked by the open cumulus cloud capped PBL in the lidar image. The frontal passage was evident in the lidar 3-D vertical profile by an abrupt increase in the boundary layer height with open cumulus cloud capped PBL.

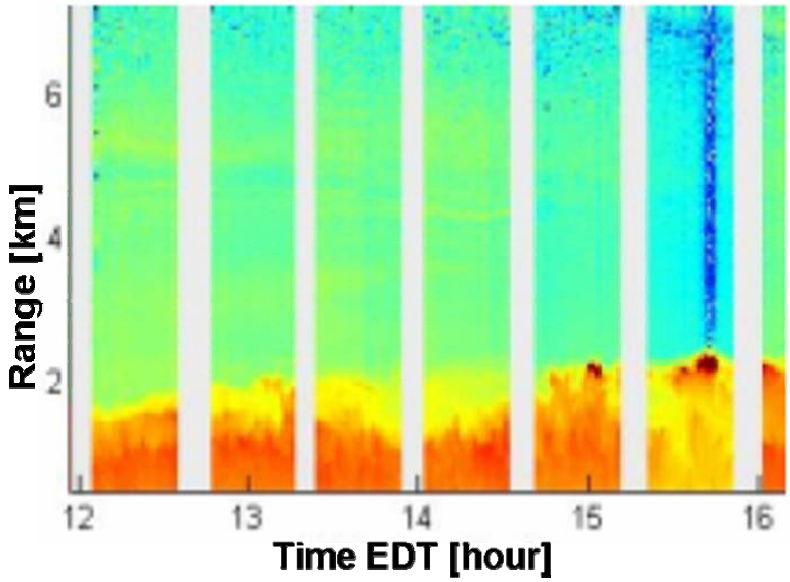

Figure 4.3: June 13, 2006 CCNY lidar 3-D vertical profile up to 4 km from 1400 to 1630 EDT showing an increase in the ABL height at the time of the sea breeze frontal passage, where cumulus clouds are identified by the largest backscatter (darkest pixels).

During this period the CCNY surface weather station recorded changes in wind speed, wind direction, temperature and relative humidity. Figure 4.4 shows the time series of these variables for a 24 hour period. The dotted line identifies the approximate time of the frontal passage. The temperature decreases from about 27^{o}C to about 22^{o}C, a 5^{o} drop, with a simultaneous increase in relative humidity from approximately 30% to approximately 65%. The wind direction changed from slightly west-northwest (WNW) to slightly south-southwest (SSW) and the wind speed increased from <2ms^{-1} before arrival of the front to almost 7ms^{-1} just behind the front.

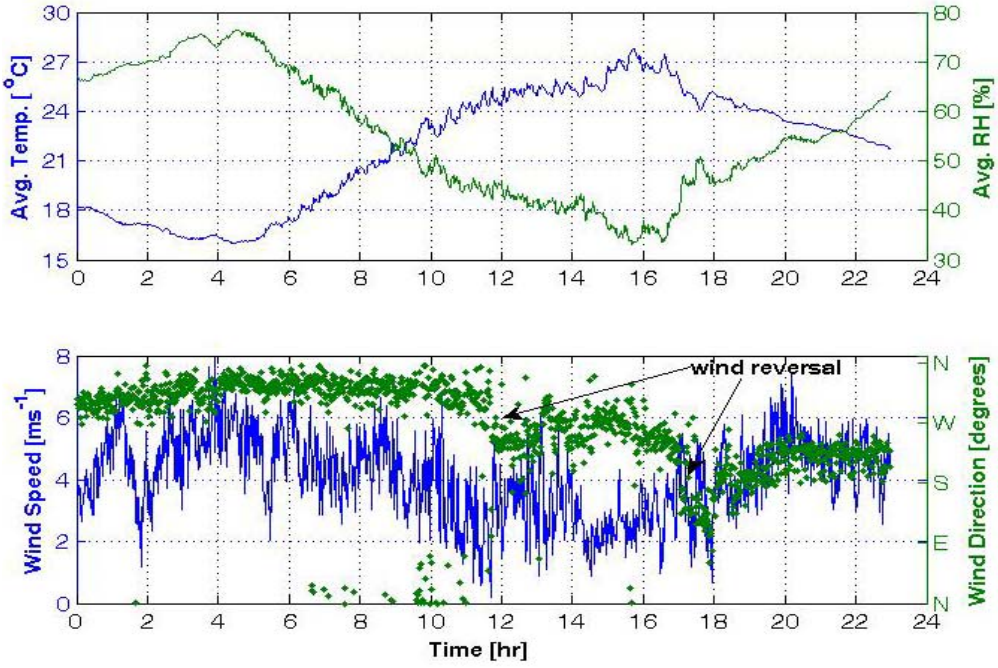

Figure 4.4: Time series of (a) top panel, temperature (blue line) and relative humidity (green line) and (b) bottom panel, wind speed (blue line) and wind direction (green line) during the passage of the leading edge of a sea breeze front on June 13, 2006

As a means of verifying these features observed in the lidar 3-D vertical profile of the atmosphere, we looked at the MODIS Aqua image at 1340 EDT (Figure 4.5) where we can observe a line of cumulus clouds formed where the surface winds converged at the leading edge of the front. These features can also be observed in Figure 4.6 of the simulations from the Weather Research Forecast (WRF) model which was run for 24 hours for June 13, 2006 [Gedzelman et al. 2006].

Figure 4.5: MODIS Aqua image on June 13, 2006 at 1740 UTC showing cumulus cloud lines at sea breeze front on Long Island.

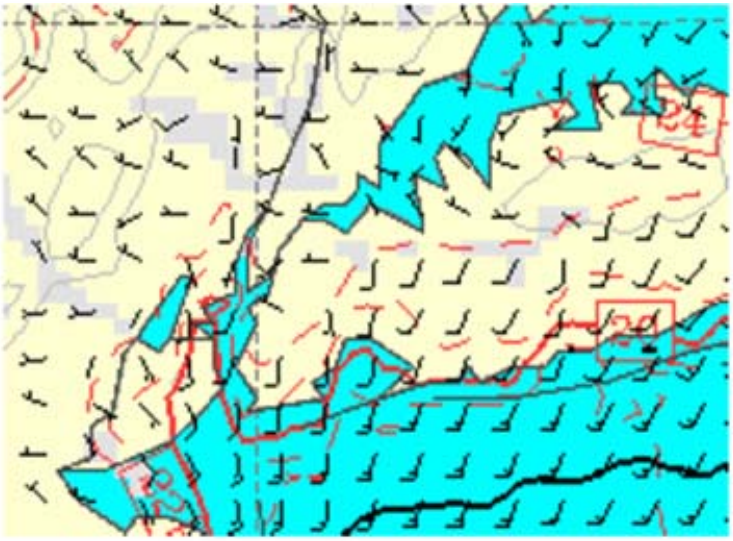

Figure 4.6: Weather Research Forecast (WRF) model generated surface map on June 13, 2006 showing wind (barbs), clouds (gray shading), and temperature (^{o}C, red line).

4.4.2 JUNE 21, 2006 SEA BREEZE FRONT

In figure 4.7 we can observe the abrupt growth in the PBL from less than 1 km at the beginning of lidar measurements to approximately 2 km by mid day as a sea breeze frontal passage made its way over NYC, which is also marked by the open cumulus cloud capped PBL in the lidar image. Also notice that the PBL

remained consistently stable and homogeneous through the remainder of the day.

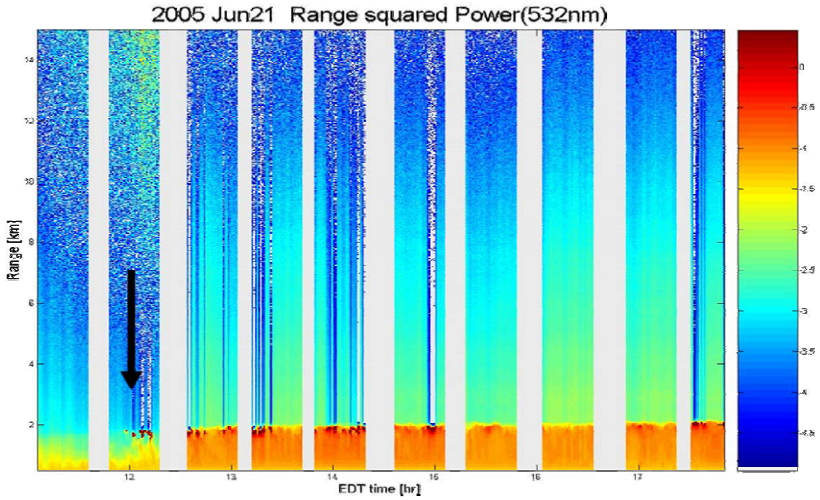

Figure 4.7: June 21, 2006 CCNY lidar 3-D vertical profile up to 14 km from 1100 to 1800 EDT showing an abrupt increase in the ABL height at the time of the sea breeze frontal passage, where cumulus clouds are identified by the largest backscatter returns (darkest pixels).

The NOAA/ARL HYSPLIT modeled sounding over CCNY at 1800 UTC on June 21, 2006, as shown in figure 4-8 indicates a near surface inversion with southwesterly winds from the surface to 250 hpa, except between the inversion and the dry layer at 750 hpa, where the winds blow from the north west, which may be indicative of a frontal passage.

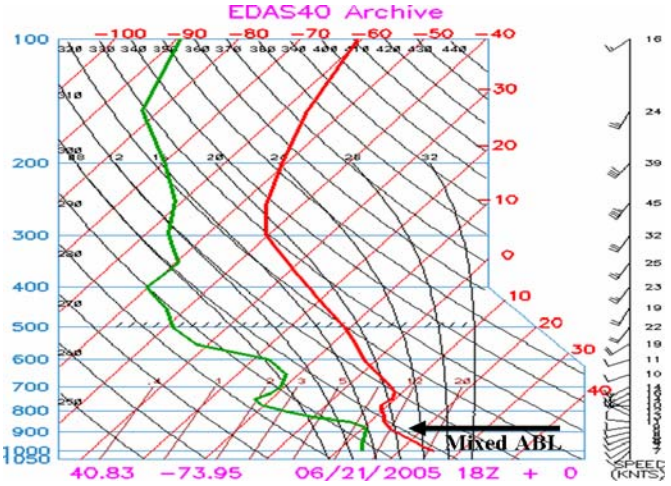

Figure 4.8: ARL/NOAA HYSPLIT model sounding on June 21, 2006 at 1800 UTC showing agreements in ABL with the lidar.

As discussed in the previous case, Figure 4-9 shows a decrease in temperature from approximately 28^{o}C to about 22^{o}C with an increase in relative humidity from 35% to 70%, a 45% increase in humidity. We also observed a wind reversal from west-southwest (WSW) to slightly east-southeast (ESE), almost a 180^{o} change in wind direction at the surface. There was also a simultaneous increase in wind speed from < 4ms^{-1} before arrival of the front to approximately 9 ms^{-1} just behind the front.

As explained in case 1 above, as a means of verifying the features observed in the lidar 3-D vertical profile of the atmosphere, we looked at the MODIS Aqua image at 1545 UTC (figure 4.10) where we can observe a line of cumulus clouds formed over Long Island (similar situation as case 1) where the surface winds converged at the leading edge of the front.

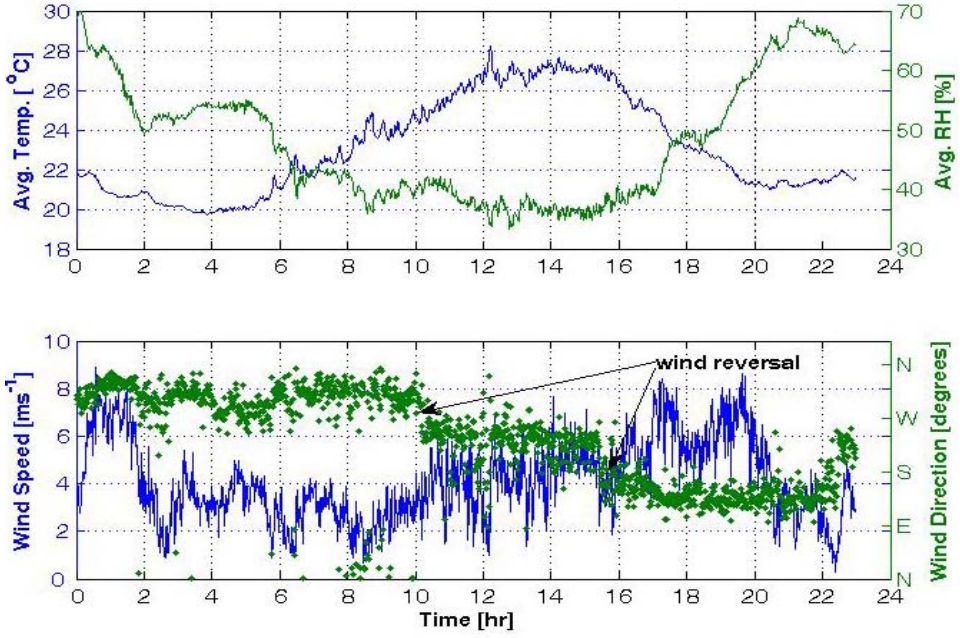

Figure 4.9: Time series of (a) temperature (blue line) and relative humidity (green line) and (b) wind speed (blue line) and wind direction (green line) during the passage of the leading edge of a sea breeze front on June 21, 2005.

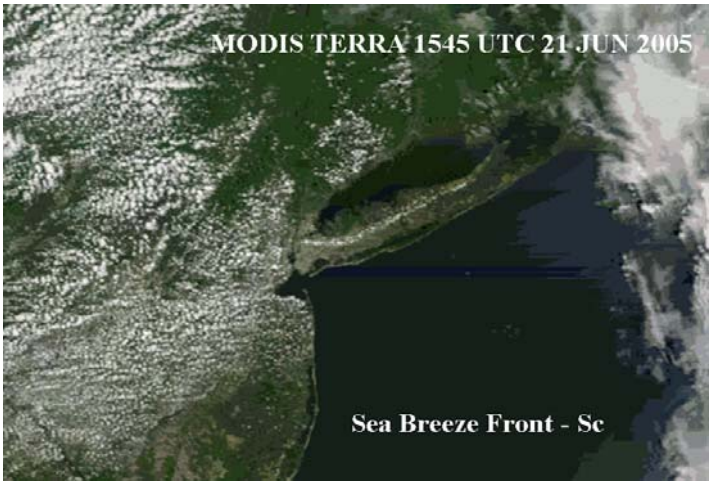

Figure 4.10: MODIS Aqua image on June 21, 2006 at 1545 UTC showing cumulus cloud lines at sea breeze front on Long Island.

4.5 SUMMARY

LIdar has the capability of measuring the time sequence of meteorological conditions and events which provides a more useful measure and interpretation of atmospheric behavior than conventional techniques, particularly when coupled with upper air soundings and backward trajectories.

Lidar observations also indicate a general persistence of the boundary layer over night, which is different from the normal diurnal cycle model of the PBL. This is primarily due to urban island heat effects which clearly lead to a poor prediction of surface level $PM_{2.5}$ since the mixing layer heights are clearly overestimated in the morning.

LIDAR is an excellent tool (when used in conjunction with other meteorological measurements) for determining atmospheric structure including the Atmospheric Boundary Layer, clouds and aerosol layers aloft. Lidar measurements also seem to form a connection between local meteorology and PBL dynamics; in particular, sea-breeze events can affect the dynamics of the

PBL layer. Abrupt increases in the height of the ABL accompanied by cumulus clouds above CCNY occur mainly on (late spring and summer) days and generally mark the passage of sea breeze fronts.

REFERENCES

Charles, L., S. et. al., "Application of CCNY Lidar and ceilometers to the study of Aerosol Transport and PM2.5 monitoring". Amer. Meteor. Soc., 3rd Symposium on Lidar Atmospheric Applications, 2007.

Charlson RJ, Schwartz SE, Hales JM, Cess RD, Coakley Jr JA, Hansen JE, Hoffman DJ. 1992. "Climate forcing by anthropogenic aerosols", Science **255**: 423–430.

Gedzelman, S. D., et. al., "Mesoscale weather features in NYC revealed by CCNY Lidar". Amer. Meteor. Soc., 6th Symposium on the Urban Environment, 2006.

Hashvardhan et al., "Aerosol–climate interactions. In Aerosol-Cloud-Climate Interactions", Hobbs PV (ed.). International Geophysics Series vol. 54. 75–95, 1993.

Houghton JT, Meira Filho LG, Callander BA, Harris N, Kattenberg A, Maskell K (eds), "The Science Climate Change", IPCC (Inter-Governmental Panel for Climate Change), Cambridge University Press; 572 pp., 1995.

Kiehl JT, Briegleb BP., "The relative roles of sulfate aerosols and greenhouse gases in climate forcing", Science **260**: 311–314, 1993.

Nelson, N., "The Impact of Weather on Pollution", Indoor Built Environment, VOL 9, 1-4, 2000.

Penner JE, Charlson RJ, Hales JM, Laulainen NS, Leifer R, Novakov T, Ogren J, Radke LF, Schwartz SE, Travis L., "Quantifying and minimizing uncertainty of climate forcing by anthropogenic aerosols", Bulletein of the American Meteorological Society **75**:375–400, 1994.

Richard D. Clark**, "**Modification of surface and boundary layer meteorology and chemistry by seabreeze incursions during NE-OPS", 2002.

Taylor K, Penner JE., "Response of the climate system to atmospheric aerosols and greenhouse gases", Nature **369**: 734–737, 1994.

Wallace, John M. and Peter V. Hobbs, "Atmospheric Science: An Introductory Survey", International Geophysics Series, VOL. 29, 2nd Ed., 2006.

5 SMOKE TRANSPORT

Atmospheric transport of smoke particulates and its interaction with the planetary boundary layer as observed by multi-wavelength lidar and supporting instrumentation

5.1 INTRODUCTION

Smoke aerosols are one of the main atmospheric constituents that affect air quality as well as the Earth's climate system. Although forest fires are generally local phenomena, they can also contribute to changes of the atmosphere on a regional or even global scale by generating large amounts of aerosol particles (Charlson et al., 1992; Taylor and Penner, 1994) which can be transported over large distances. Clearly, remote sensing observations from Geostationary satellites of forest fires are quite useful in determining the spatial extent and transport of plumes but are currently not capable of determining the source of the plume directly without relying on backward trajectory analysis, which may not be completely accurate. To determine the nature of the aerosol plumes, a number of more advanced multi-spectral satellites including OMI, POLDER, and MODIS to name a few have the added capability of improved aerosol classification.

Fire hotspots and smoke plume signatures are readily seen in satellite imagery, and many satellite sensors like GOES, MODIS [Kaufman et al. 1997] and TOMS [Torres et al., 1998; and Herman et al., 1997] are widely used to map the geographical distribution and characterization of aerosol transport on all scales. MODIS and TOMS (sun synchronous polar orbiting satellites) provide global coverage approximately once a day and can only provide snap-shots of

large-scale aerosol spatial distribution during the time of satellite overpass, which is not very suitable for tracking and monitoring large scale aerosol events. On the other hand, although GOES (Geostationary satellite) has a single channel, unlike MODIS and TOMS, it provides coverage of the entire globe at 30 minute intervals providing a summary of the extent of aerosol coverage, which gives a strong indication of the aerosol intensity. This gives GOES the advantage of being useful in tracking the time-history and spatial distribution of aerosol transport. Important features may sometimes go unnoticed by sun synchronous satellites, making it challenging and sometimes difficult to complete a picture. GOES can then further be used to validate features common to MODIS and OMI imagery. The goal is to use the GOES AOD product to identify transport by utilizing its multi-time passes in a single day to verify features which are common in geographical area to MODIS and OMI.

In particular, we unambiguously show that long term advected smoke plumes can either be transported aloft without any interaction with the PBL, or can mix with the PBL and change the air quality parameters at the surface. In fact, we show that a combination of passive and active ground instruments and satellite measurements respectively is needed to provide a unique and clear picture on how PBL aerosols can be affected by plumes mixing down into the PBL.

In both interacting and non interacting plume cases, lidar measurements are critical to properly apportion the PBL AOD contributions from the total column and to connect it to surface PM. In particular, due to the presence of these aerosol plumes as well as poorly mixed aerosols in the PBL, relating satellite

derived AOD to surface level air quality measurements such as PM2.5 or PM10 would lead to a great error. Therefore, efforts such as the IDEA product, which attempt to connect satellite AOD measurements directly to PM2.5 using the static relationship between AOD and surface PM2.5 measurements:

$$PM\,2.5 = 60\tau \tag{5-1}$$

must only be considered as a rough estimate.

5.2 AUGUST 2007 NORTHWESTERN UNITED STATES: IDAHO AND MONTANA FOREST FIRES

To illustrate the phenomenon, we choose the mid August 2007 fires which were continuously burning across Idaho and Montana with columns of thick smoke transported eastwards across North America, affecting much of the United States. Although it was assumed that this event significantly affected air quality in the north east, observations from satellites are not conclusive and in fact during the plume transport, surface samplers often showed low pollutant levels. The advanced warning provided by the satellites was crucial to ensuring that this transport event captured by the CCNY multi-wavelength lidar as well as other lidars from the Micro-Pulse Lidar Network (MPLNET).

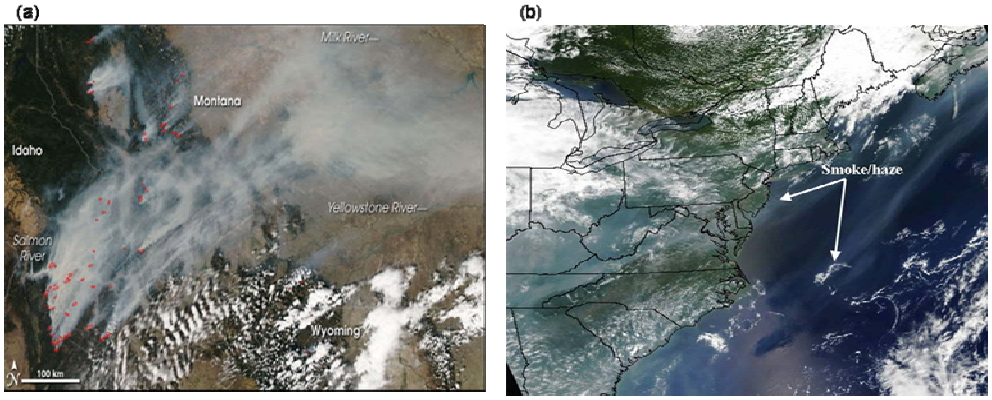

Figure 5.1: (a) Images showing smoke and fires area (Montana and Idaho) captures by MODIS aboard Aqua satellite on August 13, 2007. This image of the area was captured by MODIS on NASA's Aqua satellite at 2:00 p.m. local time (U.S. Mountain Daylight Time). Locations where that sensor detected active fires are highlighted in red. (b) MODIS Terra close-up view of the smoke and haze over the Great Lakes and the northeastern United States on August 15, 2007 at 1625 UTC.

The plumes were initially transported as high altitude lofted layers which was observed by the City College of the City University of New York (CCNY, 40.8N, 73.9W) lidar over two days and was subsequently observed to mix with the late afternoon planetary boundary layer (PBL). The source of the plume is shown in Figure 5.1(a) as fire hot spots and smoke signatures captured by MODIS onboard the Aqua satellite on August 13. By August 14 and 15 , the smoke plumes began to spread over the Northeastern United States as seen in figure 1b and were visually identifiable from the quick view imagery, as well as through the large AOD measurements seen from the GOES and MODIS satellites.

5.3 SATELLITE OBSERVARTIONS OF AEROSOL PLUME SOURCE, EXTENT AND PROPERTIES

In this section, we explore in more detail the plume observations from multiple satellite platforms. We find in particular that as discussed in the

introduction (1.2) the combined use of MODIS, OMI and GOES measurements clearly detail the magnitude and constituents of the plumes as biomass burning smoke. The plume transport is also clearly correlated to 48 hour predictions from NOAA's Air Resource Laboratory (ARL) HYSPLIT dispersion model. However, the connection of surface air-quality parameters to the observations and models are not satisfactory as shown in section 4 and as already emphasized, require supplemental lidar measurements to repartition the aerosol between aloft plumes and PBL.

5.3.1 Identification of Aerosol Transport Source Region

Modeled backw-trajectories provide a means to identify of the source region and the transport patterns of the air parcels at varying altitudes as specified by lidar observations. In Figure 5.2, we show the back-trajectory of the air parcels over 120 hr from CCNY for August 14 and 15, illustrating the horizontal and vertical motion of the air mass. The trajectory results show the air mass interacting with the lofted layers from the Idaho and Montana forest fire regions. This back-trajectory mode then allowed us to run HYSPLIT in prediction mode, which can then be compared to observations

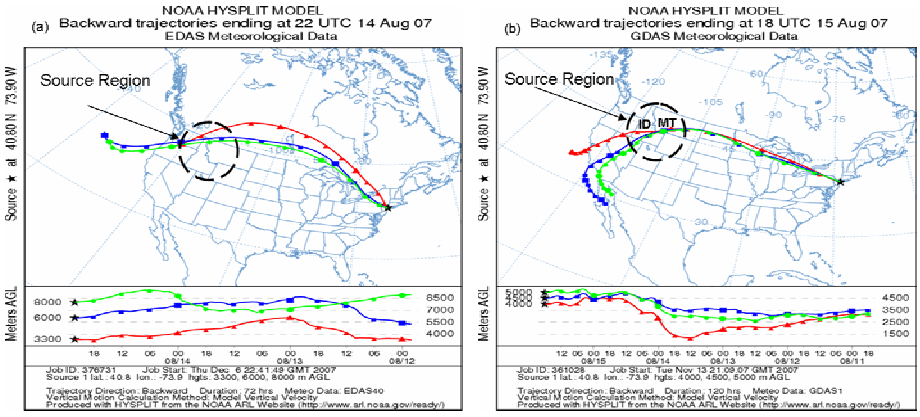

Figure 5.2: HYSPLIT 5-day backward trajectory analysis ending at (a) 2200 UTC on August 14 at three altitudes between 3 and 8 km and (b) 180 UTC on August 15, 2007 between 4 and 5 km.

5.3.2 MODIS Observations

Running the smoke forecast tool produced by ARL using the HYSPLIT dispersion model with the MODIS aerosol loadings shows clearly how well the model performs. In particular, MODIS aerosol retrieval continuously shows high aerosol optical depth over the source region over all three days (figure 5.3b, d, f). Details of the MODIS retrieval algorithm can be found in appendix A. However, we can see that on August 13 in figure 3b, very low aerosol loadings over the NYC region, implying that the smoke plumes had not made its way to this area as yet, as predicted by the model. On the other hand, we can see much higher aerosol loading on the 14th and 15th August (figures 3d and f) which is consistent with the CCNY lidar observations and model predictions. The quality of the predictions is also seen in the timing of the plume front. A more careful examination of the observations and model predictions show that by 1600 UTC, the plumes were first making their way into central New York State and did not make it into the New York City Area. This is consistent with the timing of the

plumes observed from the City College instrumentation suite where the first plumes were seen at 2000 UTC.

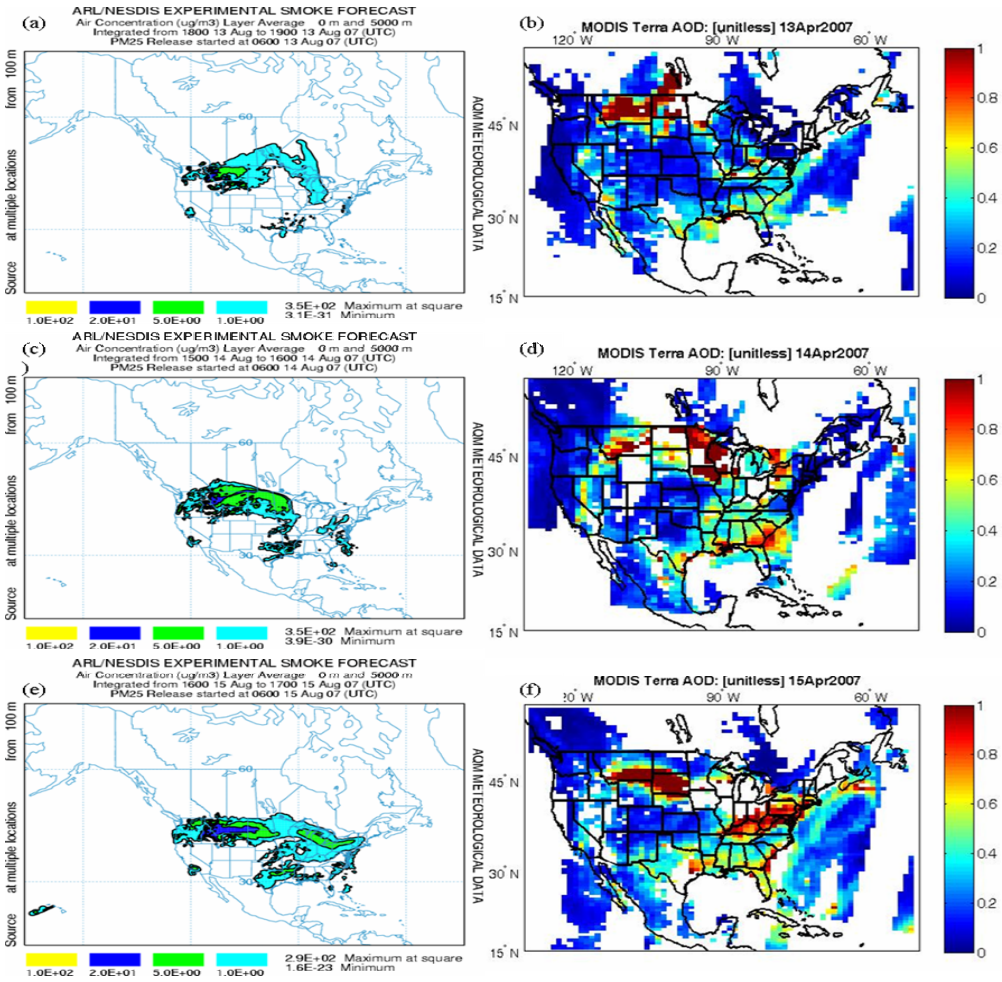

Figure 5.3: MODIS Terra AOD at 550 nm on (b) 13 August, (d) 14 August, and (f) 15 August, 2007. NOAA ARL smoke forecast for (a) 13 August, (c) 14 August, and (e) 15 August, 2007. The smoke forecast are 1-hour average output maps of primary $PM_{2.5}$ air concentrations between that ground and 3 km. Smoke Forecast Model complements of NOAA's Air Resource Laboratory using the HYSPLIT Dispersion Model.

To further identify the nature of the plume coefficient as well as the underlying aerosol environment, we also plot in Figure 5.4 the angstrom coefficient derived from MODIS AOD. The Angstrom exponent α, which is a measure of the wavelength dependence of the of the aerosol extinction, quantifies the slope of the wavelength dependence of the optical depth and is an

indicator of the size of the atmospheric particles. In particular, when the Angstrom exponent is larger than one, the column is dominated by fine mode aerosols, while for Angstrom exponents less than one; the column is dominated by coarse mode aerosols [Kaufman et al. 1993]. In particular, we note that the plume as well as the background aerosol angstrom coefficient is quite high, which is indicative of highly concentrated fine mode aerosols. However, to identify the aerosols as biomass burning, we need to obtain information on the absorbing nature of the aerosols. We utilize the UV aerosol measurements from AURA's OMI sensor, which allows for the determination of the absorbing index (AI) parameter known for its precise identification of biomass burning aerosols. These results are reported in the next sub-section.

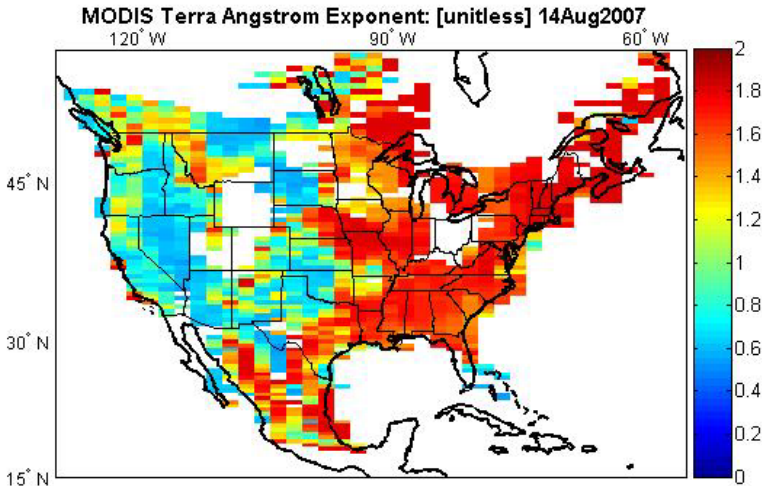

Figure 5.4: Mosaic of Angstrom Exponents over North America derived from MODIS on August 14, 2007.

5.3.3 OMI OBSERVATIONS

As discussed previously, the Aura OMI instrument can differentiate UV-absorbing aerosols such as dust and biomass burning from the weakly absorbing

aerosols and clouds [Braak et al., 2007]. Absorbing and non-absorbing aerosols are separated based on the UV aerosol index, which is positive for absorbing (e.g. dust) and negative for non-absorbing aerosols [Torres et al., 2002]. Details of the OMI retrieval algorithm can be found in appendix A. Since we have already eliminated dust due to the MODIS observed high Angstrom coefficient, a high AI coefficient is a clear indicator of biomass burning. .

In Panel A of Figure 5.5, we see the strong biomass signature of the fire source. By the 14th, the biomass plume had been transported to the northeast. Although the AI index is slightly smaller, the biomass signature is still quite clear. By the 15th, the plumes are observed to be heading out to sea and mixing strongly with native maritime type aerosols reducing the overall absorbing index. The smoke areas in the OMI imagery of UVAI, was found to coincide well with areas where MODIS (Figure 4) reported increased aerosol loading compared to its surrounding background. We observe UV Absorbing Index as high as 4, which is indicative of highly absorbing aerosols.

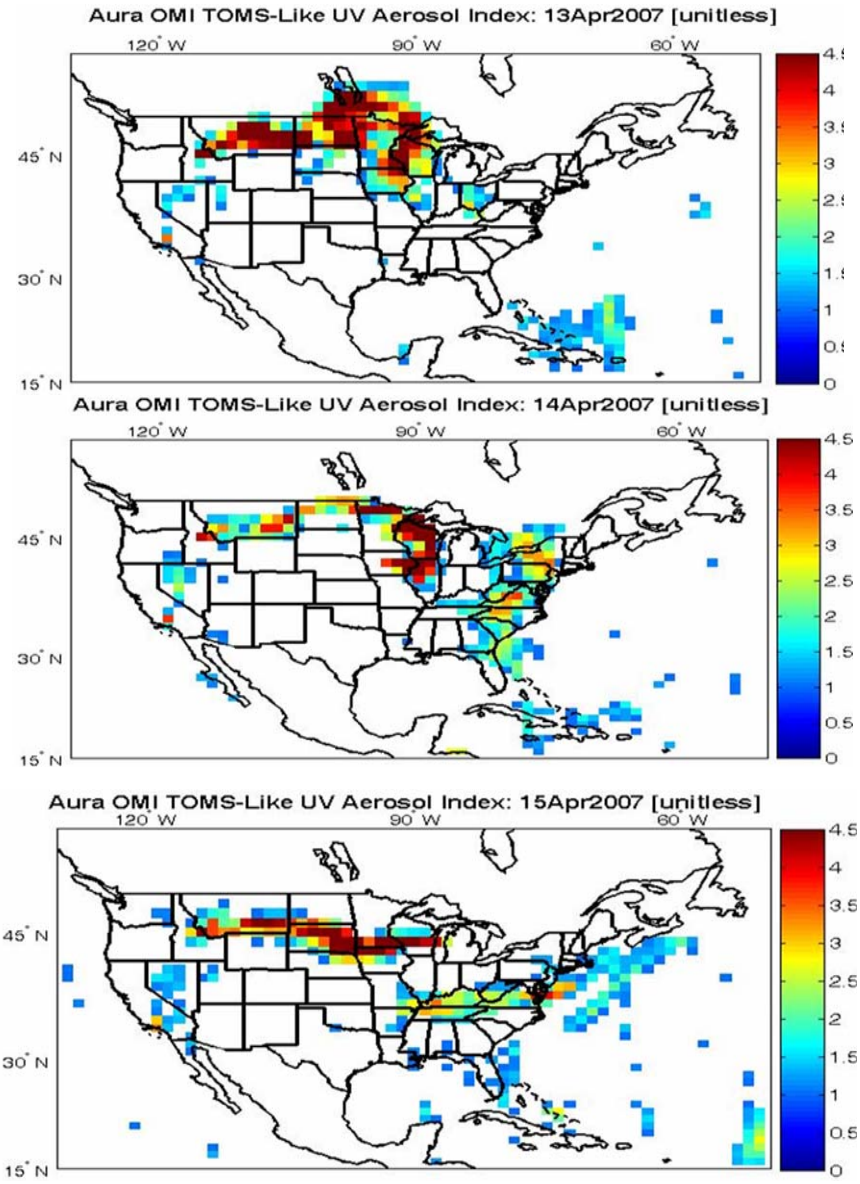

Figure 5.5: TOMS OMI UV Aerosol Index for (a) August 13, 2007, (b) August 14, 2007, (c) August 14, 2006 at 354nm.

5.3.4 MOPITT OBSERVATIONS

We have also examined the biomass nature of the plume directly using the MOPPITT Carbon Monoxide (CO) product which is a good indicator of biomass aerosols and smoke. The results in Figure 5.6 plot the CO concentrations over the NYC area for the plume event as a function of pressure

level. Clear increases in biomass burning is seen on the 14th and 15th of August, marked by the increase in CO concentrations. Note however, that little difference in CO concentration is seen between the 14th and 15th due to the inability of the satellite sensor to see to the PBL layer. In fact, TEOM surface measurements of CO between the 14th and 15th show a 50 percent increase in CO at the surface, which may be indicative of plume advection into the PBL (not shown).

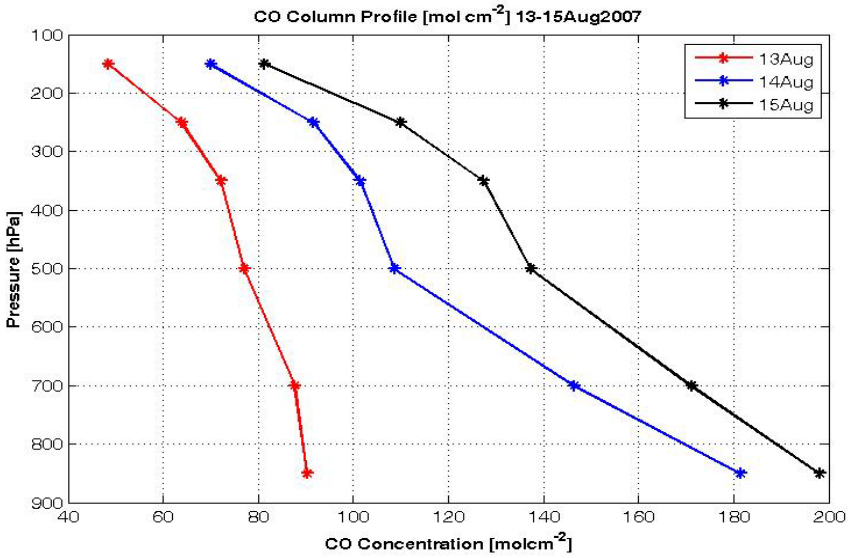

Figure 5.6: MOPITT column profile of carbon monoxide concentration of 13-15 August, 2007 at six pressure levels: 850, 700,500, 350, 250, and 150 hpa.

5.3.5 GOES OBSERVATIONS

Polar orbiting satellite observations are very useful in determining the spatial distribution of aerosols, but are not well suited for examining the time evolution of aerosol plumes for a local domain. However, geostationary measurements provide the possibilities for measuring the time evolution of the aerosol optical depth.

The GOES Aerosol and Smoke product (GASP) provides aerosol optical depth retrievals over the United States at 4 km spatial resolution and 30 minute intervals. Retrievals are performed over land and ocean providing a full view of the Earth daily. The GOES AOD retrieval method uses the visible channel of the GOES-12 Imager data to retrieve aerosol information. The GOES retrieval method is a three-step process. Firstly, a background image composite is created of the visible imagery for each satellite observation time, using the visible image from the past 28 days including the current image. The second minimum reflectance (second darkest pixel) is selected and used in the background composite. Secondly, an atmospheric correction is applied and the Radiative Transfer (RT) model which assumes a continental aerosol model from the Look Up Table (LUT) generated with the 6S RT model, is used to connect the top of the atmosphere (TOA) reflectance to a surface reflectance. In the final step, the calculated surface reflectance, the LUT, and the GOES visible image are used to retrieve the aerosol optical depth at 550 nm [Prados et al., 2007; Knapp et al., 2002, 2005].

As discussed, above due to the requirement that the GASP Product must assume an aerosol type (background continental), it may be thought that the AOD might be quite inaccurate when applied to smoke. However, the GOES visible channel is fairly insensitive to absorbing effects and since the particle size distributions are quite compatible, we might expect fairly good quantitative measures of AOD.

In Figure 5.8 we show a comparison of the AERONET sun-photometer derived AOD and GASP AOD products at CCNY for August 13-15, 2007. The GASP pixel was centered over CCNY and the AOD was averaged over a 0.1^{o} x 0.1^{o} grid for every 30 minutes of data. Although the GASP product uses a single channel, we still see excellent temporal agreement between the GASP AOD and the sun-photometer AOD product when both data sets exist. However, the GASP measurements are often given when the sky radiometer measurements are not available. These gaps in the sun-photometer data exist due to the presence of clouds in the instruments field of view, where an automated cloud screening algorithm has been applied. In the original formulation, the GASP AOD has not been properly cloud screened, and therefore, high optical depth values due to top broken clouds are observed, as indicated by the circled regions in Figure 5.7. However, when applying a more conservative cloud screen technique to the GOES data (courtesy of NOAA/STAR team), most of the cloud pixels were removed while still leaving the plume AOD measurements unaffected.

Two cloud screening techniques were applied to the GOES data, a conservative (filter 1) and a more conservative technique. Filter 1 uses a standard deviation threshold between 0.1 and 0.2, and a cloud free pixel threshold of 15. For the GOES more conservative (filter 2) cloud screening technique, a threshold AOD standard deviation value of 0.15 was used which is obtained by investigating the bias between AERONET and GOES AOD as a function of AOD standard deviation [Kondragunta et al.]. The number of cloud

free pixels threshold was also set to 22. When applied to the data, the screening technique flags out the majority of the cloud pixels.

When we carefully examined the retrievals from the two filters, we see that the more conservative filter (filter 2) removes a greater percentage of the broken cloud measurements but does not reduce the number of plume measurements. We also note that GOES AODs are at times lower than the AERONET AODs and this occurs for relatively small AOD values. We believe that a partial interpretation of this is a possible overestimation of the referenced surface albedo which can occur in summer months, when aerosol loading is often consistently high and a true “clean” atmosphere cannot be seen in a particular three week period. This has dramatic effects on the GASP algorithm. Recall, the GASP surface reflectance is obtained based on assuming a small AOD atmosphere (tau=.02) exists over the second minimum reflectance. If the minimum AOD is larger than the assumed value, the GASP retrieved reflectance will be biased high to match the higher TOA reflectance. In fact, when examining the AOD observed for NYC area over the three week period prior to the plume event, the minimum AOT observed over all time intervals is approximately tau ~ 0.1. The 0.08 excess in AOD not accounted for when calculating the surface albedo leads to an underestimation of AOD on this order and is in good agreement with our match-ups of August 14. This error is expected to be less important as the AOD increases as observed in the Aug 15 match-ups.

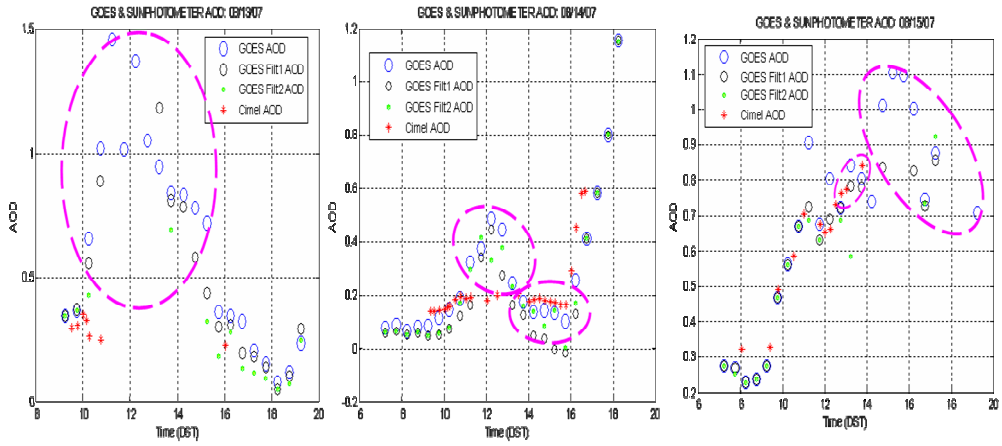

Figure 5.7: MODIS mosaic of aerosol optical depth (AOD) on August 15, 2005

While the nature and spatial extent of the plume event is clearly determined on a large scale, the vertical structure of the plume as well as any impacts the plume may have on local surface air-quality requires complementary ground based instrumentation.

5.4 EVALUATION OF THE PLUME VERTICAL STRUCTURE

As discussed in section 2, an operational multi-wavelength lidar co-located with a CIMEL sun-photometer is available for extensive ground measurements at CCNY. Lidar measurements of the smoke event from Aug 13 to Aug 15 are illustrated in Figure 5.8. On August 13 (Figure 5.8a) we observe prior to the smoke plume arrival over NYC, a clear atmosphere above CCNY with no visible evidence of plumes aloft. On August 14, the vertical profile retrieved by the lidar shows a distinct aerosol layer, identified by its strong aerosol backscatter in the late afternoon at about 7 km altitude (Figure 5.8b). However, by the following day (August 15), as the boundary layer developed and the smoke plumes continued to pollute the free troposphere over CCNY, the most noticeable impact

of the smoke was its downward advection and mixing with the boundary layer by 2:00 PM EST.

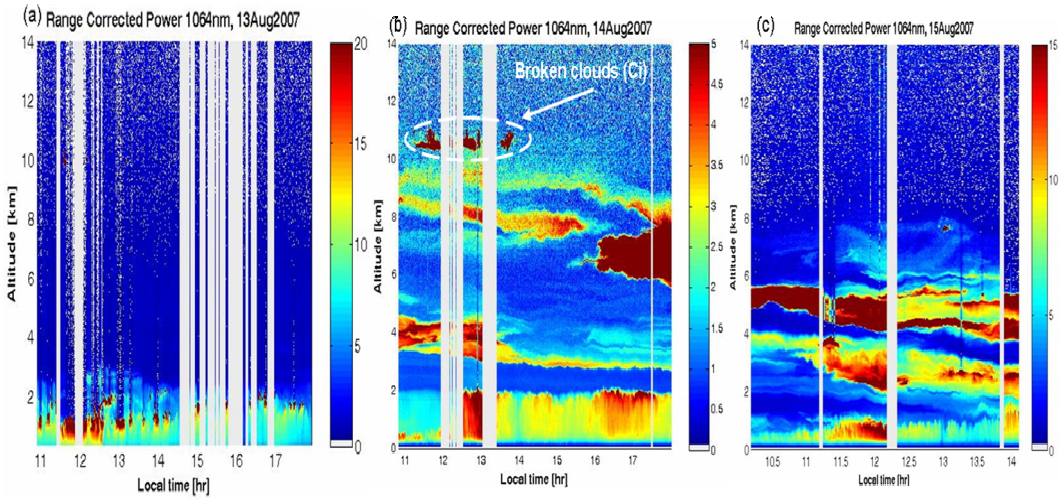

Figure 5.8: CCNY range corrected returns at 1064nm showing high altitude plume formation from Idaho, Montana, and Wyoming fires. a) Aug 13: before evidence of smoke plume arrival to NYC b) Aug 14: onset of plumes with lofted layer and no evidence of PBL interactions c) Aug 15: plumes advect downwards interacting with PBL.

In examining the spatial extent of the vertical plume structure, we also looked at the NASA Micro-Pulse Lidar NETwork (MPLNET) for simultaneous measurement with the CCNY lidar. The MPLNET operates a lidar at GSFC (39^{o} N, 76^{o} W), downwind from the CCNY lidar, which also has a collocated sun-photometer instrument. Figure 5.9 displays the MPLNET/NASA Goddard Space Flight Center Micro Pulse Lidar normalized relative backscatter ratios measured on 14-15 August, the same days as CCNY lidar observations. In the images in Figure 5.9, we can see smoke plumes between 3 and 10 km on August 14 and between 2 and 6km on August 15, similar to that observed over the CCNY site, with the exception that the August 14 plumes over GSFC had already began descent, although no boundary layer mixing was evident. It is also important to highlight that the boundary layer mixing on August 15 occurred about the same

time (14:00 EST) at both locations, which is consistent with the HYSPLIT trajectory analysis.

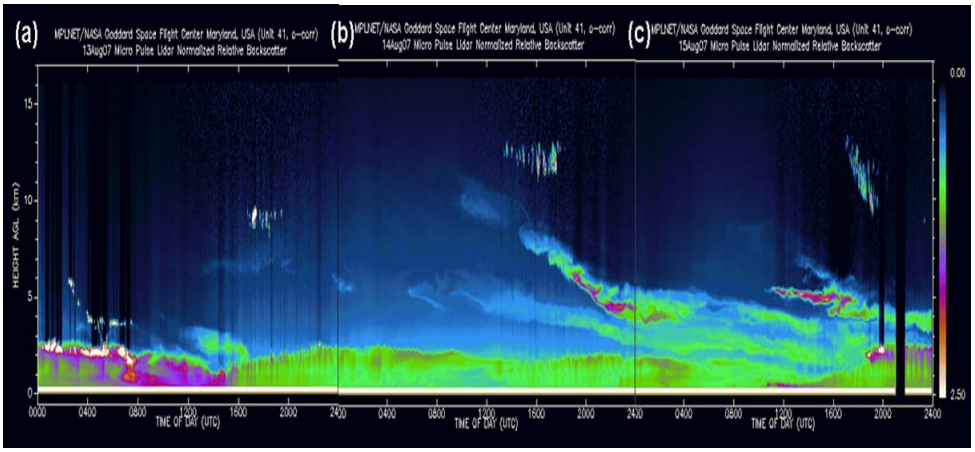

Figure 5.9: MPLNET/NASA Goddard Space Flight Center Micro Pulse Lidar normalized relative backscatter ratios measured on (a) August 13 before the onset of the smoke plumes, (b) August 14, the onset of the smoke plumes descending towards the boundary layer but no visible mixing, and (c) August 15, plume advected downwards and mixed with the surface air.

5.5 PLUME PROPERTIES AND IDENTIFICATION

To test the smoke particulate hypothesis, we have processed our lidar signals at both the 532 nm and 1064 nm channels in order to derive the wavelength dependence of the backscatter within the plume. To obtain the absolute backscatter in the 532 nm channel, we use the traditional Fernald processing scheme [Fernald et al., 1984], where the far end calibration is determined by the molecular profile while the 1064nm channel is calibrated using a cirrus cloud feature within the scene. This approach is similar to that described in Schneider et al (2002), where it is assumed that the cloud backscatter from cirrus clouds between the 532 nm and 1064 nm channels is to a good approximation, a white scatterer independent of wavelength so that the backscatter color ratio is near unity [Kaufman et al., 1997]. In this case, an

accurate measurement of the backscatter below the cloud base at the 532 nm channel can be used to obtain the calibration of the 1064 nm channel. While the main idea is the same, the approach in Schneider et al 2002 is somewhat different technically than our approach and does not discuss the uncertainties inherent in the calibration scheme, due to uncertainties in the 532 nm channel; therefore, we briefly describe it below

I. To begin, a reference height is chosen which is sufficiently clear, based on match-ups with the molecular only signal obtained from meteorological radiosonde data.
II. Given this reference layer, we then “forward” integrate the Fernald equation from the reference layer through the cloud base using a large range of viable parameter values for both the reference aerosol lidar ratio ($Z_{ref}(532) \leq 1.2$) and aerosol S ratio ($30 \leq S_{532} \leq 70$) values.
III. Since it is well known that the forward integration method may become unstable for sufficiently large optical depths, we utilize an iterative scheme for the integration of the Fernald equation, which allows us to ensure stability by calculating the solution at different iteration orders and only penetrating into the cloud when the tenth iteration is the convergent solution.
IV. For all convergent solutions, we then calculate the mean and standard deviation of the backscatter retrieval over all lidar parameter sets, to identify the optimal depth into the cloud that maximizes the backscatter retrieval, while maintaining a sufficiently small retrieval uncertainty.

V. Once the optimal altitude is determined, we can easily obtain the calibration constant as

$$C_{1064} = \frac{\overline{P(z_c)}}{\beta_c(z_c\lambda(532)) + \beta_m(z_c\lambda(1064))T_a^2(R,\lambda(1064))T_m^2(R,\lambda(1064))} \quad (5\text{-}1)$$

Where $\overline{P(z)}$: received backscatter signal (1064 nm) from altitude z.

Once the 1064nm calibration is performed, and the backscatter signal is constructed, the vertical estimate of the plume Angstrom coefficient (α), can be derived using the Angstrom Relation in equation 5-2, where, given the backscatter coefficients at two wavelengths λ_1 and λ_2, where $\lambda_1 < \lambda_2$ are known.

$$\alpha(\lambda_1/\lambda_2) = \frac{-\ln\left[\beta(\lambda_1)/\beta(\lambda_2)\right]}{\ln(\lambda_1/\lambda_2)} \quad (5\text{-}2)$$

To further understand the August smoke plume properties, we also examined the plume angstrom coefficient derived from the lidar backscatter measurements as a function of altitude which we define in Equation 5-2, where β is the aerosol backscatter coefficient, and α is the angstrom exponent. In Figure 5.10c, we can see the large (~ 2) and stable angstrom exponent as a function of altitude, which is a clear indication of small particles. Figure 5.10 b also illustrates the extinction coefficient derived from the lidar measurements. These results are reinforced when the sky radiometer Angstrom coefficient is calculated, as illustrated in Figure 5.11. In particular, we note changes in the angstrom signature (increasing from 1.4 to 1.8 by late afternoon on August 14) indicating

an increase of fine mode particulates entering the air column. Furthermore, the angstrom coefficients remained fairly constant and stable over the entire two day episode, indicating that we are dealing with the same type of particulates (not necessarily coming from a single source). These results are also in good quantitative agreement with the CCNY lidar derived angstrom coefficients.

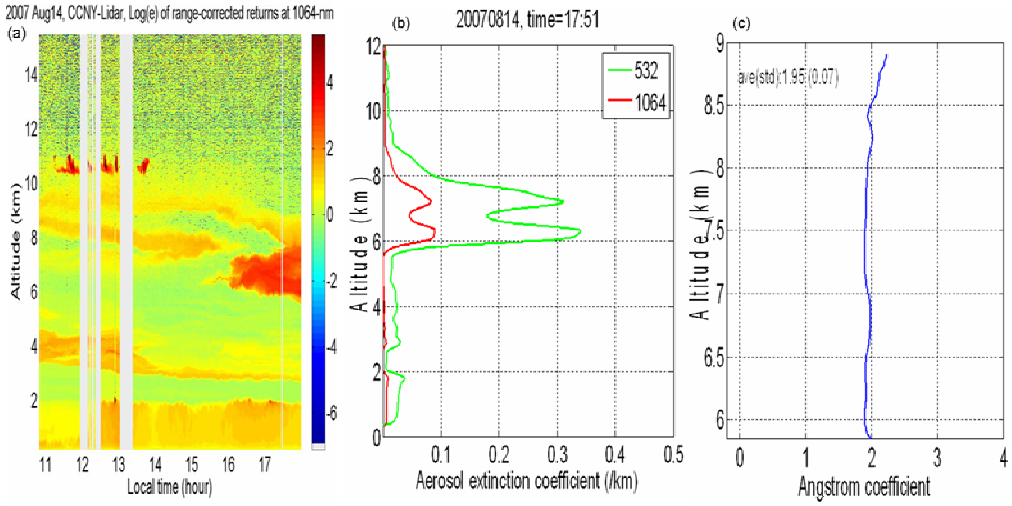

Figure 5.10: a) Lidar range corrected power at 1064nm b) Extinction coefficient obtained from figure 13a at 17:51 EST c) Angstrom coefficient using two wavelengths obtained using equation 2.

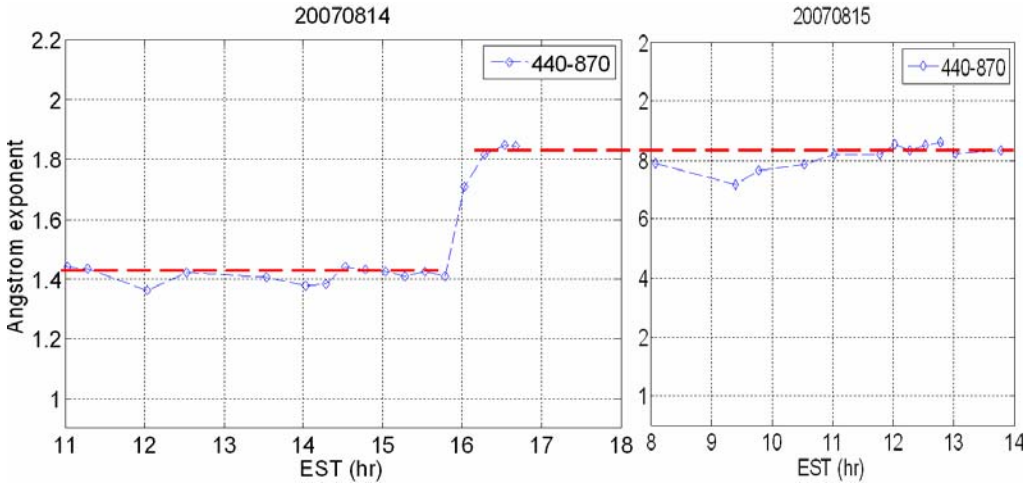

Figure 5.11: Column integrated angstrom coefficient derived from sun photometer AOD measurements using 440 – 870 nm channels.

5.6 SMOKE INFLUENCE ON LOCAL AIR QUALITY

We have already noted the advection of the plume into the PBL, so it is natural to explore any ground signatures that indicates an increase in air pollution in the PBL. Figure 5.12 shows the near surface particulate loadings on August 13-14 obtained from the New York State Department of Environmental Conservation (NYS DEC). On August 14, as expected, the $PM_{2.5}$ loadings were low and in good agreement with lidar measurements of PBL AOD described in section 5.7. These observations showed no evidence of boundary layer interaction with upper tropospheric plumes, and at the surface scattering coefficients and particulate loadings remained low, which is a characteristic of clear and relatively unpolluted air above the boundary layer. On the other hand, by the afternoon of August 15, there was a large-scale descent of smoke plumes (figure 5.12), resulting in a significant increase in the surface $PM_{2.5}$ loadings, compared to the states prior to plume interaction.

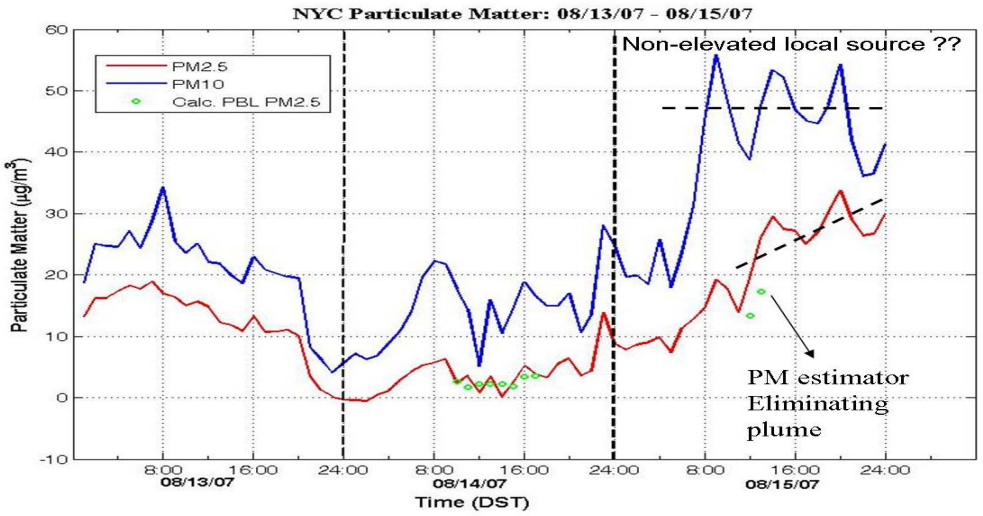

Figure 5.12: Ground level PM2.5 and PM10 surface loadings for New York City on August 13-14, 2007.

5.7 LIDAR DERIVED AOD APPORTIONMENT

Many attempts have been made to connect surface PM2.5 measurements to column AOD, but these efforts are very inaccurate when aloft plumes are present. To obtain such a connection requires that we separate the column AOD into a plume and a PBL component. This decomposition clearly requires the use of Lidar data which can provide accurate vertical extinction profiles and therefore provide an accurate measure of the plume extinction. Measurement of the PBL optical depth is more difficult, since a non-overlap zone of 500 meters exists in our lidar measurements. Therefore, we simply assume that the extinction in the final 500 meters is constant and equal to the mean value of the extinction between 500 and 600 meters. Figures 5.13 (a) and (c) show the lidar column integrated AOD (green) and AOD apportionment above the PBL (blue) for August 14 and 15. We can also see that lidar derived column optical depth is in good agreement with the sun-photometer AOD on both days.

Once we correctly extract the PBL AOD, we can explore and validate the connection between AOD and PM2.5. An often used approach which is currently being used in the Infusing satellite Data into Environmental Applications (IDEA) product for the northeastern US is to equate the 1 AOD to ~ 60 μgm^{-3} $PM_{2.5}$ assumptions. To verify the validity of this estimator performance, we applied the estimator directly to the AOD loadings derived from the CCNY lidar below the PBL and compared it to the $PM_{2.5}$ concentrations as measured by the Tapered Element Oscillating Microbalance (TEOM). Figure 5.14 shows the hourly PM2.5 concentrations (measured) and the lidar $PM_{2.5}$ concentrations (estimated) within the boundary layer is in reasonably good agreement on August 14, indicating

acceptable $PM_{2.5}$ estimator performance, while showing how critical it is to remove the PBL AOD contribution from the total column.

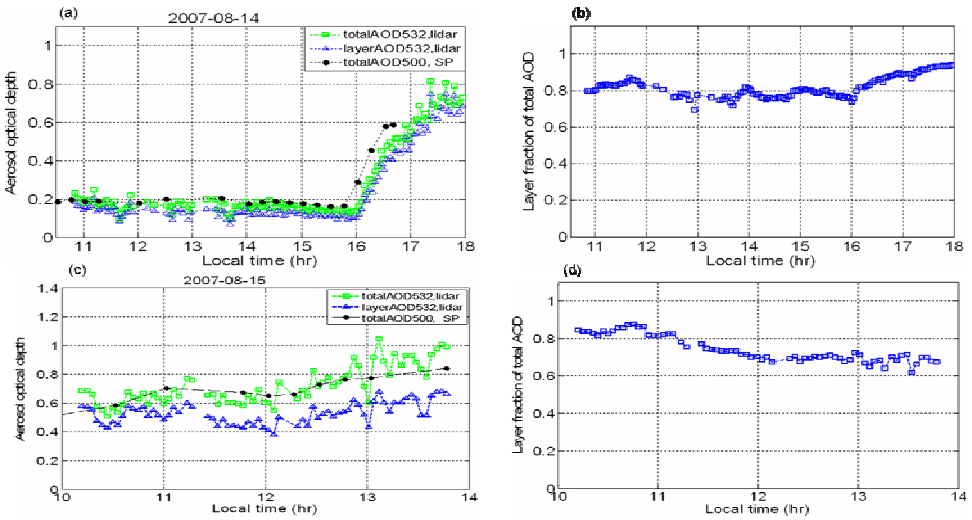

Figure 5.13: a) Lidar total column AOD (green), AOD apportionment above the PBL (blue), and sun-photometer column AOD on August 14; b) Lidar fraction of total column AOD due to plume layers above the PBL on August 14; c) Lidar total column AOD (green), AOD apportionment above the PBL (blue), and sun-photometer column AOD on August 15; d) Lidar fraction of total column AOD due to plume layers above the PBL on August 15.

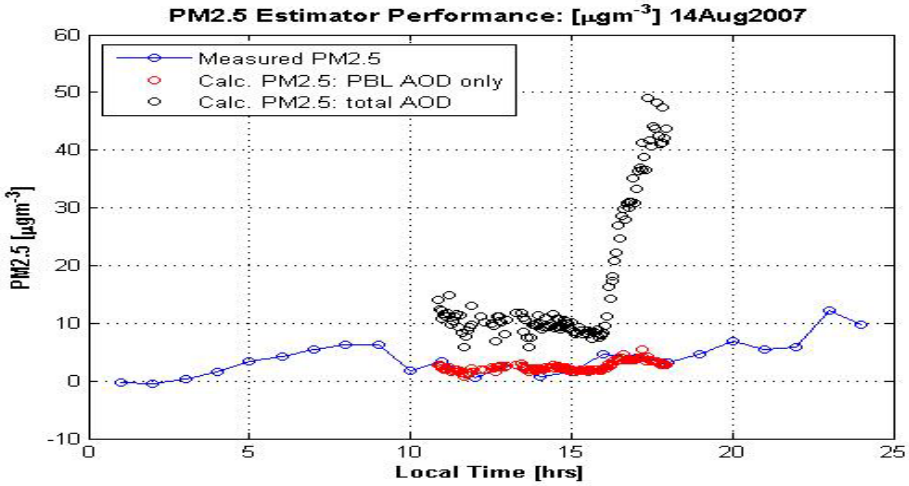

Fig. 5.14: Lidar column AOD (blue), Layer column AOD (red), and sun-photometer column AOD (black) April 18, 2006

5.8 SUMMARY

Satellite measurements can be a valuable tool for estimating air quality, providing information not available from traditional ground monitoring stations. If measured accurately, satellite data can help in the quantitative and qualitative detection, tracking, and understanding of pollutant transport by providing observations over extended spatial domains. Satellites can be the only data source in rural and remote areas where no ground-based measurements are taken and can help assess the impact of events such as biomass burning or dust transport from remote sources.

The limited air pollution monitoring from conventional methods restrict our ability to enforce global air quality regulations, therefore a fusion of satellite and ground measurements is necessary to generate a detailed estimate of air pollution. We emphasized this by showing good correlations between the GASP, sun-photometer, and lidar total column AOD products.

Our analysis of the transport of the Idaho and Montana forest fire plumes over the eastern United States during August 2007, demonstrates the importance of pollution monitoring and prediction particularly in situations when lofted layers are mixed with surface air by coupling to the PBL and can have significant implications on human activities. Lidar provide the means to quantitatively evaluate the spatial and temporal variability of smoke plumes. The elevated smoke plume subsequently mixed to the surface as it was entrained into the turbulent planetary boundary layer and can have adverse effects on the surface air quality over the region, which was quantified by the enhanced $PM_{2.5}$ loadings.

We also showed that the time variability of $PM_{2.5}$ and PM_{10} loadings are consistent with our interpretation of a plume advecting into the planetary boundary layer, thereby altering the surface air quality. We also demonstrated to a certain extent, that the static relationship between PM2.5 and AOD can be satisfied to a reasonable accuracy if we correctly apportion the PBL AOD contributions from the total column AOD. This is at times very difficult since the static relationship between PM2.5 measurements and AOD can vary regionally since the sources and compositions of aerosols also vary regionally.

Trajectory analysis confirmed the origin of the smoke to be Idaho and Montana, its transport at high altitudes, and deposition ofpollutants to the surface. Additionally, the smoke optical properties obtained from the CCNY multi-wavelength lidar was in good agreement with radiometer and remote sensing observations (sun-photometer and GASP). These results have important implications for the long-range transport of pollutants and their subsequent entrainment to the surface, as well as the evolving optical properties of smoke from forest fires.

ACKNOWLEGEMENTS

The NASA Micro-Pulse Lidar Network is funded by the NASA Earth Observing System and Radiation Sciences Program. We thank the MPLNET PI(s) (Dr. Judd Welton, Dr. James Spinhirne, Mr. Brent Holben, and Dr. Si-Chee Tsay) and MPLNET staff (James Campbell, Sebastian Stewart, Larry Belcher, and Dave Augustine) for their efforts in establishing and maintaining the (Goddard Space Flight Center (GSFC)) site.

REFERENCES

Angstrom, A., "On the atmospheric transmission of sun radiation and on dust in the air", Geogr. Ann., 11, 156–166, 1929.

ARL HQ Modeling Group, "HYSPLIT Interim Smoke Forecast Tool".

Braak, R., O. Torres, B. Veihelmann, J. P. Veefkin, M. Kroon, and P. Levelt, "OMI UV absorbing index as a tracer for transport of Australian biomas burning aerosols", Geophys. Res. Letterss, 9, 2007.

Herman., J. R, P. K. Bhartia, O. Torres, C. Hsu, C. Seftor, and E. Celarier, "Global distribution of UV absorbing aerosols from Nimbus 7/TOMS data", J. Geophys. Res. **102**, 16,911-16,922, 1997.

Kaufman, Y. J., "Aerosol optical thickness and atmospheric path radiance", J. Geophys. Res., 98(D2), 2677–2692, 1993.

Kaufman, Y. J., D. Tanré, L. Remer, E. Vermote, A. Chu, and B. N. Holben, "Remote sensing of tropospheric aerosol from EOS-MODIS over the land using dark targets and dynamic aerosol models", J. Geophys. Res., VOL. 102, 17051-17067, 1997.

Knapp, Kenneth R., "Quantification of aerosol signal in GOES 8 visible imagery over the United States", J. Geophys. Res., VOL. 107, NO. D20, 2002.

Knapp, Kenneth R. and Thomas H. Vonder Haar, "Aerosol Optical Depth Retrieval from GOES-8: Uncertainty study and Retrieval validation over South America", J. Geophys. Res., VOL. 107, NO. D7, 2002.

Knapp, Kenneth R., R. Frouin, S. Kondragunta, and A. Prados, "Towards Aerosol Optical Depth Retrievals over land from GOES visible radiances: determine surface reflectance", International Journal of Remote Sensing, VOL. 26, NO. 18, 2005.

Kondragunta, S., P. Ciren, A. I. Prados, Y. Shinozuka, A. Clark, "Characterization of GOES-12 Aerosol Optical Depth Retrievals during ICARTT/INTEX-A", J. Geophys. Res.

Prados, Ana I., Shobha Kondragunta, Puba Ciren, and Kenneth R. Knapp, "GOES Aerosol/Smoke Product (GASP) over North America: Comparisons to AERONET and MODIS observations", J. Geophys. Res. 112, 2007.

Torres, O, P. K. Bhartia, J. R. Herman, Z. Ahmad, and J. Gleason, "Derivation of aerosol properties from satellite measurements of backscattered ultraviolet radiation: Theoretical basis". J. Geophys. Res. **103**, 17,099-17,110, 1998.

Torres, O., R. Decae, P. Veefkind, G. de Leeuw, "OMI Aerosol Retrieval Algorithm", OMI Algorithm Theoretical Basis Document, Volume III, Version 2, August 2002.

6 DUST TRANSPORT

Regional Impact of Inter-Continental Dust Transport

6.1 INTRODUCTION

Aerosols transported over long distances can affect air quality on a local, regional, and even intercontinental scale. Therefore, global monitoring of aerosols is important, not only because of aerosol effects on the Earth radiation budget, but also because of the potential impacts on air quality and human health, cloud properties, and precipitation. Airborne particulate matter (PM) is one of the principal components of the atmosphere that has been singled out as a major air pollutant concern [Szykman et al.; 2004]. Surface air pollution caused by such particulates has been a major problem since the beginning of the industrial revolution, both because of its impact on human respiratory and pulmonary system as well as on visibility (because of their ability to scatter light).

Long-range transport and mixing of aerosols with surface air can increase particulate concentrations and may consequently reduce the benefits of local emission control [Chin et al.; 2007]. Chin et al. [2007] studied the implications on air quality by intercontinental transport of pollution and dust aerosol. Their results revealed that long-range transport of dust adds significant amounts of fine particulates (>0.5μgm-3 annual average) over the eastern US [Henald et al.; 2006]. Collette et al. [2006] studied the transpacific transport of Asian anthropogenic aerosols and its impact on surface air quality in the United States.

It has been documented by many authors that east Asian dust can be transported over the northern Pacific reaching Canada and the United States. A comprehensive evaluation of the April 1998 dust storm was done by Husar et al. (2001) by using a combination of satellite multi-sensor observations (AVHRR aerosol optical depth, TOMS aerosol index, etc.), and ground based observations, including AERONET sun-photometer measurements. Recently, Darmenova et al., (2005) examined the capabilities of TOMS, MODIS, and SeaWiFS measurements to track dust plumes and constraining the areas affected by dust transport over land and ocean.

Of particular interest in this section is the application of multi-wavelenght lidar together with the Ozone Monitoring Instrument (OMI) aboard NASA's Aura Satellite to study intercontinental dust transport and its regional impact on air quality. In particular, our ground-based lidar measurements are used to determine the plume angstrom exponent, which, together with OMI UV absorbing aerosol index allows us to differentiate a plume as a dust event. We also observe the dynamic mixing of high altitude plumes with the PBL, resulting in a dramatic rise in surface PM_{10} concentrations without a corresponding dramatic rise in $PM_{2.5}$ concentrations. These observations strongly suggest the deposition of large particulates into the PBL, which is consistent with both lidar angstrom coefficient measurements and back-trajectory analysis.

Lidar provides a method to quantitatively evaluate the spatial and temporal variability of smoke and dust plumes as they are transported downwind from their sources at a single convenient location and has the ability to detect the complex vertical structure of the atmosphere and can therefore identify the existence and

extent of aerosols that have undergone long-range transport. Husar et al. [2001] performed a detailed analysis on an East Asian dust episode of April 1998 using data from multiple satellites, including AERONET sun photometer and TOMS aerosol index. Here, we follow the Asian dust episode of April 6-21, 2006, which traversed the Pacific reaching Canada and the Eastern United States by 18, April 2006. The focus is on qualifying and quantifying the use of lidar techniques, multi-sensor satellite observations, and other ground based measurements to provide useful evaluations of the dust event.

6.2 MOTIVATIONS FOR AEROSOL MONITORING AND ASSESMENTS

Air quality in New York City and elsewhere is highly dependent on the meteorological conditions that govern the transport and mixing of trace gases and aerosol particles. These processes occur on a variety of scales, namely; the atmospheric boundary layer (ABL), regional, intra-continental and inter-continental scales. Previous studies have demonstrated on all of these scales, the impact of transport processes on the United States, in particular the impact on surface air quality [Chin et al., 2007; Thulasiraman et al., 2002; Jaffe et al., 2003; Heald et al., 2006; and VanCuren et al., 2002]. A clear understanding of transport on these scales will allow us to assess the impact from local, regional, and distant sources on air quality of air masses as they traverse over NYC and are transported to downwind locations. The event discussed in this section was observed by continuous multi-sensor satellite observations, lidars, sun

photometer measurements, and surface aerosol monitors on the east coast, NYC in particular.

6.3 APRIL 2006 EAST ASIAN DUST EVENT

Lidar has the capability to characterize particle optical properties on both a horizontal and vertical scale, which makes it an applicable tool for boundary layer aerosol properties. Lidar also serves as a means to quantify the effects of the boundary layer structure and dynamics on plume incursion and dispersion. Its AOD retrievals also serve as a proxy indicator of PM2.5 concentrations, making it a key parameter for various aerosol related studies [Kaufman et al., 1997]. To assess the need for lidar measurements to predict PM2.5, we examine a case of a plume advecting and mixing with the planetary boundary layer.

The large-scale event of free tropospheric transport of dust particles that occurred in April of 2006 provided an excellent opportunity to gain new insight on the influence of such lofted plume layers. In support of this prediction, the CCNY lidar system observed some reasonable transport activity over its location, which contributed to reasonable aerosol loadings in the free troposphere.

6.4 Model Predictions and Satellite Observations

6.4.1 Model Predictions

Transport models can be very useful forecasting tools for predicting inter-continental aerosol transport. The Infusing Satellite Data into Environmental Applications (IDEA) 48-hour aerosol trajectory forecast which plots the latest high MODIS aerosol optical depth (AOD) and the potential vertical movement of high

aerosol loads in the troposphere, reported very low aerosol optical depth (τ_a<0.2) over New York City (NYC) and its immediate vicinity. These low AOD's are indicative of low column aerosol loadings, nonetheless; the parcel trajectory forecast patterns were in agreement with the HYSPLIT back-trajectory models displayed in Figure 6.1. However, in the trajectory forecast areas of elevated MODIS AOD (τ_a>0.4) are seen over parts of southeastern Canada (north of US east coast) on April 18 and 19; projecting wind patterns towards the eastern US with particle trajectories directed towards high pressure within the boundary layer on April 19. The backward trajectories also show that the dust observed at all levels above the planetary boundary layer on April 19 (Figure 6.1a) and April 18 (Figure 6.1b) originated from East Asia. This shows that transport source can be predicted to some degree of accuracy. This evidence for long-range transport of continental aerosols prompted our examination of satellite imagery for pre-lidar observation days.

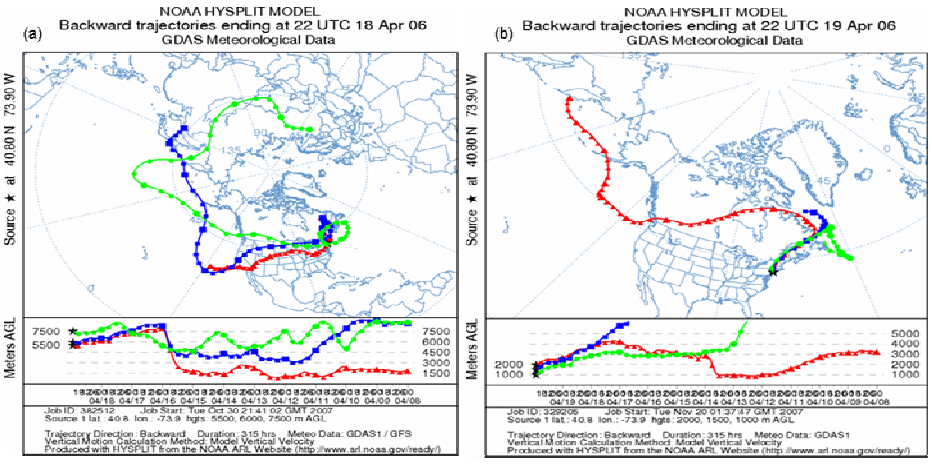

Figure 6.1: NOAA/ARL 13-day HYSPLIT model backward particle trajectories for three altitudes (indicated) ending at 2200 UTC on April 18 and 19, 2006 respectively showing source for continental layers from East.

6.4.2 Satellite Observations

It is well documented that aerosol plumes can at times be transported over large distances from their source regions, and can also affect the air quality of the Earth's climate system. Therefore, monitoring of their constituents on a global scale is necessary. Although ground based remote sensing provides accurate aerosol information at high temporal resolution, their spatial coverage is limited which impacts our ability to monitor aerosol concentrations and their properties across the United States. Surface monitoring is limited over the United States, particularly over costal regions which are very often niche by polluted air approaching over water. Long-range plume layers can also be transported aloft, undetected by ground monitors, and can also descend to influence surface air.

6.4.2.1 MODIS OBSERVATIONS

Dust plumes are readily seen in satellite imagery, and many satellite sensors like GOES, MODIS [Kaufman et al., 1997] and TOMS [Torres et al., 1998 and Herman et al., 1999] have been widely used to map the geographical distribution and to characterize aerosol (dust) transport on a global scale. MODIS and TOMS (sun synchronous polar orbiting satellites) provide global coverage approximately once a day and can only provide snap-shots of large-scale aerosol spatial distribution during the time of satellite overpass, which is impractical for daily tracking and monitoring of large scale aerosol events.

The 8-day mean aerosol optical depth retrieved from MODIS (Level-3 global product) was used in this analysis, which is derived from Level-2 data and spatially averaged to a 1^o x 1^o equal angle grid over 24 hours. To better illustrate the MODIS spatial coverage and spatially assess the dust transport event, a fusion of eight days of data becomes useful to obtain a cloudless composite image. In Figure 6.2, we show an 8-day MODIS composite image (16-23 April, 2006) indicating how well this event was captured from its source region (east Asia) and its transport across the northern pacific to Canada and the United States. We can observe that the Asian dust was transported along the extent of the U.S. eastern seaboard. Although it was a large scale dust event which spanned over 13 days, by the time the dust particulates reached the eastern U.S. the plume had weakened. This is shown by the low aerosol loadings ($\tau < 0.2$). It is also very likely that the dust particulate concentrations may have been reduced by precipitation scavenging along its transport path, although HYSPLIT model shows no precipitation except for April 14 (< 1 inch). We can also see in Figure 6.2 that the largest enhancements in aerosol optical depth is over the source region and its immediate surroundings and of a lower order along its trajectory path compared to the much lower aerosol loadings in the background.

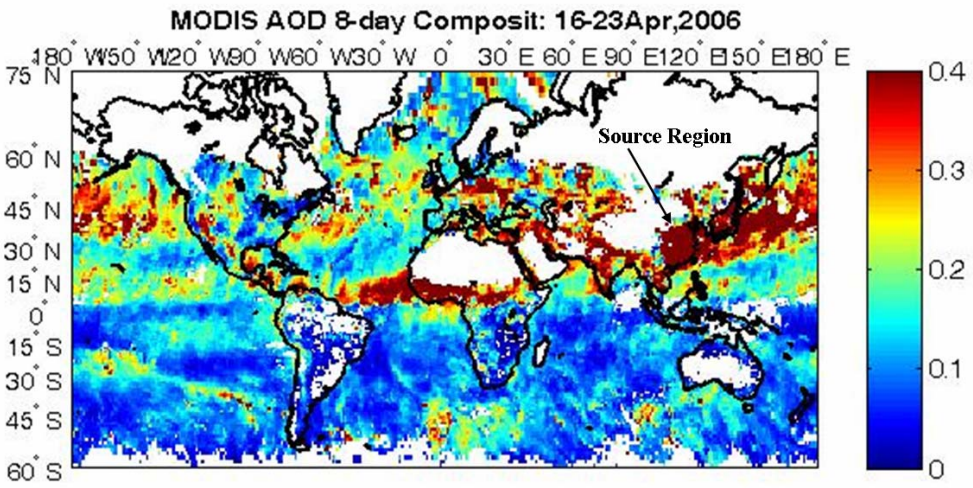

Figure 6.2: Dust pollution from source region and transport pathway from MODIS AOD (550nm) image (8-day composite level-3 product) in 16-23 April, 2006.

6.4.2.2 OMI OBSERVATIONS

The Aura Ozone Mapping Instrument (OMI) provides daily information on absorbing aerosols using a retrieved aerosol index (AI) [Torres et al., 2002] and is continuously being used to track long-range transport events globally. However, because its sensitivity to aerosols decreases with increasing pressure (lowest near surface), this limits its use for air quality monitoring is limited. The main mission of the Aura OMI instrument is to monitor atmospheric aerosols and smoke from biomass burning; in particular, differentiating UV-absorbing aerosols such as dust and biomass burning aerosols from the weakly absorbing aerosols and clouds [Braak et al., 2007]. Absorbing and non-absorbing aerosols are separated based on the UV aerosol index, which is positive for absorbing (e.g. dust) and negative for non-absorbing aerosols [Torres et al., 2002]. OMI also has the unique capability to detect aerosols mixed with clouds. The aerosol index is simply a measure of the absorption of UV radiation by aerosols.

As was done with the MODIS AOD data, we used the OMI TOMS-Like daily global 1^{o}x1.25^{o} UV aerosol index (dust only) for 12-20 April of the dust event and computed an 8-day global composite of UV Aerosol Index with the goal of being able to fill in the gaps of missing meaningful data. Figure 6.3 shows the results of the 8-day UVAI composite, with the HYSPLIT trajectory projected on the map. We can see that the air parcel trajectory clearly follows the transport path of the dust plume which was observed by the CCNY lidar system, particularly over northern Canada, because OMI has the capability over other satellite sensors of detecting aerosols mixed with clouds.

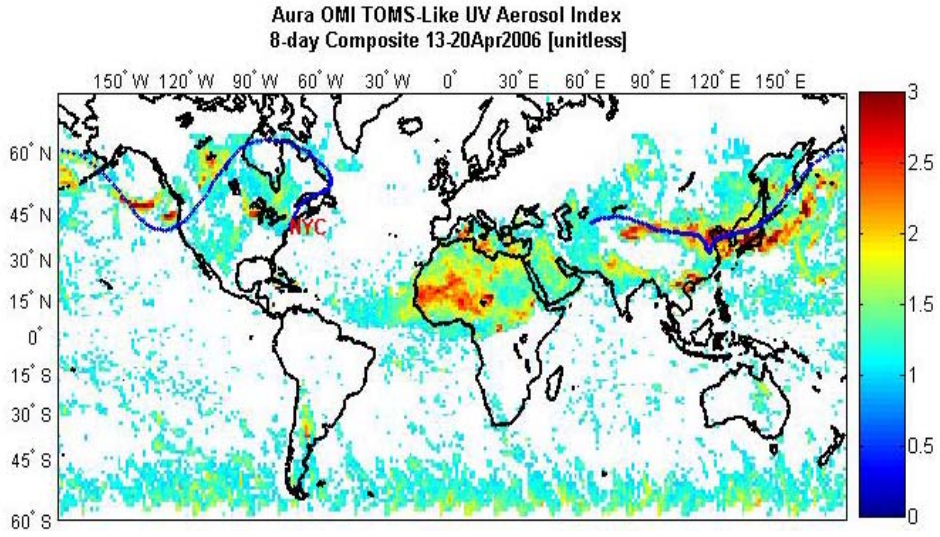

Figure 6.3: Aura OMI Toms-Like Global 1^{o}x1.25^{o} UV 8-day composite Aerosol Index over 12-20 April, 2006.

6.5 CCNY MULTI-WAVELENGTH LIDAR OBSERVATIONS

During 6-21 April, 2006, a severe dust storm wiped over East Asia, where waves of dust washed out of the Asian deserts and progressed over the northern Pacific Ocean reaching Canada and eastern Unites States, and arriving NYC by

April 19. Figure 6.4 and 6.5 shows the measured lidar signal (range corrected) on April 18 at 1064 nm and April 19 at 532, 355, and 1064 nm respectively, measured by the CCNY lidar system. The figures illustrate the complex vertical structure of the observed atmosphere over CCNY.

These observed features are consistent with the upper air meteorological soundings displayed in Figure 6.6, which was obtained using the NOAA Air Resources Laboratory HYSPLIT model. Although the retrieved backscatter was reasonably small on both days, aerosols have been detected up to altitudes of 10,000 m on April 18 and 6000 m on April 19 above CCNY, with the majority of the optical depth attributed to the lofted plumes. In addition, we observe a well-mixed (homogeneous) PBL in the CCNY Lidar image, except for the midday haze on April 18, indicating a shallow PBL (~ 1 km) in the morning with a gradual increase to about 2 km during the afternoon, allowing for an interaction between the PBL and the lofted plume. Upper air soundings provide a means to confirm the detailed vertical structure of the atmosphere as observed by the CCNY Lidar system. The PBL is topped by a temperature inversion, which can be seen in the upper air soundings in Figure 6.6.

The lidar also reveals how multiple clean and continental influenced aerosol layers can coexist over a particular location, and how variable the column physical, chemical, and optical properties can be. In Figure 6.4, the aerosol layers appear to be entrained between 5 and 10 km, with no evidence of decent. However, in Figure 6.5, during most of the day the aerosols were concentrated in layers above 3km and by 4:00PM demonstrated to be entrained into the

planetary boundary layer from aloft. The incursion of the transported aerosol plume into the boundary layer was clearly a cause for air quality concerns.

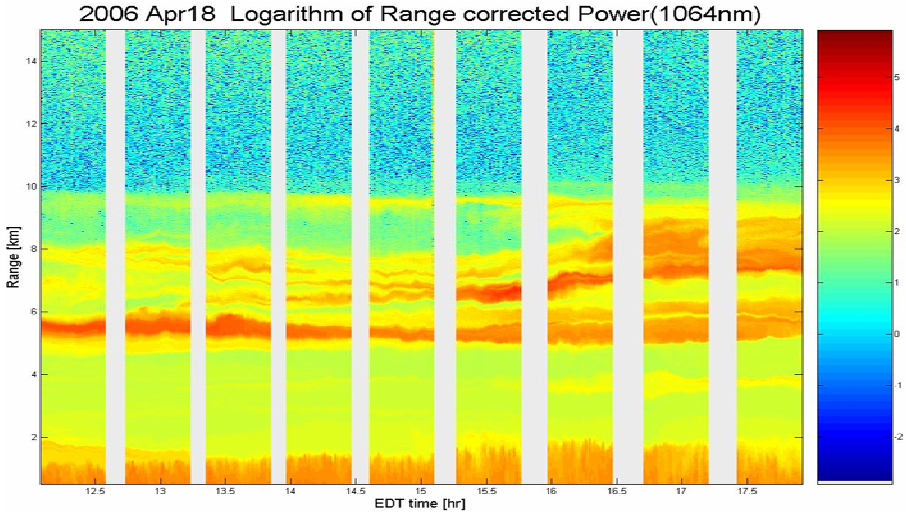

Figure 6.4: Time-to-height indication of range-corrected power (logarithmic) obtained by the CCNY lidar on April 18, 2006 at 1064nm.

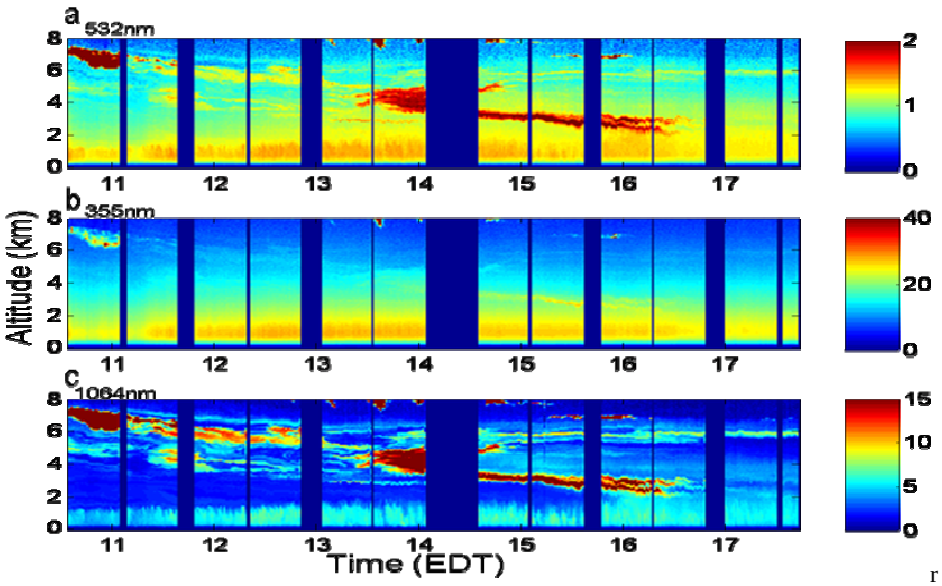

Figure 6.5: Time-to-height indication of range-corrected power obtained by the CCNY lidar on April 19, 2006. (a) Visible at 532 nm, (b) UV at 355 nm, and (c) IR at 1064 nm

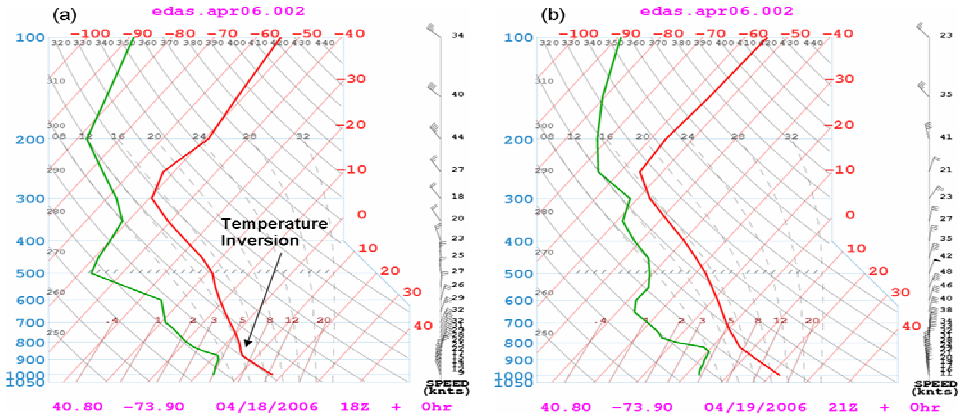

Figure 6.6: Upper air sounding for (a) 1800 UTC on April 18, 2006 and (b) 2100 UTC on April 19, 2006 obtained from HYSPLIT model.

6.6 PLUME PROPERTIES AND IDENTIFICATION

6.6.1 PLUME PROPERTIES FROM GROUND OBSERVATIONS

Figure 6.7 shows the near surface particulate loadings on April 19 obtained from the New York State Department of Environmental Conservation (NYS DEC). April 18 showed low PM2.5 loading within the CCNY lidar observation window (not shown), which is expected since the plumes remained aloft, and also indicating the absence of local transport. On the other hand, since a plume incursion into the PBL was evident on April 19, it was practical to examine the influence of these incursions on near surface air quality. $PM_{2.5}$ levels showed a very small increase in mass loads but as seen in Figure 6.7, the small $PM_{2.5}$ loading occurred simultaneously with a distinctively large increase in the PM_{10} loadings during the incursion period, which is identifiable with the PBL. This finding is consistent with the hypothesis that the plume is comprised mainly of large dust particulates undergoing large-scale transport from a remote source. Additionally, we have analyzed coincident data obtained from the CCNY mobile

lidar stationed at Princeton University in New Jersey. This lidar is downwind from New York City, and captured the same transport event seen over NYC at a later time.

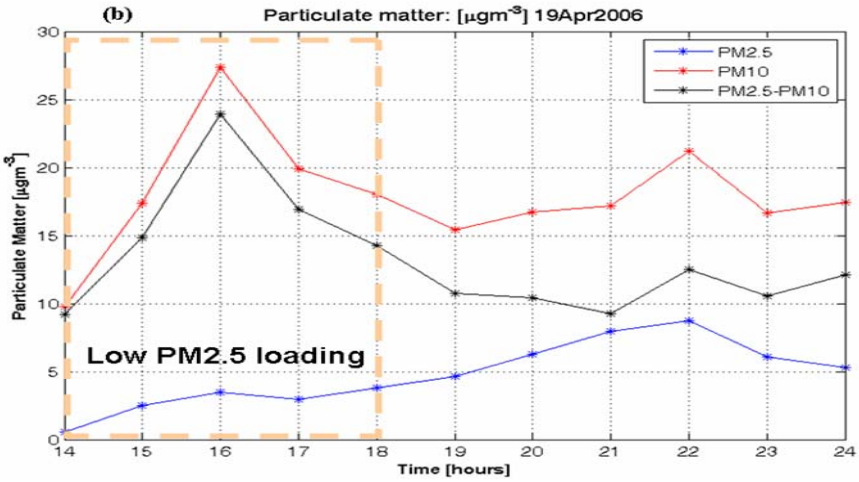

Figure 6.7 Ground level PM2.5 surface loadings for New York City, April 18, 2006.

To test the dust particulate hypothesis, we have processed our lidar signals at both the 532 nm and 1064 nm channels in order to derive the wavelength dependence of the backscatter within the plume. To obtain the absolute backscatter on the 532 nm channel, we use the traditional Fernald processing scheme [Fernald et al., 1984], where the far end calibration is determined by the molecular profile while the 1064 nm channel is calibrated using a cirrus cloud feature within the scene. This approach is similar to that described in Schneider et al 2002, where it is assumed that the cloud backscatter from cirrus clouds between the 532 nm and 1064 nm channels is to a good approximation, a white scatterer independent of wavelength so that the backscatter color ratio is near unity [Kaufman et al., 1997]. In this case, an accurate measurement of the backscatter below the cloud base at the 532 nm

channel can be used to obtain the calibration of the 1064 nm channel. While the main idea is the same, the approach in Schneider et al 2002 is somewhat different from our approach, it does not discuss the uncertainties inherent in the calibration scheme, due to uncertainties in the 532nm channel. We briefly describe our approach below:

I. To begin, a reference height is chosen which is sufficiently clear, based on match-ups with the molecular only signal obtained from meteorological radiosonde data.

II. Given this reference layer, we then "forward" integrate the Fernald equation from the reference layer through the cloud base using a large range of viable parameter values for both the reference aerosol lidar ratio ($Z_{ref}(532) \leq 1.2$) and aerosol S ratio ($30 \leq S_{532} \leq 70$) values.

III. Since it is well known that the forward integration method may become unstable for sufficiently large optical depths, we utilize an iterative scheme for the integration of the Frenauld equation, which allows us to ensure stability by calculating the solution at different iteration orders and only penetrating into the cloud when the 10^{th} iterate is the convergent solution.

IV. For all convergent solutions, we then calculate the mean and standard deviation of the backscatter retrieval over all lidar parameter sets, to identify the optimal depth into the cloud that maximizes the backscatter retrieval, while maintaining a sufficiently small retrieval uncertainty.

V. Once the optimal altitude is determined, we can easily obtain the calibration constant as

$$C_{1064} = \frac{\overline{P(z_c)}}{\beta_c(z_c\lambda(532)) + \beta_m(z_c\lambda(1064))T_a^2(R,\lambda(1064))T_m^2(R,\lambda(1064))} \quad (6\text{-}1)$$

Where $\overline{P(z)}$: received backscatter signal (1064) from altitude z.

Once the 1064nm calibration is performed, and the backscatter signal is constructed, the vertical estimate of the plume Angstrom coefficient (α), can be derived using the Angstrom Relation in equation 6-2, where, given the backscatter coefficients at two wavelengths λ_1 and λ_2, where $\lambda_1 < \lambda_2$ are known.

$$\alpha(\lambda_1/\lambda_2) = \frac{-\ln[\beta(\lambda_1)/\beta(\lambda_2)]}{\ln(\lambda_1/\lambda_2)} \quad (6\text{-}2)$$

The dust event can easily be distinguished from its background conditions by examining the angstrom exponent as a function of backscatter. During those days the angstrom exponent was approximately 0.5, with minimum values near zero on April 19 when the dust mixed with the boundary layer. We show the lidar aerosol extinction for April 18 and 19, which is a product of the aerosol backscatter and lidar scattering ratio. For the dust, our S ratios were based on the dust aerosol model from AERONET. Then using the 532-1064 nm wavelengths we derived the plume angstrom exponent. Figure 6.8, shows the aerosol backscatter and angstrom exponent as a function of altitude for the 15:20 EST time slice on April 18. We can observe that for the plume layers between 5-8 km (Figure 6.8a), the plume backscatter coefficient is large compared to the background, and an angstrom exponent near zero (Figure 6.8b). Because of the small angstrom exponent (<0.5), smoke and clouds can instantaneously be ruled

out. Small angstrom exponents are indicative of an abundance of large particle size. However, in the April 18 case, since the angstrom exponent is closer to 0.5 we can safely conclude that the plume layer was not purely dust, but mixed with other particulates along the transport pathway. Unlike smoke, dust plumes are made of very large absorbing particles, which are representative of angstrom coefficients smaller than unity. In spite of the impression from lidar that the major plume is dust-like (small angstrom exponents), elevated values of angstrom exponent at other layers (Figure 6.8) clearly indicates other particulate contributions.

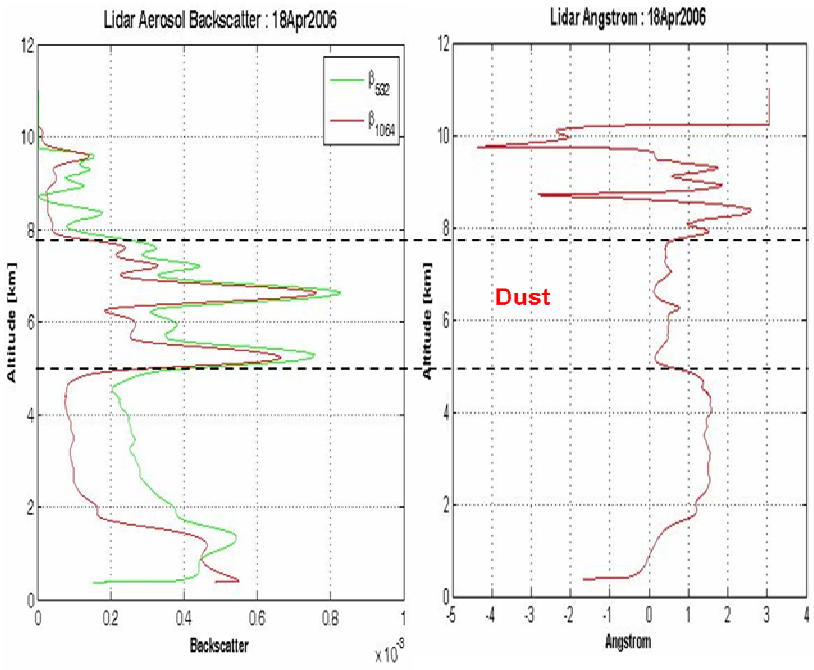

Figure 6.8: April 18, 2006 (a) Plume vertical estimate of aerosol extinction at 15:20 EST, and (b) Plume vertical estimate of angstrom exponent at 15:20 EST

In Figure 6.9(a) and (b) we show the aerosol extinction and angstrom exponent for April 19, respectively. We can see larger plume backscatter than the background, where the larger aerosol backscatter coincides with much

smaller angstrom exponents than background (~0). The small values of the angstrom coefficient (A ~ 0) confirms that the particles in the plume are consistent with dust particles. In this case it is evident that the dust particulates dominate.

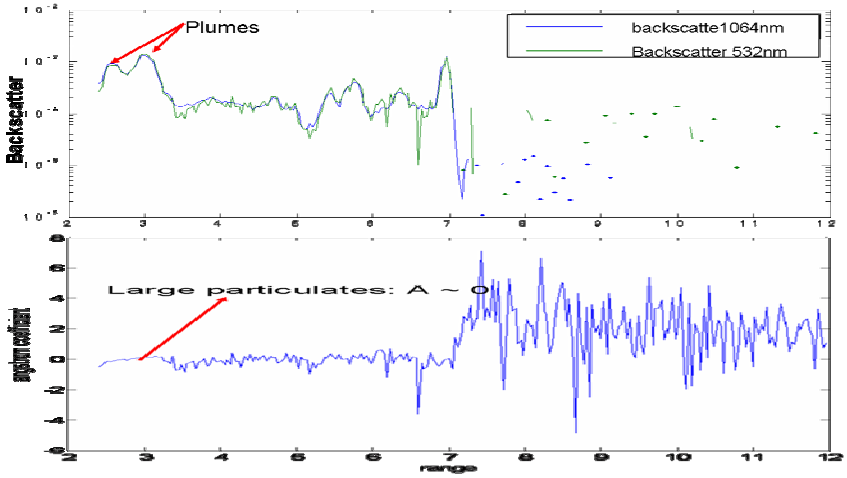

Figure 6.9: April 19, 2006 (a) Plume vertical estimate of aerosol extinction at time of plume incursion into the boundary layer 16:00 EST, and (b) Plume vertical estimate of angstrom exponent at 16:00 EST.

Finally, once we have identified the altitude of the observed plumes, further analysis based on extended backtrajectories almost always identifies the source of transport. In Figure 6.1 we show the 13-day backtrajectory ending at 2200 UTC, on April 19, 2006, at an altitude of 2000 m over the CCNY site (latitude 40.8, longitude -73.9). The ending altitude was determined from the lidar observations of the plume incursion in the boundary layer, shown in Figure 6.6. We can see that the 2 km wind trajectory (green trajectory in Figure 1b) traces back to the source regions (East Asia). A careful examination of the results reveal that the dust plume traversed the Pacific Ocean, across to south eastern Canada, and downwind to the eastern US (as shown in the OMI 8-day

UVAI composite). The wind parcel trajectory is also consistent with the wind patterns on that day in question, and there was no rainfall reported along the parcel trajectory path (not shown), which would effectively reduce the possibilities of aerosol scavenging if modeled correctly. This event was also captured by Aura's Ozone Monitoring Instrument (OMI), (Figure 6.3), with winds patterns conforming to previous findings. We can also see in Figure 6.4 high positive aerosol index along most of the trajectory path, which is indicative of absorbing aerosols (dust).

6.6.2 PLUME PROPERTIES FROM SATELLITE OBSERVATIONS

Numerous passive instruments on space-borne platforms (such as MODIS, OMI, and GOES etc.) are being used to measure the column dust aerosol optical thickness on a global scale The dust episode was captured by MODIS, GOES, and OMI. MODIS images are multi-spectral products and are captured daily and can be used for real time applications such as identifying plume transport and their properties. Because of cloud cover, assessing transport events may at times be difficult or impossible using daily multi-spectral imagery, as is the case with the dust event over northern Canada. Multi-day composite products can also provide meaningful global pictures since the data over several days can fill the gaps compared to daily averaged data. A disadvantage of this is that we loose the temporal evolution of the dust on a shorter timescale.

6.6.2.1 MODIS OBSERVATIONS

We have assumed a global transport path confined between 30^{o} and 75^{o} latitude, and performed a latitude averages AOD and weighted averaged Angstrom exponent, to observe how these plumes vary along the transport path (longitudes) for the MODIS 8-day AOD composite shown in Figure 6.2. In Figure 6.10, we display the average AOD for the above defined latitudes across all longitudes in the upper panel (blue profile), average AOD across latitudes 90^{o}N to 90^{o}S (red profile), and average over all latitudes outside the 35-75^{o} window. We can safely conclude that the highest aerosol loadings were in the source region. However, the AOD reduced in magnitude by the time it arrived the western U.S, which is consistent with the low aerosol loadings retrieved from MODIS, sun-photometer and lidar. The aerosol loading again increased along its path to the U.S east coast which may be largely due to mixing with local transport. The averaged AOD for 35-75 ^{o} N and 73.9 ^{o} W which includes CCNY, is on the same order as measured by the AERONET sun-photometer and out multi-wavelength lidar system. MODIS at times overestimates the aerosol loadings over land [Ichoku et al., 2003]. Similarly, the Angstrom exponent is smaller at the source than over the United States.

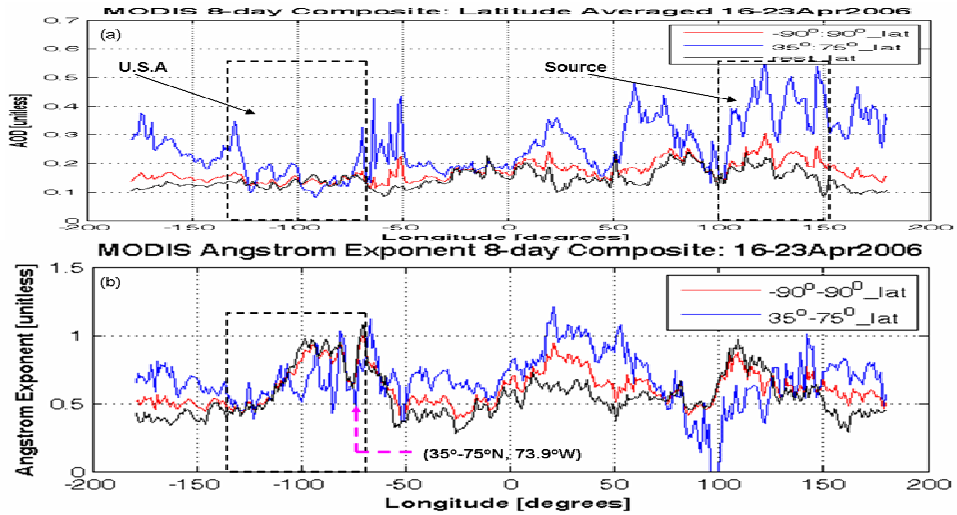

Figure 6.10: (a) MODIS AOD averaged over latitudes along all longitudes, (b) Similar for the Angstrom Exponent.

6.6.2.2 OMI OBSERVATIONS

OMI aerosol index is useful for identifying the aerosol type. In Figures 6.3 we showed the OMI UV aerosol index for the dust particulates only, where we can clearly see large plumes with high absorption index (~3) over the source region. In the 8-day composite (Figure 6.3) we can also see the larger aerosol index over the source region and the transport path. This shows that aerosol index can serve as a tracer of transport.

We also looked at the daily global variability of the UV aerosol index for April 2006, averaged over 90S-90N, 180W-180E using the GIOVANNI interface developed by the NASA Goddard Earth Science Data and Information Service Center (GES DISC). It is event that the UV absorbing aerosol index is highest during the time of the Asian dust event (Figure 6.11).

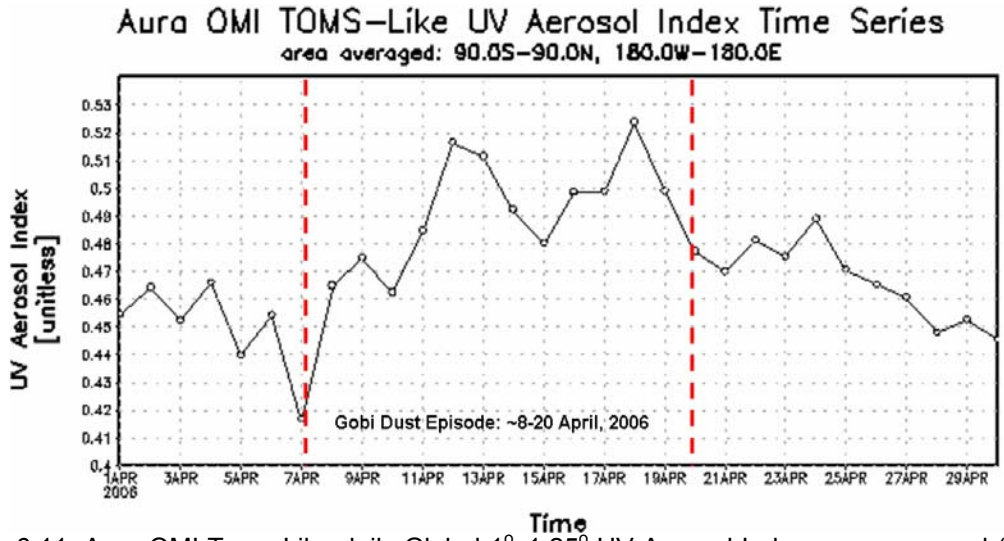

Figure 6.11: Aura OMI Toms-Like daily Global 1^{o}x1.25^{o} UV Aerosol Index area averaged (90.0S-90.0N, 180.0W-180.0E) for April, 2006. This images was acquired using the GES-DISC Interactive Online Visualization ANd aNalysis Infrastructure (Giovanni) as part of the NASA's Goddard Earth Sciences (GES) Data and Information Services Center (DISC).

6.7 LIDAR DERIVED AOD APPORTIONMENT

Lidar data can provide insight on the amount of pollution above and below the boundary layer, and can further aid in particulate matter estimates. In order to be able to estimate $PM_{2.5}$ based on optical depth, it is important to understand the connection between AOD and particulate matter. An approach to the latter is currently being used in the Infusing satellite Data into Environmental Applications (IDEA) product for the north-east, where it is assumed that 1 AOD ~ 60 μgm^{-3} of PM2.5. This allows an evaluation of the impact of elevated aerosol optical depth on near surface by using the optical depth below the boundary layer as a precursor for PM2.5 concentration estimates. This can be done by examining how well the lidar AOD apportionment below the boundary layer and the total column AOD agrees with the PM2.5 surface measurements.

Figures 6.12 (a) and (c) shows the lidar column integrated AOD (green) and AOD apportionment above the PBL (blue) for April 18 and 19. We can also see that lidar derived column optical depth is in good agreement with the sun-photometer AOD on both days. The trends seen in the aerosol loadings on April 18 and 19 are well in agreement with the features observed in the CCNY lidar images, aloft plumes with no surface interaction and plume interaction with the PBL respectively. The plume layers appear relatively stable on April 18, and remained lofted and entrained at high altitudes.

Figures 6.12 (b) and (d) show the fraction of the lidar total column AOD solely due to the plumes above the PBL. We can see that on April 18, the largest percentage of the total column AOD contribution are due to the lofted plumes above the boundary layer, with less than 20% due to PBL contributions. This is also in agreement with the lidar image, since there is no evidence of boundary layer interaction on this day. However, April 19 was quite the contrary. As the plume descended towards the surface, the PBL optical depth contribution increased from less than 5% between 3:00 and 3:30 PM to almost 40% by 5:00 PM at the time of the plume incursion. The rise in PBL AOD is expected during episodes of boundary layer plume interactions.

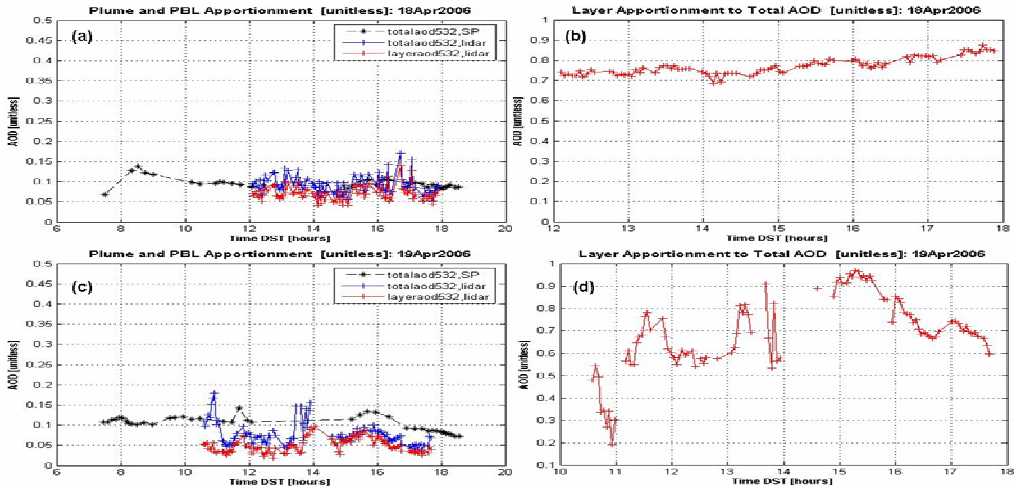

Figure 6.12: (a) Lidar column AOD (blue), Layer column AOD (red), and sun-photometer column AOD (black) April 18, 2006 (b) Lidar layer fractional AOD April 18, 2006; c) Lidar column AOD (blue), Layer column AOD (red), and sun-photometer column AOD April 19, 2006; d) Lidar layer fractional AOD April 19, 2006.

To estimate the contribution of aerosols to the boundary layer AOD, we integrated (as a function of altitude) the lidar derived aerosol extinction at 532 nm above the boundary layer and subtracted those retrievals from the sun-photometer column AOD at 500 nm. The lidar retrieved AOD's is consistent with that retrieved from the sun-photometer. In figure 6.13, the blue profile represents the sun-photometer aerosol optical depth, the green and the red profiles showing the plume column integrated and PBL AOD, respectively. In Figure 6.13, we can see that on April 19, the largest contribution of the total column aerosol loading was due to the lofted layers, but as the plumes descended and mixed with the boundary layer, the PBL contributed a comparable magnitude to the total column loadings.

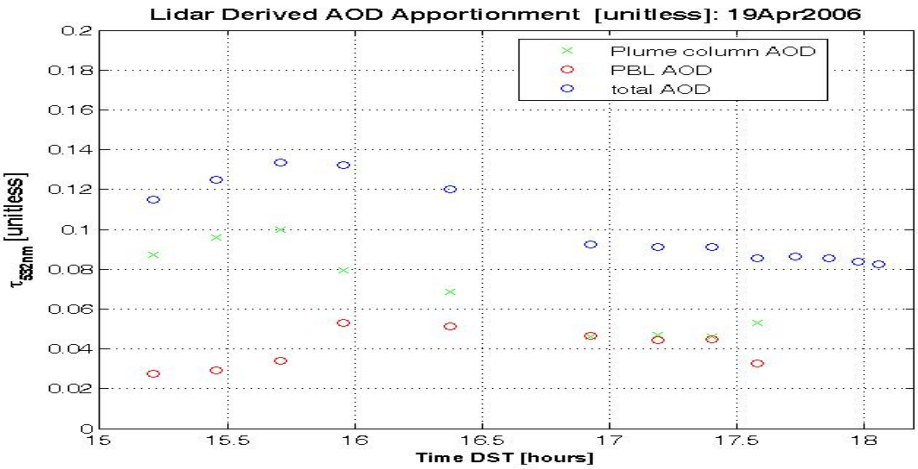

Figure 6.13: Layer column AOD (green), PBL AOD (red), and sun-photometer column AOD (blue) April 18, 2006.

We applied the IDEA PM2.5 estimator described earlier to the AOD loadings derived from the CCNY lidar below the PBL. Figure 6.14 shows the hourly $PM_{2.5}$ concentrations (measured) and the lidar PM2.5 concentrations (estimated) below the boundary layer are in reasonably good agreement with the TEOM measurements for April 19, indicating acceptable $PM_{2.5}$ estimator performance. Therefore, assuming a linear relationship between aerosol optical depth and $PM_{2.5}$ concentrations show that AOD can be used (to a reasonable approximation) as a good predictor of $PM_{2.5}$. This can be said with reservations, because there are cases where there is no obvious relationship between AOD and $PM_{2.5}$. This may have been the case for April 18 where the total column AOD was relatively higher than the PBL AOD, resulting in erroneous $PM_{2.5}$ estimations. A possible reason may be due to the majority of the aerosols being in aloft plume layers aloft.

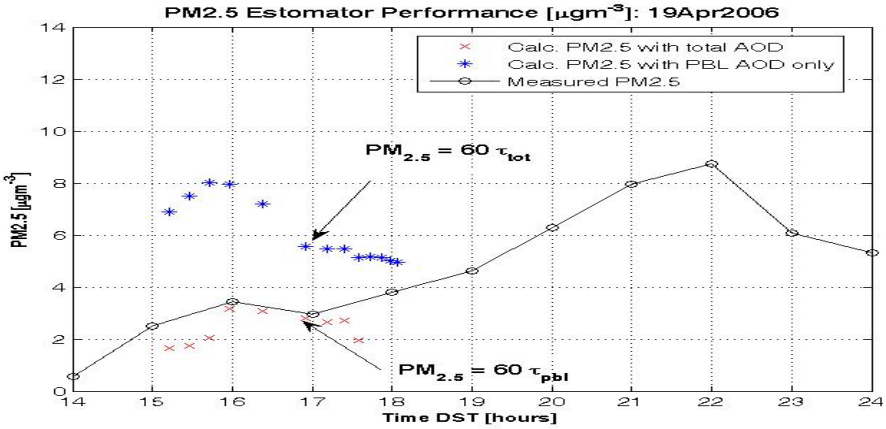

Figure 6.14: PM2.5 Estimator performance using AOD derived from sun-photometer and CCNY lidar.

6.8 SUMMARY

Vertical structure of aerosols is very important in assessing transport events and how they interact with the PBL as demonstrated. Multi-wavelength lidar can provide vertical information, and have demonstrated its usefulness in identifying large scale incursions of high altitude aerosol plumes into the Planetary Boundary Layer, and plume properties and classification through the optically derived angstrom coefficient.

Backtrajectory analysis indicated East Asian origins and estimates a travel time of 13 days, although the dust emissions at the source were intermittent. Also, combined with satellite measurements, the source of these plumes can be identified. In our case the April 2006 dust episode was traced back to the deserts in East Asia. Lidar measurements also allow us the capability to apportion the PBL optical depth characteristics from the total column, which we found to be consistent with the column integrated sun-photometer AOD. It is only when the

PBL is isolated, do the $PM_{2.5}$ measurements and predictions agree with aerosol optical depth.

Surface monitors are limited spatially, and pollution layers and plumes can be transported aloft over long distances, undetected by surface monitors, and then advect downwards to influence the surface air. Therefore, satellite observations are useful to help address these limitations by fusing surface measurements with satellite measurements, and even by augmenting surface networks.

We have also shown how well near surface aerosol loadings correlate with PM2.5, which can be used as a proxy for PM2.5 predictions. The results presented in this section show that a combination of data from lidar, satellite, and ground-based instruments looks promising and will soon be as reliably used as traditional weather forecasts.

ACKNOWLEDGMENTS

This work was partially supported under contracts from NOAA # NA17AE1625 and NASA # NCC-1-03009.

REFERENCES

Albritton, D. L., D. S. Greenbaum, "Atmospheric Observations: Helping Build the Scientific Basis for Decisions Related to Airborne Particulate Matter", EPA Report No. 1, Chapel Hill, North Carolina, 1-8, 1998.

Braak, R, O. Torres, B. Veihelmann, J. P. Veefkin, M. Kroon, and P. Levelt, "OMI UV absorbing index as a tracer for transport of Australian biomas burning aerosols", Geophys. Res. Abstracts, 9, 2007.

Chin, M., T. Diehl, P. Ginoux, and W. Malm, "Intercontinental transport of pollution and dust aerosols: implications for regional air quality", *Atmos. Chem. Phys. Discuss.*, 7, 9013-9051 (2007).

Darmenova, K, I. N. Sokolik, and A. Darmenov, "Characterization of East Asian dust outbreaks in the spring of 2001using ground-based and satellite data", J. Geophys. Res. Vol. 110, 2005.

Frenauld, F., "Analysis of atmospheric lidar observations: some comments", Appl. Op.t 23, 652-653 (1984).

Heald, C. L., D. J. Jacob, R. J. Park, B. Alexander, T. D. Fairlie, R. M. Yantosca, and D. A. Chu, "Transpacific transport of Asian anthropogenic aerosols and its impact on surface air quality in the United States", J. Geophys. Res., VOL. 111, D14310, (2006).

Herman, J. R., P. K. Bhartia, O. Torres, C. Hsu, C. Seftor, and E. Celarier, "Global distribution of UV absorbing aerosols from Nimbus 7/TOMS data". J. Geophys. Res. **102**, 16,911-16,922, 1997.

Houghton, J.T.,Y. Ding, D.J. Griggs, M. Noguer, P.J. van der Linden, X. Dai, K. Maskell, and C.A. Johnson (eds.), "Intergovernmental Panel of Climate Change (IPCC), 2001: Climate Change 2001: The Scientific Basis", Cambridge University Press, New York, NY, USA, 881pp (2001).

Husa, R. B., D. M. Tratt, B. A. Schichtel, S. R. Falke, F. Li, D. Jaffe, S. Gasso´, T. Gill, N. S. Laulainen, F. Lu, M. C. Reheis, Y. Chun, D. Westphal, B. N. Holben, C. Gueymard, I. McKendry, N. Kuring, G. C. Feldman, C. McClain, R. J. Frouin, J. Merrill, D. DuBois, F. Vignola, T. Murayama, S. Nickovic, W. E. Wilson, K. Sassen, N. Sugimoto, and W. C. Malm, "The Asian Dust Event of April 1998", J. Geophys. Res., 106, 18,317-18,330 (2001).

Ichoku, C. L., L.A. Remer, Y. J. Kaufman, R. Levy, D. A. Chu, D. Tanre, and B. N. Holben, "MODIS observation of aerosols and estimation of aerosol radiative forcing over southern Africa during SAFARI 2000", J. Geophys. Res. 108, 2003.

Jaffe, D., J. Snow, and O. Cooper, "The 2001 Asian Dust Events: Transport and Impact on Surface Aerosol Concentrations in the U.S.", EOS, Transactions, American Geophys. Union, VOL. 84, 501-516 (2003).

Kaufman, Y. J., D. Tanre, H. R. Gordon, T. Nakajima, J. Lenoble, R. Frouin, H. Grassl, B. M. Herman, M. D. King, and P.M. Teillet, "Passive remote sensing of tropospheric aerosol and atmospheric correction for the aerosol effect", J. Geophys. Res., VOL 102, 16815-16830 (1997).

Infusing satellite Fata into Environmental Applications (IDEA), http://idea.ssec.wisc.edu, Accessed April 2006, August 2007.

Kaufman, Y. J., D. Tanré, L. Remer, E. Vermote, A. Chu, and B. N. Holben, "Remote sensing of tropospheric aerosol from EOS-MODIS over the land using dark targets and dynamic aerosol models", J. Geophys. Res., 102, 17051-17067, 1997.

Loughlin, D., T. Johnson, C. Shay, and B. Hemming, "Projecting Future-Year Pollution Emissions: Emerging Approaches from the EPA ORD Global Change Air Quality Assessment", Presented at the 16th Annual International Emissions Inventory Conference, Raleigh, NC, May 2007.

NOAA ARL Real-time Environmental Applications and Display System (HYSPLIT), http://www.arl.noaa.gov/ready/hysplit4.html. Accessed April 2006, August 2007.

Prospero, J. M., P. Ginoux, O. Torres, and S. Nicholson (2002), "Environmental characterization of global sources of atmospheric soil dust derived from NIMBUS-7 TOMS absorbing aerosol product", Rev. Geophys., 40(1), 2002.

Thulasiraman, S, N. T. O'Neill, A. Roger, B. N. Holben, D. L. Westphal, and L. J. B. McArthur, "Sunphotometric observations of the 2001 Asian dust storm over Canada and the U.S.", J. Geophys. Res., VOL. 29 (2002).

Torres, O, P. K. Bhartia, J. R. Herman, Z. Ahmad, and J. Gleason, "Derivation of aerosol properties from satellite measurements of backscattered ultraviolet radiation: Theoretical basis", J. Geophys. Res. **103**, 17,099-17,110, 1998.

Torres, O, R. Decae, P. Veefkind, G. de Leeuw, "OMI Aerosol Retrieval Algorithm", OMI Algorithm Theoretical Basis Document, Volume III, Version 2, August 2002.

VanCuren, R. A., "Asian aerosols in North America: Frequency and concentration of fine dust", Geophys. Res., VOL. 107 (2002).

SUMMARY OF THESIS ACCOMPLISHMENTS

We showed how a combination of lidar and passive radiometer measurements can identify the nature of aerosol plumes, providing a more comprehensive picture of aerosol interaction and its effect on air-quality. We also showed how intercontinental transport events can have a demonstrable effect on local air quality, providing unique direct evidence that long scale aerosol transport can interact with the PBL and affect air quality parameters.

Aerosol classification from OMI is not sufficient but a synergy between OMI and MODIS provides a better classification. Geostationary Observations from GOES is very useful for studying the dynamics of plume transport but care is needed in defining “clear sky” properly. Therefore, we show that satellites are not sufficient to give a complete picture of aerosol transport, but rather a fusion of sensors including multi-wavelength lidars and ground radiometers can complete the story. The complete interpretation and classification of local aerosol transport events can only be accomplished through interplay of multiple satellite retrievals together with passive ground based multi-wavelength instruments.

We also illustrated the need to apportion the column AOD into the plume AOD and PBL AOD, and showed that it is only when this apportionment is correctly achieved, can we then use the PBL AOD as an estimator of PM2.5. We further emphasized on the fact that existing Air Quality transport models often do not predict the correct PBL height dynamics, which therefore lead to incorrect predictions of surface PM2.5 concentrations.

Finally, we showed how lidar measurements can be used together with satellite data to validate and quantify sea breeze conditions.

APPENDIX A

A.1 MULTI-SENSOR MONITORING

Satellite based aerosol remote sensing plays a critical role for monitoring of the Earth's environment and global climatology. Many of the new generation sensors, like MODIS and OMI, are designed to acquire more accurate aerosol information than classical ones. Multi-sensor monitoring of aerosols is useful to study the behavior of aerosols and particulates at multiple wavelengths. Sensors like MODerate Resolution Imaging Spectrometer (MODIS) aboard Terra and Aqua, and Ozone Mapping Instrument (OMI) aboard the EOS-AURA are found to be particularly useful in monitoring and tracking transport events.

MODIS and OMI both provide global coverage. However MODIS has a good temporal repeativity of twice daily, whereas OMI is one daily. These satellite systems have different capabilities in terms of spatial resolution, sensitivity, spectral bands, and times and frequencies of overpasses, but none of the sensing systems prior to MODIS included fire monitoring in their design. Combining multiple satellite products that provide synthetic information on different aerosol characteristics and developing multi-sensor algorithms is needed to optimize the use of the current sensing systems.

A.2 MODIS

MODIS has a fine spatial and spectral resolution with its 36 channels spanning the visible (0.415 μm) to the thermal infrared (14.235 μm) spectrum. With high clouds in the field of view, it is difficult for MODIS to provide good plume diagnostics. In general, MODIS performs the best retrieval over dark vegetative regions which are quite the contrary over urban environments. Urban areas continuously prove to be a challenge for MODIS since the ground albedo is more complex than the dark surfaces.

MODIS bands are particularly sensitive to fires; they can distinguish flaming from smoldering burns and provide better estimates of the amounts of aerosols and gases fires release into the atmosphere.

A.2.1 MODIS AEROSOL RETRIEVAL ALGORITHM OVER LAND

1. The measured reflectance at the three MODIS channels ($\rho_{0.47}$, $\rho_{0.66}$, $\rho_{2.13}$) are organized into 10-km boxes corresponding to 20 by 20 pixels at 500 m resolution for each box.
2. Each 400 pixel box is evaluated pixel by pixel to identify whether the pixels are cloudy, snow/ice, or water. The darkest pixels are identified based only on their reflectance at 2.13 μm. To be selected a pixel must fall within the range of $0.01 \leq \rho_{2.13} \leq 0.25$. The remaining pixels after masking and dark target

selection are then sorted in terms of their visible reflectance, $\rho_{0.66}$. The pixels with the darkest 20% and brightest 50% of $\rho_{0.66}$ are discarded, to eliminate any remaining pixels contaminated by cloud shadow and odd surfaces at the bright end [Remer et al., 2004]. The remaining 120 pixels will be used in the regular retrieval.

3. If there are at least 12 of these remaining from the original 20 x20 box, the inversion procedure is followed.
4. For all the identified dark pixels (12 or more dark targets), the mean measured reflectance is calculated at the three wavelengths $(\bar{\rho}_{0.47}, \bar{\rho}_{0.66}, \textit{and } \bar{\rho}_{2.13})$. The MVI is also calculated, which is a function of the surface reflectance at 2.1 and 1.2 μm.

$$MVI = (\rho_{1.2} - \rho_{2.1})/ (\rho_{1.2} + \rho_{2.1}) \qquad (A - 1)$$

5. The surface reflectance at 0.47 and 0.66 μm $(\rho^s_{0.47}, \rho^s_{0.66})$ are obtained by assuming a surface reflectance relationship

$$\rho^s_{0.66} = f(\rho^s_{2.13,} MVI, \Theta) \text{ and } \rho^s_{0.47} = f(\rho^s_{0.47,} MVI, \Theta) \qquad (A - 2)$$

6. The estimated surface reflectance and the mean TOA reflectance are used as inputs into the continental model lookup table (LUT). Spectral reflectance from the LUT is compared with the MODIS-measured spectral reflectance to find the best match. The best fit is the solution to the inversion. The aerosol optical depth at 0.47 and 0.66 μm are retrieved.
7. The estimated surface reflectance and the mean TOA reflectance.

A.3 OMI

OMI is a high-resolution spectrograph that measures the upwelling radiance at the top of the atmosphere in the ultraviolet and visible (270-500 nm) regions of the solar spectrum [Torres et al., 2007]. OMI uses TOMS-like algorithms and provides the ability to distinguish aerosols that absorb light from aerosols that reflect it. It has a 2600 km wide swath and has a spatial resolution of 13 x 24 km at nadir. The OMI measurements are used as input to inversion algorithms to retrieve ozone column amount and its vertical distribution, aerosols, clouds, and total column amounts of trace gases [Torres et al., 2007].

The main advantage of OMI for aerosol characterization from space is the availability of near-UV measurements that can be used for the retrieval of aerosol properties using the TOMS-like inversion techniques. These techniques work well over all surface types (including urban, unlike MODIS) because the reflectance of all terrestrial surfaces is small in the UV, including arid regions that appear very bright in the visible and near-IR. A second advantage of the technique is the strong interaction between aerosol absorption and molecular scattering from below the aerosol layers, which allows an estimate of the amount of absorption (AAOD) due to aerosols. The availability of the multi-wavelength (UV and VIS.) measurements allows a better characterization of the aerosol load.

A.3.1 OMI AEROSOL NEARUV RETRIEVAL ALGORITHM

The OMAERUV data product consist of the UV aerosol index (UVAI), aerosol extinction optical depth (AOD) and aerosol absorption optical depth (AAOD) ta 354, 388 and 500 nm. The AOD is a measure of the extinction of light by aerosols due to the combined effect of scattering and absorption. AAOD on the other hand, is due to absorption only. The UVAI is a measure of the departure of the spectral dependence of the near UV upwelling radiation at the top of the atmosphere [Stammes et al., 2002].

The OMAERUV aerosol algorithm uses measurements made at two wavelengths in the UV, 354 and 388 nm, in order to make use of the large sensitivity of the upwelling radiance to aerosol absorption in that spectral region [Torres et al., 2007, Torres et al., 1998], and partly because of the lack of reliable surface reflectance data at the longer OMI wavelengths. Note that wavelengths below 340 nm cannot be used due to strong ozone absorption. There are two advantages of the near-UV technique for deriving aerosols. Firstly, in the UV, the reflectance of all terrestrial surfaces is very low (due to high Rayleigh scattering properties of the UV), therefore the retrieval of aerosol properties over both land and water surfaces, including the arid and semi-arid regions that appear very bright (highly refective) in the visible and near-IR. Secondly, interaction between aerosol absorption and molecular scattering from below the aerosol layer allows an estimation of AAOD.

Below are the steps in the OMAERUV algorithm:

1. Calculation the Lambert Equivalent Reflectivity (R_{obs})

$$R_{obs} = \frac{I_{388}^{obs} - I_{388}^{Ray}}{T_{388}^{Ray} + S_{b388}^{Ray}(I_{388}^{obs} - I_{388}^{Ray})} \quad \text{(A-3)}$$

where, I_{388}^{obs} is the OMI observed radiance at 388 nm, I_{388}^{Ray} is the calculated atmospheric radiance, T_{388}^{Ray} is the transmittance, and S_{b388}^{Ray} is the spherical albedo for a Rayleigh atmosphere.

2. Calculation of the UV Aerosol Index (UVAI)

$$UVAI = -100 \log_{10}[\frac{I_{354}^{obs}}{I_{354}^{cal}(R_{obs})}] \quad \text{(A-4)}$$

I_{354}^{calc}, the calculated radiance at 354 nm assumes a Lambert Equivalent Reflectivity (R_{obs}), equation A-1. Since UVAI is sensitive to UV-absorbing aerosols only, it is used to discriminate between carbonaceous (biomass burning) and dust aerosols, since they absorb in the UV. This allows a differentiation between absorbing and weakly/non-absorbing such as sulfates, nitrates, etc.

To clearly differentiate between carbonaceous and desert dust aerosols the algorithm takes advantage of the scene darkening effect of desert dust aerosols in the near UV:

(a) In the algorithm, three types of aerosols are assumed, desert dust (DST), carbonaceous aerosols associated with biomass burning (BIO), and weakly-absorbing sulfates (SLF).

(b) At 388 nm, the scattering and absorption effects of desert dust aerosols nearly cancel, therefore, the LER is close to the true surface reflectivity. Carbonaceous aerosols, on the other hand generally increases the LER compared to the true surface reflectivity. The change in the net aerosol reflectivity (ΔR) at 388 nm is

$$\Delta R = R_{obs} - R_{sfc} \qquad \text{(A-5)}$$

(c) The ΔR and UVAI, in conjunction with the aerosol type (obtained from AERONET micro-physical properties) are used to select an aerosol type.

3. Since the retrieval of desert dust and carbonaceous aerosols are sensitive to the aerosol layer height [Torres et al., 2007], the results are reported at five different assumptions of the aerosol center of mass (surface, 1.5, 3.0, 6.0, and 10.0 km). The best estimates of AOD and AAOD are associated with a particular choice of aerosol layer height, which varies with aerosol type and geographical location.
4. Results are also reported at 354 and 500 nm.

REFERENCES

Remer, L. A., Y. J. Kaufman, D. Tanre, S. Mattoo, D. A. Chu, J. V. Martins, R. R. Li, C. Ichoku, R. C. Levy, R. G. Kleidman, T. F. Eck, E. Vermote, and B. N. Holben, "The MODIS Aerosol Algorithm, Products, and Validation", American Meteorological Society, 2004.

Stammes, P., R. Noordhoek, "OMI Algorithm Theoretical Basis Document: OMI Aerosol Retrieval Algorithm", VOL 3, Vers. 2.0, August 2002.

Torres, Omar, Aapo Tanskanen, Ben Veihelmann, Changwoo Ahn, Remco Braak, Pawan K. Bhartia, Pepijn Veefkind, and Pieternel Levelt, "Aerosols and surface UV products from Ozone Monitoring Instrument observations: An overview", J. Geophys. Res., 112, 2007.

Torres, O., P. K. Bhartia, J. R. Herman, Z. Ahmad, "Derivation of aerosol properties from satellite measurements of backscattered ultraviolet radiation: Theoretical basis", J. Geophys. Res., 103, 1998.

BIBLIOGRAPHY

CHAPTER 1

Brinksma, E. J., K. F. Bousma, and P. F. Levelt, "Validation Requirements Document", 2003.

Chu, D. A., Y. J. Kaufman, G. Zibordi, J. D. Chern, J. Mao, C. Li and B. N. Holben, "Global Monitoring of air pollution over Land from the Earth Observing System – Terra Moderate Resolution Imaging Spectrometer (MODIS)", Journal of Geophysical Research, VOL. 108, D21, 2003.

Diner, D. I., Russe A. Chipman, Neil Beaudryb, Brian Caims, Leslie D. Food, Steven A. Macenka, Thomas J. Cunningham, Suresh Seshadli, and Christoph Keller, "An integrated multiangle, multispectral, and polarimetric imaging concept foor aerosol remeote sensing from space", 2004.

Diner, D.J., T.P. Ackerman, T.L. Anderson, J. Bosenberg, A.J. Braverman, R.J. Charlson, W.D. Collins, R. Davies, B.N. Holben, C.A. Hostetler, R.A. Kahn, J.V. Martonchik, R.T. Menzies, M.A. Miller, J.A. Ogren, J.E. Penner, P.J. Rasch, S.E. Schwartz, J.H. Seinfeld, G.L. Stephens, O. Torres, L.D. Travis, B.A. Wielicki, and B. Yu, "PARAGON: An integrated approach for characterizing aerosol climate impacts and environmental interactions", Bull. Amer. Meteorol. Soc., **85**, 14911-1501, 2004.

Engel-Cox, J. A., H. H. Christopher, B. W. Coutant and R. M. Hoff, "Qualitative and Quantitative evaluation of MODIS satellite sensor data for regional and urban scale air quality", Atmospheric Environment, VOL. 38, pp. 2495-2509, 2004.

Heintzenberg, Jost and David S. Covert, "On the distribution of physical and chemical particle properties in the atmospheric aerosol", Journal of Atmospheric Chemistry, VOL. 10, 4, 1990.

Schneider, J. and R. Eixmann, "Three years of routine Raman lidar measurements of tropospheric aerosols: Backscattering, extinction, and residual layer height" Atmos. Chem. Phys., 2, 313–323, 2002.

Wang J. and S. A. Christopher, "Inter-comparison between Satellite-derived Aerosol Optical Thickness and PM2.5 mass: Implications of Air Quality Studies", Geophysical Research Letters, VOL. 30, 2003.

Yu, H., Y. J. Kaufman, M. Chin, G. Feingold, L. A. Remer, T. L. Anderson, Y. Balkanski5, N. Bellouin, O. Boucher, S. Christopher, P. DeCola, R. Kahn, D. Koch, N. Loeb, M. S. Reddy, M. Schulz, T. Takemura, and M. Zhou, "A review of measurement-based assessment of aerosol direct radiative effect and forcing", Atmos. Chem. Phys. Discuss., 5, 7647-7768, 2005.

CHAPTER 2

Albrecht, B. A., "Aerosols, cloud microphysics and fractional cloudiness. Science", 245, 1227–1230, 1989.

Bret Brunekreef, "Health Effects of Ambient Particulate Matter", 7th International Aerosol Conference, Minnesota, 2006.

Chu, D. A., Y. J. Kaufman, G. Zibordi, J. D. Chern, J. Mao, C. Li and B. N. Holben, "Global Monitoring of air pollution over Land from the Earth Observing System – Terra Moderate Resolution Imaging Spectrometer (MODIS)", Journal of Geophysical Research, VOL. 108, D21, 2003.

Dockery, D. W. and C. A. Pope III, "Acute Respiratory Effects of Particulate Air Pollution", NYU, Annual Review of Public Health, 15, 1994.

Forster, P., V. Ramaswamy, P. Artaxo, T. Berntsen, R. Betts, D.W. Fahey, J. Haywood, J. Lean, D.C. Lowe, G. Myhre, J. Nganga, R. Prinn, G. Raga, M. Schulz and R. Van Dorland, 2007: "Changes in Atmospheric Constituents and in Radiative Forcing. In: Climate Change 2007: The Physical Science Basis. Contribution of Working Group I to the Fourth Assessment Report of the Intergovernmental Panel on Climate Change" [Solomon, S., D. Qin, M. Manning, Z. Chen, M. Marquis, K.B. Averyt, M.Tignor and H.L. Miller (eds.)]. Cambridge University Press, Cambridge, United Kingdom and New York, NY, USA.

Hansen, James E. and Makiko Sato, "Trends of measured climate forcing agents", Proceedings of the National Academy of Sciences (PNAS), 98, 26, 2001.

Heintzenberg J., "Arctic haze: Air pollution in polar region", AMBIO 18(1): 50-55, 1998.

NOAA's ARC, "NEAQS-ITCT 2004 Science & Implementation Plan", 2003.

Pincus, R. and M. B. Baker, "Effect of precipitation on the albedo susceptibility of marine boundary layer clouds", Nature, 372, 250–252, 1994.

Poschl, U., T. Fehrenbach, T. Franze, U. McKeon, A. Messerer, E. Mikhailov, R. Niessner, C. Schauer, and A. Zerrath, "Carbonaceous Aerosol Components: Properties, Interactions, Climate and Health Effects", Geo. Res. Letters, 8, 2006.

Schwartz, Joel and Douglas W. Dockery, "Particulate Air Pollution and Daily Mortality in Steubenville, Ohio", Amer. Jour. Epidemiology, VOL. 135, 1994.

Szykman, J., et al "Utilizing MODIS satellite observations in near-real-time to improve AIRNow next day forecast of fine particulate matter, PM2.5" Proceedings of the Sixth Conference on Atmospheric Chemistry, American Meteorological Society, January 10-15, 6pp. (2004).

Twomey, S., "The influence of pollution on the short wave albedo of clouds", J. Atmos. Sci., 34, 1149–1152, 1977.

CHAPTER 3

Bisson, S. E, J. E. M. Goldsmith, and M. G. Mitchell, "Daytime Raman lidar profiling of atmospheric water vapor", Appl.Opt. **38**, 1,841–1,849 (1999).

Chen H. et al., Opt. Lett. **21**, 1,093–1,095 (1997).

Fernauld, F. G., "Analysis of Atmospheric Lidar Observations", Applied Optics, VOL. 23, pp. 652, 1984.

Gobbi, G. P., F. Barnaba, R. Van Dingenen, J. P. Putaud, M. Mircea, and M. C. Facchini, "Lidar and in situ observations of continental and Saharan aerosol: closure analysis of particles optical and physical properties", Atmos. Chem. Phys., 3, 2161-2172, 2003.

Kovalev, Vladimir A., and William E. Eichinger, "Elastic Lidar: Theory, Practice, and Analysis Methods", 2004

Weitkamp, C., "LIDAR: Range-Resolved Optical Remote Sensing of the Atmosphere," Springer Series in Optical Science, VOL. 1, 2005.

CHAPTER 4

Charles, L., S. et. al., "Application of CCNY Lidar and ceilometers to the study of Aerosol Transport and PM2.5 monitoring". Amer. Meteor. Soc., 3rd Symposium on Lidar Atmospheric Applications, 2007.

Charlson RJ, Schwartz SE, Hales JM, Cess RD, Coakley Jr JA, Hansen JE, Hoffman DJ. 1992. "Climate forcing by anthropogenic aerosols", Science **255**: 423–430.

Gedzelman, S. D., et. al., "Mesoscale weather features in NYC revealed by CCNY Lidar". Amer. Meteor. Soc., 6th Symposium on the Urban Environment, 2006.

Hashvardhan et al., "Aerosol–climate interactions. In Aerosol-Cloud-Climate Interactions", Hobbs PV (ed.). International Geophysics Series vol. 54. 75–95, 1993.

Houghton JT, Meira Filho LG, Callander BA, Harris N, Kattenberg A, Maskell K (eds), "The Science Climate Change", IPCC (Inter-Governmental Panel for Climate Change), Cambridge University Press; 572 pp., 1995.

Kiehl JT, Briegleb BP., "The relative roles of sulfate aerosols and greenhouse gases in climate forcing", Science **260**: 311–314, 1993.

Nelson, Noel, "The Impact of Weather on Pollution", Indoor Built Environment, VOL 9, 1-4, 2000.

Penner JE, Charlson RJ, Hales JM, Laulainen NS, Leifer R, Novakov T, Ogren J, Radke LF, Schwartz SE, Travis L., "Quantifying and minimizing uncertainty of climate forcing by anthropogenic aerosols", Bulletein of the American Meteorological Society **75**:375–400, 1994.

Richard D. Clark**, "**Modification of surface and boundary layer meteorology and chemistry by seabreeze incursions during NE-OPS", 2002.

Taylor K, Penner JE., "Response of the climate system to atmospheric aerosols and greenhouse gases", Nature **369**: 734–737, 1994.

Wallace, John M. and Peter V. Hobbs, "Atmospheric Science: AN Introductory Survey", International Geophysics Series, VOL. 29, 2nd Ed., 2006.

CHAPTER 5

Angstrom, A., "On the atmospheric transmission of sun radiation and on dust in the air", Geogr. Ann., 11, 156–166, 1929.

ARL HQ Modeling Group, "HYSPLIT Interim Smoke Forecast Tool".

Braak, R., O. Torres, B. Veihelmann, J. P. Veefkin, M. Kroon, and P. Levelt, "OMI UV absorbing index as a tracer for transport of Australian biomas burning aerosols", Geophys. Res. Abstracts, 9, 2007.

Herman., J. R, P. K. Bhartia, O. Torres, C. Hsu, C. Seftor, and E. Celarier, "Global distribution of UV absorbing aerosols from Nimbus 7/TOMS data", J. Geophys. Res. **102**, 16,911-16,922, 1997.

Kaufman, Y. J., "Aerosol optical thickness and atmospheric path radiance", J. Geophys. Res., 98(D2), 2677–2692, 1993.

Kaufman, Y. J., D. Tanré, L. Remer, E. Vermote, A. Chu, and B. N. Holben, "Remote sensing of tropospheric aerosol from EOS-MODIS over the land using dark targets and dynamic aerosol models", J. Geophys. Res., VOL. 102, 17051-17067, 1997.

Knapp, Kenneth R., "Quantification of aerosol signal in GOES 8 visible imagery over the United States", J. Geophys. Res., VOL. 107, NO. D20, 2002.

Knapp, Kenneth R. and Thomas H. Vonder Haar, "Aerosol Optical Depth Retrieval from GOES-8: Uncertainty study and Retrieval validation over South America", J. Geophys. Res., VOL. 107, NO. D7, 2002.

Knapp, Kenneth R., R. Frouin, S. Kondragunta, and A. Prados, "Towards Aerosol Optical Depth Retrievals over land from GOES visible radiances: determine surface reflectance", International Journal of Remote Sensing, VOL. 26, NO. 18, 2005.

Kondragunta, S., P. Ciren, A. I. Prados, Y. Shinozuka, A. Clark, "Characterization of GOES-12 Aerosol Optical Depth Retrievals during ICARTT/INTEX-A", J. Geophys. Res.

Prados, Ana I., Shobha Kondragunta, Puba Ciren, and Kenneth R. Knapp, "GOES Aerosol/Smoke Product (GASP) over North America: Comparisons to AERONET and MODIS observations", J. Geophys. Res. 112, 2007.

Torres, O, P. K. Bhartia, J. R. Herman, Z. Ahmad, and J. Gleason, "Derivation of aerosol properties from satellite measurements of backscattered ultraviolet radiation: Theoretical basis". J. Geophys. Res. **103**, 17,099-17,110, 1998.

Torres, O., R. Decae, P. Veefkind, G. de Leeuw, "OMI Aerosol Retrieval Algorithm", OMI Algorithm Theoretical Basis Document, Volume III, Version 2, August 2002.

CHAPTER 6

Albritton, D. L., D. S. Greenbaum, "Atmospheric Observations: Helping Build the Scientific Basis for Decisions Related to Airborne Particulate Matter", EPA Report No. 1, Chapel Hill, North Carolina, 1-8, 1998.

Braak, R, O. Torres, B. Veihelmann, J. P. Veefkin, M. Kroon, and P. Levelt, "OMI UV absorbing index as a tracer for transport of Australian biomas burning aerosols", Geophys. Res. Abstracts, 9, 2007.

Chin, M., T. Diehl, P. Ginoux, and W. Malm, "Intercontinental transport of pollution and dust aerosols: implications for regional air quality", *Atmos. Chem. Phys. Discuss.*, 7, 9013-9051 (2007).

Darmenova, K, I. N. Sokolik, and A. Darmenov, "Characterization of East Asian dust outbreaks in the spring of 2001using ground-based and satellite data", J. Geophys. Res. Vol. 110, 2005.

Frenauld, F., "Analysis of atmospheric lidar observations: some comments", Appl. Op.t 23, 652-653 (1984).

Heald, C. L., D. J. Jacob, R. J. Park, B. Alexander, T. D. Fairlie, R. M. Yantosca, and D. A. Chu, "Transpacific transport of Asian anthropogenic aerosols and its impact on surface air quality in the United States", J. Geophys. Res., VOL. 111, D14310, (2006).

Herman, J. R., P. K. Bhartia, O. Torres, C. Hsu, C. Seftor, and E. Celarier, "Global distribution of UV absorbing aerosols from Nimbus 7/TOMS data". J. Geophys. Res. **102**, 16,911-16,922, 1997.

Houghton, J.T.,Y. Ding, D.J. Griggs, M. Noguer, P.J. van der Linden, X. Dai, K. Maskell, and C.A. Johnson (eds.), "Intergovernmental Panel of Climate Change (IPCC), 2001: Climate Change 2001: The Scientific Basis", Cambridge University Press, New York, NY, USA, 881pp (2001).

Husa, R. B., D. M. Tratt, B. A. Schichtel, S. R. Falke, F. Li, D. Jaffe, S. Gasso´, T. Gill, N. S. Laulainen, F. Lu, M. C. Reheis, Y. Chun, D. Westphal, B. N. Holben, C. Gueymard, I. McKendry, N. Kuring, G. C. Feldman, C. McClain, R. J. Frouin, J. Merrill, D. DuBois, F. Vignola, T. Murayama, S. Nickovic, W. E. Wilson, K. Sassen, N. Sugimoto, and W. C. Malm, "The Asian Dust Event of April 1998", J. Geophys. Res., 106, 18,317-18,330 (2001).

Ichoku, C. L., L.A. Remer, Y. J. Kaufman, R. Levy, D. A. Chu, D. Tanre, and B. N. Holben, "MODIS observation of aerosols and estimation of aerosol radiative forcing over southern Africa during SAFARI 2000", J. Geophys. Res. 108, 2003.

Jaffe, D., J. Snow, and O. Cooper, "The 2001 Asian Dust Events: Transport and Impact on Surface Aerosol Concentrations in the U.S.", EOS, Transactions, American Geophys. Union, VOL. 84, 501-516 (2003).

Kaufman, Y. J., D. Tanre, H. R. Gordon, T. Nakajima, J. Lenoble, R. Frouin, H. Grassl, B. M. Herman, M. D. King, and P.M. Teillet, "Passive remote sensing of tropospheric aerosol and atmospheric correction for the aerosol effect", J. Geophys. Res., VOL 102, 16815-16830 (1997).

Infusing satellite Fata into Environmental Applications (IDEA), http://idea.ssec.wisc.edu, Accessed April 2006, August 2007.

Kaufman, Y. J., D. Tanré, L. Remer, E. Vermote, A. Chu, and B. N. Holben, "Remote sensing of tropospheric aerosol from EOS-MODIS over the land using dark targets and dynamic aerosol models", J. Geophys. Res., 102, 17051-17067, 1997.

Loughlin, D., T. Johnson, C. Shay, and B. Hemming, "Projecting Future-Year Pollution Emissions: Emerging Approaches from the EPA ORD Global Change Air Quality Assessment", Presented at the 16th Annual International Emissions Inventory Conference, Raleigh, NC, May 2007.

NOAA ARL Real-time Environmental Applications and Display System (HYSPLIT), http://www.arl.noaa.gov/ready/hysplit4.html. Accessed April 2006, August 2007.

Prospero, J. M., P. Ginoux, O. Torres, and S. Nicholson (2002), "Environmental characterization of global sources of atmospheric soil dust derived from NIMBUS-7 TOMS absorbing aerosol product", Rev. Geophys., 40(1), 2002.

Thulasiraman, S, N. T. O'Neill, A. Roger, B. N. Holben, D. L. Westphal, and L. J. B. McArthur, "Sunphotometric observations of the 2001 Asian dust storm over Canada and the U.S.", J. Geophys. Res., VOL. 29 (2002).

Torres, O, P. K. Bhartia, J. R. Herman, Z. Ahmad, and J. Gleason, "Derivation of aerosol properties from satellite measurements of backscattered ultraviolet radiation: Theoretical basis", J. Geophys. Res. **103**, 17,099-17,110, 1998.

Torres, O, R. Decae, P. Veefkind, G. de Leeuw, "OMI Aerosol Retrieval Algorithm", OMI Algorithm Theoretical Basis Document, Volume III, Version 2, August 2002.

VanCuren, R. A., "Asian aerosols in North America: Frequency and concentration of fine dust", Geophys. Res., VOL. 107 (2002).

APPENDIX

Remer, L. A., Y. J. Kaufman, D. Tanre, S. Mattoo, D. A. Chu, J. V. Martins, R. R. Li, C. Ichoku, R. C. Levy, R. G. Kleidman, T. F. Eck, E. Vermote, and B. N. Holben, "The MODIS Aerosol Algorithm, Products, and Validation", American Meteorological Society, 2004.

Stammes, P., R. Noordhoek, "OMI Algorithm Theoretical Basis Document: OMI Aerosol Retrieval Algorithm", VOL 3, Vers. 2.0, August 2002.

Torres, Omar, Aapo Tanskanen, Ben Veihelmann, Changwoo Ahn, Remco Braak, Pawan K. Bhartia, Pepijn Veefkind, and Pieternel Levelt, "Aerosols and surface UV products from Ozone Monitoring Instrument observations: An overview", J. Geophys. Res., 112, 2007.

Torres, O., P. K. Bhartia, J. R. Herman, Z. Ahmad, "Derivation of aerosol properties from satellite measurements of backscattered ultraviolet radiation: Theoretical basis", J. Geophys. Res., 103, 1998.

CONFERENCES / PUBLICATIONS

Charles et al., "**Atmospheric transport of smoke and dust particulates and their interaction with the Planetary Boundary Layer as observed by multi-wavelength lidar and supporting instrumentation**", *Proc. SPIE Int. Soc. Opt. Eng.,Vol. 6681, Sept. 26, 2007,* doi:10.1117/12.731943.

Charles et al, "**Application of CCNY Lidar and Ceilometers to the study of Aerosol Transport and PM2.5 Monitoring**", *AMS 3rd Symposium on Lidar Atmospheric Applications, Jan. 2007.*

Jia-Yeong Ku, Chris Hogrefe, Gopal Sistla, Chaw, S., L. Charles, B. Gross, "***Use of Lidar backscatter to determine the PBL heights in NYC*"**, NYC 2006.

Chaw, S., L. Charles, "**Application of Remote Sensing Tools for the Assessment of Regional Air Quality Forecast Models and Indoor Air Quality**", CUNY Sustainability Conference, Energy and Environmental Stability: Science, Engineering and Public Policy, Dec. 2006, CUNY Graduate Center, NYC.

Charles et al., "**Improving CALIPSO Llidar Retrievals of Surface Level Backscatter**", 3rd Annual GOES-R Users Conference, Colorado May 2004.

Leona Charles, M. M. Oo, B. Herman B. Gross, F. Moshary and S. Ahmed, "**Improving Calipso Lidar Retrievals of Surface Level Backscatter as a Proxy for PM2.5 using MODIS Path Reflectance Constraints***", ILRC.*

Eduardo H. Hernandez, Min Min Oo, Leona Charles, Barry Gross, Margarita Mihailidi, Fred Moshary, "**Assessing the Land Albedo Model of the New Modis Aerosol over Land Algorithm for Urban Scenes",** *AMS 87th Annual Conference – 3rd Lidar, January 14-18, 2007.*

Stanley David Gedzelman, Kwan-yin Kong, Fred Moshary, Heather Yael Glickman, Barry Gross, and Leona Charles, *"***Fair Weather Climatology Revealed By CNNY Lidar***", AMS 87th Annual Conference – 3rd Lidar, January 14-18, 2007.*

Charles et al, '**ANALYSIS OF THE INTERACTION OF AEROSOL TRANSPORT LAYERS ON LOCAL AIR QUALITY',** *IGARSS 2008*